



**This electronic thesis or dissertation has been
downloaded from Explore Bristol Research,
<http://research-information.bristol.ac.uk>**

Author:
Warburton, Julia M

Title:
**Investigating the effect of amyloid-beta on hippocampal dynamics in Alzheimer's
disease**

General rights

Access to the thesis is subject to the Creative Commons Attribution - NonCommercial-No Derivatives 4.0 International Public License. A copy of this may be found at <https://creativecommons.org/licenses/by-nc-nd/4.0/legalcode> This license sets out your rights and the restrictions that apply to your access to the thesis so it is important you read this before proceeding.

Take down policy

Some pages of this thesis may have been removed for copyright restrictions prior to having it been deposited in Explore Bristol Research. However, if you have discovered material within the thesis that you consider to be unlawful e.g. breaches of copyright (either yours or that of a third party) or any other law, including but not limited to those relating to patent, trademark, confidentiality, data protection, obscenity, defamation, libel, then please contact collections-metadata@bristol.ac.uk and include the following information in your message:

- Your contact details
- Bibliographic details for the item, including a URL
- An outline nature of the complaint

Your claim will be investigated and, where appropriate, the item in question will be removed from public view as soon as possible.



**This electronic thesis or dissertation has been
downloaded from Explore Bristol Research,
<http://research-information.bristol.ac.uk>**

Author:
Warburton, Julia M

Title:
Investigating the effect of amyloid-beta on hippocampal dynamics in Alzheimer's disease

General rights

Access to the thesis is subject to the Creative Commons Attribution - NonCommercial-No Derivatives 4.0 International Public License. A copy of this may be found at <https://creativecommons.org/licenses/by-nc-nd/4.0/legalcode> This license sets out your rights and the restrictions that apply to your access to the thesis so it is important you read this before proceeding.

Take down policy

Some pages of this thesis may have been removed for copyright restrictions prior to having it been deposited in Explore Bristol Research. However, if you have discovered material within the thesis that you consider to be unlawful e.g. breaches of copyright (either yours or that of a third party) or any other law, including but not limited to those relating to patent, trademark, confidentiality, data protection, obscenity, defamation, libel, then please contact collections-metadata@bristol.ac.uk and include the following information in your message:

- Your contact details
- Bibliographic details for the item, including a URL
- An outline nature of the complaint

Your claim will be investigated and, where appropriate, the item in question will be removed from public view as soon as possible.

Investigating the effect of amyloid-beta on hippocampal dynamics in Alzheimer's disease

By

JULIA WARBURTON



Bristol Centre for Complexity Sciences
Department of Engineering Mathematics
UNIVERSITY OF BRISTOL

A dissertation submitted to the University of Bristol in accordance with the requirements of the degree of Doctor of Philosophy in the Faculty of Engineering.

NOVEMBER 2019

Word count: 33,545

ABSTRACT

Alzheimer's disease (AD) is a complex and multifactorial, neurodegenerative disease. Accumulation of pathogenic forms of the protein amyloid-beta ($A\beta$), one of the hallmark features of AD, is thought to have a causal role in this neurodegeneration. Enhanced levels of $A\beta$ are associated with synaptic dysfunction, altered neuronal intrinsic excitability and altered gamma frequency activity within the hippocampus.

In this thesis, biophysical models of synapses, neurons and networks are combined with experimental work to examine how $A\beta$ alters neural activity in the CA1 hippocampal region. The acute effect of $A\beta$ -infusion on synaptic transmission is investigated by recording spontaneous miniature excitatory postsynaptic currents (mEPSCs) from CA1 neurons in cultured hippocampal slices; $A\beta$ is found to cause a rapid increase in mEPSC amplitude. Using a first-order kinetic synapse model parameterised using the mEPSC data it is found that the increase in amplitude can be accounted for by a 50% increase in the synaptic conductance of the model.

Two versions of a single-compartment biophysical model are used to simulate intrinsic excitability measures recorded from CA1 pyramidal neurons in wild type and PDAPP transgenic mice that overexpress $A\beta$. Both models predict that altered excitability in PDAPP neurons can be accounted for by lowering the transient Na^+ and delayed-rectifier K^+ (K_{DR}) channel conductances and by slowing the activation rate of the K_{DR} -channel.

The potential impacts of these observations on gamma frequency oscillations are explored using an excitatory-inhibitory network model. The $A\beta$ -mediated increase in synaptic transmission increases the total gamma power of the oscillations, progressively increasing as more synapses are affected. Incorporating the PDAPP neuron model into the network increases the frequency of the gamma oscillations.

These results illustrate how data-informed mathematical models can bring new insights into the underlying mechanisms and implications of $A\beta$ pathology and can contribute to a quantitative and multiscale understanding of AD.

DEDICATION AND ACKNOWLEDGEMENTS

This PhD has been a bit of a bumpy ride and I would not have got to this point without the help of the people I've been lucky to have around me. Many thanks go to my supervisors, Kراسي and Lucia for their support, encouragement and guidance. Thanks to the other people I've worked with along the way including Daniel, Jeena, Kyle and particularly Conor for going out of his way to help me. Thanks to my friends at the BCCS, particularly Bert, Louis, Alonso and Lily for the days in the office. Thanks to Alice and Laura for being there, to Annie for her advice, and last but not least, my thanks go to Rich for his unending support and patience and to my parents for helping me get to the end.

AUTHOR'S DECLARATION

I declare that the work in this dissertation was carried out in accordance with the requirements of the University's Regulations and Code of Practice for Research Degree Programmes and that it has not been submitted for any other academic award. Except where indicated by specific reference in the text, the work is the candidate's own work. Work done in collaboration with, or with the assistance of, others, is indicated as such. Any views expressed in the dissertation are those of the author.

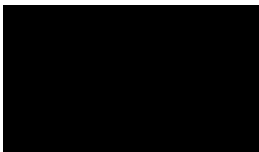
SIGNED:  DATE: 29/11/2019

TABLE OF CONTENTS

	Page
List of Tables	xi
List of Figures	xiii
1 Introduction	1
1.1 Thesis Overview	3
1.2 Thesis Contributions	5
2 Background	7
2.1 Alzheimer's Disease: An Overview	7
2.1.1 The Amyloid-beta hypothesis	10
2.2 The Hippocampus	12
2.2.1 Hippocampal Structure	12
2.2.2 Oscillations in the Hippocampus	13
2.2.3 AD and the Hippocampus	15
2.3 Computational Models of AD	16
2.3.1 Modelling Neuronal-level Dysfunction	16
3 Computational Models	21
3.1 Model Backgrounds	22
3.1.1 Ion Channel Gating Mechanisms	22
3.1.2 Conductance-based Neuronal Models	25
3.2 Synapse Model	26
3.3 Single Cell Models	27
3.3.1 Pyramidal neuron model	27
3.3.2 Fast-spiking interneuron model	29
3.4 Network model	30

4	The acute effect of intracellular Aβ on spontaneous synaptic transmission	33
4.1	Background	33
4.1.1	A β and Synaptic Dysfunction	33
4.1.2	Acute Synaptic Effect of Intracellular oA β	34
4.1.3	AMPA Receptors	34
4.1.4	Spontaneous Transmission and Miniature EPSCs	35
4.2	Experimental Methods	38
4.2.1	Hippocampal Slice Preparation	38
4.2.2	Amyloid- β_{1-42} Preparation	39
4.2.3	Electrophysiology Equipment	40
4.2.4	Whole-cell Patch Protocol	41
4.2.5	Miniature EPSC Recording Protocol	42
4.2.6	Data Acquisition and Analysis	43
4.3	Results	45
4.3.1	mEPSC Amplitude & Frequency Analysis	45
4.3.2	mEPSC Kinetics Analysis	47
4.4	Discussion	47
5	Modelling the effect of acute Aβ on synaptic transmission	51
5.1	The mEPSC Model	51
5.1.1	Method Overview	51
5.1.2	Model Set-up	52
5.1.3	Parameter Sensitivity Analysis	54
5.2	Model Fitting	55
5.2.1	Simulating mEPSC Amplitude Variability	55
5.2.2	Simulating the A β Effect	60
5.3	Discussion	61
6	Modelling altered intrinsic excitability in a transgenic mouse model of AD	65
6.1	Background	65
6.1.1	A β and Altered Intrinsic Excitability	65
6.1.2	Na ⁺ Channels	66
6.2	Model-Data Fitting Method	66
6.2.1	Intrinsic Excitability Data Summary	67
6.2.2	The Models	69
6.2.3	Fitting Method	72

6.3	Model Fitting Results	74
6.3.1	Single Na ⁺ Channel Model	74
6.3.2	Split Na ⁺ Channel Model	76
6.4	Discussion	81
7	Investigating the impact of Aβ-related changes in neuronal activity on gamma frequency oscillations	83
7.1	Gamma Oscillations in the Hippocampus	83
7.2	The EI Network Model	84
7.2.1	Network Model Set-Up	84
7.2.2	Network Activity Measures	85
7.2.3	Original and Extended Network Behaviour	85
7.3	Robustness of the Network Oscillations	86
7.3.1	The Robustness Tests	86
7.3.2	Robustness Test Results	89
7.4	Incorporating the Effects of A β	98
7.4.1	Altered Intrinsic Excitability	98
7.4.2	Altered Synaptic Strength	102
7.5	Discussion	107
8	Discussion	109
A	Appendix A	111
B	Appendix B	113
C	Appendix C	115
	Bibliography	117

LIST OF TABLES

TABLE	Page
6.1 CA1 pyramidal neuron model parameters: WT-fitted values vs. initial values . . .	74
6.2 Single Na ⁺ channel CA1 neuron model: voltage-gated ion channel parameters . .	76
6.3 Split Na ⁺ channel CA1 neuron model: voltage-gated ion channel parameters . . .	79
C.1 Initial AMPAR parameters fitted to CA3 EPSCs from [61]	115
C.2 EI Network properties	115

LIST OF FIGURES

FIGURE	Page
2.1 The hippocampus and its location	12
2.2 The hippocampal circuit	13
3.1 Chapter model use guide	22
3.2 Example equivalence circuit of a neuron	26
3.3 The excitatory-inhibitory network model structure	31
4.1 A β infusion increases EPSC amplitude	35
4.2 Example mEPSC recording	38
4.3 A typical cultured hippocampal slice	39
4.4 A β oligomer size distribution in working solution	40
4.5 Electrophysiology rig infographic	42
4.6 Photos of the electrophysiology rig	43
4.7 Miniature EPSC measures	44
4.8 Recorded mEPSC amplitude and frequency distributions	46
4.9 Recorded mEPSC kinetics	48
5.1 Example mEPSC simulations	53
5.2 mEPSC model: fraction of open receptors profile	54
5.3 mEPSC synapse model: parameter sensitivity	56
5.4 Example fits of simulated mEPSCs to data	57
5.5 Fitted mEPSC parameter distributions and their correlation with the mEPSC amplitudes	58
5.6 mEPSC amplitude distribution with variability only in γ	59
5.7 Input and output of the parameterised mEPSC Control model	60
5.8 Increased synaptic conductance simulated A β -mediated increase in mEPSC amplitude	61

LIST OF FIGURES

6.1	Average hyperpolarised traces recorded in WT and PDAPP CA1 neurons	68
6.2	Action potential and typical firing pattern in WT and PDAPP neurons	69
6.3	Pyramidal neuron model behaviour with initial parameterisation	70
6.4	Published Na ⁺ ion channel kinetics	71
6.5	Single Na ⁺ model ion channel kinetics	75
6.6	PN model-data comparison: single Na ⁺ channel	77
6.7	Split Na ⁺ model Na _v 1.2 and Na _v 1.6 channel kinetics	78
6.8	PN model-data comparison: split Na ⁺ -channel	80
7.1	Behaviour of the different EI network models	87
7.2	The effect of increasing network size on network behaviour	90
7.3	The effect of increasing network connectivity on network behaviour	91
7.4	The effect of altering the E:I cell ratio on network behaviour	92
7.5	The effect of increasing the synaptic noise strength on network behaviour	93
7.6	The effect of increasing the synaptic noise frequency on network behaviour	95
7.7	The effect of altering the stimulation current on network behaviour	95
7.8	The effect of altering the synaptic strength distribution on network behaviour	97
7.9	The effect of adding heterogeneity to the E-cell population on network behaviour	97
7.10	Comparison of the gamma oscillations generated in the WT and PDAPP networks	99
7.11	The robustness of the PDAPP vs. WT network response to alterations in the network properties	100
7.12	The effect of excitatory synapse loss on the WT and PDAPP network behaviour	101
7.13	The effect of altering the excitatory synaptic conductance on network behaviour	103
7.14	Comparison of the gamma oscillations generated when the excitatory synaptic conductance is increased by 50%	104
7.15	Testing the robustness of the network response to increased excitatory synaptic conductance	106
7.16	The effect of altering the fraction of strengthened excitatory synapses on network behaviour	107
A.1	The average seal resistance recorded during the mEPSC experiments	111
A.2	mEPSC half-width and decay time correlation	112
A.3	Network model neurotransmitter release	112

INTRODUCTION

In 2012 the World Health Organisation highlighted dementia as a global public health priority due to its significant personal, social and economic impacts [253]. Currently, approximately 47 million people worldwide suffer from dementia, which is estimated to cost over one trillion American dollars, equivalent to 1% of the global GDP [189]. Dementia is a syndrome associated with the progressive deterioration of cognitive function caused by many different neurological diseases. Of these, the most common is Alzheimer's disease (AD), a terminal, age-related neurodegenerative disease that accounts for 60 - 70% of all dementia cases [3]. Forecasts predict that the number of people with AD will surpass 100 million by 2050 as a result of the ageing population [28]. Consequently, AD is a primary focus in the global action against dementia. However, despite extensive international research efforts, there is still no cure or treatment that can prevent the progression of AD [97, 136].

Essential to the development of treatments that can halt or slow the progression of AD is an understanding of the underlying pathological processes. The challenge lies in unravelling the inherently complex pathophysiology of AD, which is now believed to have several subtypes [171, 190]. Many neuropathological changes have been associated with AD, from sub-cellular through to network level dysfunction [112, 181, 214]; the aim is to identify the mechanisms underlying these changes, to determine how they interrelate and contribute to the disease progression and to place them within a temporal sequence of pathogenesis [210]. However, these pathological changes occur on different spatial scales, evolve on vastly different time scales and are recorded with distinct types of data. Though they contribute to

the understanding of AD pathology, such observations produce a fragmented picture of the disease that is complex and therefore challenging to integrate into a coherent model.

There is a growing interest within AD research in the benefits of using ‘systems’ approaches, which integrate experimental data with computational and mathematical modelling [78, 79, 197]. The idea is that to understand a complex system it is not sufficient to only consider the underlying parts in isolation, but is also necessary to consider how they interact to generate higher-level processes. By integrating experimental data with multi-scale computational models it is possible to explore the behaviour of a particular biological process at multiple temporal and spatial scales in relation to its underlying components. Recent publications have highlighted how this multidisciplinary approach is essential for developing a more complete picture of AD, necessary for identifying drug-targets and for the development of effective treatments [78, 79, 197].

This systems approach is the underlying premise of this thesis, with a particular focus on how multiscale computational models can be used to investigate the underlying mechanisms and functional impact of AD-related changes in neural activity. Neural activity refers to the propagation and processing of electrical impulses at both the individual neuron level and across neuronal populations and brain regions and is fundamental to brain function. There is a large body of research that focusses on the impacts of AD on synaptic, neuronal and network-level activity. Given the dynamic interconnected nature of the brain, determining how altered activity interacts and contributes to AD pathology is extremely challenging. Biophysical mathematical models have been developed that can simulate neural activity across different biological scales, from sub-cellular to network level activity. By integrating this experimental data with mathematical models, more insight can be gained about both the cause and functional consequence of these pathological changes.

This approach provides the framework for this thesis; biophysical models are used to explore the cause and impact of observed changes in neural activity driven by amyloid- β ($A\beta$), a protein believed to play a significant, if not causative role in the early stages of AD pathology. First, individual models of an excitatory synapse and a pyramidal neuron are used to investigate the processes underlying $A\beta$ -related changes in synaptic transmission and cell excitability recorded in the CA1 region of the hippocampus, which is a locus of learning and memory function and also presents significant neurodegeneration in AD. These data-informed models are then individually incorporated into a network model to investigate the potential functional implications of these changes on higher-level neural activity, specifically

on gamma frequency oscillations which play an important role functional activity in the CA1. By using models to simulate the recorded activity, the aim is that more insight about the impacts of $A\beta$ can be gained from the data and extrapolated in ways not possible experimentally.

1.1 Thesis Overview

Chapter 2 This chapter provides an overview of Alzheimer's disease (AD), introducing its defining characteristics, with the aim of highlighting the importance of $A\beta$ and why AD research focusses on the hippocampal region and the CA1 specifically. The hippocampal structure is then described in more detail. Subsequently, a review of AD research papers that use data informed computational models are discussed, with a specific focus on those studies that have investigated how changes in the properties of the cell alter synaptic, cellular and network level activity.

Chapter 3 In this chapter the computational methods used in this thesis are presented. These include: a kinetic synapse model used to simulate spontaneous synaptic activity; a single-compartment conductance-based neuronal model of a CA1 pyramidal neuron used to simulate the intrinsic excitability obtained from experimental recordings; an excitatory-inhibitory (E-I) network model, built using the single-compartment neuronal model (E-cell) and a fast-spiking interneuron model (I-cell), which is used to simulate gamma activity to investigate how synaptic changes alter network activity.

Chapter 4 This chapter reports on the experimental work carried out, presenting the electrophysiology recordings of miniature excitatory post-synaptic currents (mEPSCs) following acute $A\beta$ infusion into CA1 pyramidal neurons in cultured hippocampal slices. First, a background to the work is given that outlines: the evidence linking $A\beta$ to synaptic dysfunction; the published research that was a precursor to the work in this thesis, which suggested that the initial response to intracellular $A\beta$ caused an increase in CP-AMPA synaptic transmission; the main properties of AMPARs and miniature EPSCs. Then the experimental electrophysiology method used to record mEPSCs is described and the results obtained are presented.

- Chapter 5** In this chapter a first-order kinetic model is fit to the mEPSC data presented in the previous chapter to investigate the mechanisms underlying the changes in synaptic transmission. The chapter begins with a description of the first-order kinetic model used to simulate synaptic transmission. First the model set-up used to simulate AMPAR-mediated mEPSCs is described followed by an analytical and numerical analysis of its behaviour, focussing on the relation between the model parameters and the simulated mEPSCs. Subsequently, the development of the ‘control’ model is explained, including the method used for fitting the model to the mEPSCs recorded from untreated cells and the results of the distribution analysis that is used to identify the relationship between the fitted parameters and mEPSC amplitude. Finally, the results from altering the synaptic conductance of the model to reproduce the A β treated data are presented.
- Chapter 6** This chapter presents the development of a single compartment CA1 pyramidal model used to simulate published intrinsic excitability data recorded from wild type and PDAPP transgenic mice, which over express A β . First, the data is described followed by the model fitting method. Subsequently, the original CA1 neuron model and a more biologically realistic CA1 model with two transient sodium channels, which can both reproduce the simulated intrinsic excitability recordings, are fitted to the published data. This model is then used to attempt to reproduce the changes observed in a mouse model of amyloidopathy in order to suggest what alterations to the properties of the cell may underlie those changes.
- Chapter 7** In this chapter a biophysical excitatory-inhibitory network model is developed to explore the potential impacts of the A β -related alterations, described in the previous chapters, on gamma frequency oscillations. First, the network settings, output measures and behaviour of the base model used to simulate gamma activity are described. Subsequently robustness tests are carried out to investigate the dependence of the gamma oscillation generation on the parameter settings. The network model is then used to independently investigate the impact of altered excitatory synaptic transmission and intrinsic neuronal excitability on the network activity.
- Chapter 8** In the final chapter of the thesis the work is discussed within the context of A β -research and more generally with regards to the multiscale computa-

tional modelling approach to Alzheimer's disease. Ideas for future work that lead on from the work presented in this thesis are also discussed.

1.2 Thesis Contributions

- Through whole-cell recordings from CA1 hippocampal neurons it was found that direct intracellular infusion of amyloid beta ($A\beta$) oligomers rapidly enhances AMPAR-mediated mEPSC amplitude, thereby supporting previous findings which recorded a similar increase in evoked EPSC amplitude. This finding contributes to current knowledge on the initial effect of $A\beta$ oligomers on excitatory synapses in pyramidal neurons.
- By using a simple kinetic model of the synapse that could simulate mEPSCs it was possible to investigate the consequence of the synaptic effect of $A\beta$ described above on network-level activity. It was found that a 50% increase in the synaptic conductance could account for the effect of $A\beta$ and that this could lead to an increase in the gamma power of oscillations generated within an excitatory-inhibitory (E-I) neuronal network. This contributes to the current understanding of the functional effect of $A\beta$ related synaptic changes.
- A previously established single-compartment conductance-based CA1 pyramidal neuron model was extended by adding a second Na^+ -current as well as fitting to previously recorded intrinsic excitability data. It was shown that this model can be used to simulate and investigate the underlying changes that cause altered excitability in CA1 neurons of an $A\beta$ -overproducing mouse model (PDAPP-type). These improved and more biophysically realistic models can be used in further CA1 neuron studies and incorporated in a network model to further investigate $A\beta$ -related changes.

BACKGROUND

2.1 Alzheimer's Disease: An Overview

Alzheimer's disease was first described by Alois Alzheimer as an "unusual disease of the cerebral cortex" in his 1907 report on the case of a fifty-one year old female psychiatric patient that he had followed from hospital admittance until her death four years later [224]. The patient presented with paranoia, memory loss and disorientation followed by progressive cognitive and physical deterioration. In his post-mortem observations Alzheimer presciently identified histological features that are now recognised as defining features of AD. Specifically, he described significant atrophy of the brain and two abnormal lesions: intracellular neurofibrillary tangles and "minute military foci" distributed throughout the cortex which are now known as amyloid (or senile) plaques. Overall, these observations cover the characteristic features of AD which have provided the underpinnings for AD research.

In the years since Alois Alzheimer's discovery, a vast amount of research has been undertaken to determine the pathological processes that underlie AD. What has emerged is that AD is a complex and multifactorial disease; fundamental questions remain about the cause (aetiology) and progression (pathogenesis) of AD, and models of the disease that have been proposed remain under debate [212]. The following section provides a brief overview of the key aspects of AD pathology.

Disease Aetiology

In the vast majority of AD cases the exact reason why an individual develops the disease is unknown. There are rare inherited forms, accounting for less than 1% of all AD cases, that are directly associated with autosomal dominant mutations in one of three specific genes: APP, PSEN1 and PSEN2. These familial Alzheimer's disease (FAD) cases have provided valuable insight into AD pathogenesis as they are the only direct causal factors that have been identified [13]. In all remaining cases what triggers the onset of the disease is undetermined but several risk factors have been identified that increase the likelihood of an individual developing AD. The greatest known risk factor for AD is age; over 95% of all cases are in individuals over 65 years old, although AD has been diagnosed in people as young as 30 years old [28]. Family history is also a significant risk factor and is found in approximately 25% of all late-onset AD cases [18]. Several genes have been identified that increase AD susceptibility, with the greatest genetic risk associated with the Apolipoprotein A (APOE) ϵ 4 allele [48, 68, 150]. General health factors, such as diabetes, obesity, high blood cholesterol, depression, and physical inactivity, are also believed to increase the risk of developing AD [12, 55].

Clinical Symptoms

Clinically, AD is characterised by a gradual decline in cognitive ability with specific deficits in episodic memory (the memory associated with autobiographical events) [65]. Typically these impairments in memory are the first symptoms reported and continue to worsen throughout the disease. As the disease progresses other aspects of cognition, such as orientation and reasoning, become affected and eventually motor functions also become impaired, ultimately leading to the death of the patient [162]. The rate of cognitive decline varies significantly, with average life expectancy from point of diagnosis ranging from 8 - 10 years with diagnosis at 65 years old, to less than 3 years with diagnosis at 90 years old [259].

The decline in cognitive function is caused by the progressive deterioration of neural tissue. Post-mortem studies have shown that this neurodegeneration, although widespread by the end of the disease, targets specific brain areas [238] and has a distinct pattern of progression [26]. The development of clinical symptoms correlates with the location and severity of the neurodegeneration [111]. However it is believed that AD actually begins years before the onset of clinical symptoms, which occur once the neurodegeneration has become sufficient to impair function [167].

Neuropathological Features

Autopsies of severe AD brains display several characteristic neuropathological features: significant cortical atrophy, primarily caused by neuronal loss [232]; loss of synapses [56, 95] and two types of abnormal protein aggregations, intracellular neurofibrillary tangles (NFTs) of hyper-phosphorylated forms of the protein tau [92] and extracellular amyloid plaques composed of the protein amyloid-beta ($A\beta$) [84, 160]. Plaques and NFTs must be present for the confirmation of an AD diagnosis [65]. Together these characteristic features provide insight into the pathology of AD: the regions of the brain that it targets, how it progresses, and the potential causative factors.

Post-mortem studies have found that the largest amounts of neuronal loss occur in the medial temporal lobe [31] and connected areas in the association neo-cortex [183]. The medial temporal lobe contains the hippocampal formation and the entorhinal, perirhinal and parahippocampal cortices (see Figure 2.1). The highest levels of neuronal loss occur in the hippocampal formation which plays an essential role in spatial and episodic memory, which (as mentioned above) is characteristically impaired in AD [114, 247].

The same regions that are associated with neuronal loss also exhibit significant synapse loss [56, 95]. This reduction is greater than that which would be expected given the amount of neuronal loss [54] and has been found to be more strongly correlated with cognitive impairment. Synapse loss is in fact the strongest neuropathological correlate for the severity of cognitive impairments in AD [57, 195, 231] and is observed in the early stages of the disease [56, 205, 231]. Consequently, synaptic degeneration is believed to play a crucial role in the development of AD pathology [211, 219].

The highest concentrations of plaques and tangles are also observed in the medial temporal lobe and other AD-related areas. The NFT distribution has a characteristic pattern of progression, progressing from the entorhinal cortex to the hippocampus to the other cortical regions, which correlates well with the locations affected by neuronal atrophy. Consequently, NFT distribution has been used as a way to stage the disease [26]. Amyloid plaques, in comparison, are more widely distributed and the number of plaques does not correlate with the amount of neuronal atrophy or the severity of the disease [196, 232]. However, the aggregation of $A\beta$ into plaques mostly occurs prior to the onset of symptoms and therefore $A\beta$ pathology is thought to be upstream of tau [19, 214]. Consequently, these abnormal aggregations and the constituent proteins, $A\beta$ and tau, have been key focuses of AD research [172, 221].

2.1.1 The Amyloid-beta hypothesis

Origins

Amyloid-beta ($A\beta$), a 36-43 amino acid peptide, has been one of the primary focuses in AD research since it was first sequenced from the senile plaques found in AD patients by Glenner and Wong in 1984 [84, 85]. It had already been observed that Down's syndrome patients, who have a high risk of dementia, invariably develop both plaques and NFTs [34]. Glenner and Wong discovered that the same amyloidogenic protein ($A\beta$) was found in the meningeal blood vessels (and subsequently also in the plaques [160]) of both AD and Down's syndrome patients, confirming that they presented the same neuropathology. As Down's syndrome was known to be associated with an extra copy of chromosome 21 they predicted that the genetic defect in AD that causes the pathological production of $A\beta$ may also be located on chromosome 21 [85]. Subsequently, it was discovered that $A\beta$ is produced by the cleavage of the larger amyloid precursor protein (APP) that is located on chromosome 21 [121].

These discoveries, combined with the evidence from familial Alzheimer's disease (FAD) of mutations in genes related to APP [86, 146], strengthened the hypothesis that $A\beta$ had a central role in AD [98, 210]. Subsequently in 1992 Hardy and Higgins published their amyloid cascade hypothesis, proposing that aberrant $A\beta$ accumulation is the primary cause of the neurodegeneration observed in AD, triggering a pathological cascade that leads to neurofibrillary tangles, cell loss, vascular damage and dementia [99]. In the 30 years since, this hypothesis has remained the dominant theory of AD pathogenesis [213].

Amyloid-beta

There are two main forms of $A\beta$ within the brain: the 40-residue peptide ($A\beta$ 1-40) and the 42-residue peptide ($A\beta$ 1-42), which respectively account for approximately 10% and 90% of all cerebral $A\beta$ [170]. Of these two forms $A\beta$ 1-42 has been the main research focus due to its disproportionate increase in the genetic mutations associated with familial Alzheimer's disease (FAD) [22] and because it has been found to be more neurotoxic than $A\beta$ 1-40 [132].

Individual $A\beta$ 1-42 monomers have a high propensity to aggregate and can self-assemble, initially forming small soluble oligomers, which contain a small number of monomers [82], and eventually forming larger aggregations such as fibrils and plaques [32, 100]. Although plaques are the visible hallmark of AD, as previously mentioned they have low correspondence with the severity of the disease and the location of neuronal atrophy [8, 232]. The

concentration of soluble A β 1-42 oligomers, however, have a unique distribution in the human AD brain distinct from the amyloid fibrils and plaques [126] that correlates better with disease severity markers [153, 163, 175]. It has also been observed that the concentration of soluble A β 1-42 oligomers increases in the cerebrospinal fluid (CSF) and hippocampus of AD sufferers [30, 202]. Consequently, the focus has been on these smaller A β aggregations which precede the formation of extracellular plaques.

It has been proposed that the intracellular accumulation of A β oligomers plays an important role in AD pathogenesis [140]. Several studies have shown evidence that A β oligomerisation occurs intraneuronally [179, 227, 242] and that these intraneuronal A β aggregates can seed amyloid fibril growth [110]. In addition, extracellular A β , particularly soluble A β oligomers, can be sequestered by neuronal cells [43, 106, 173]. Importantly, it has been observed that soluble A β 1-42 oligomers can accumulate at synapses providing a key link to AD synaptic pathology [14, 221, 227]. Notably, A β oligomers have been found in increased numbers in the synapses near plaques in the brains of patients with AD, but not in the synapses near the plaques in those without AD [17, 134]. Given the fact that plaques begin to appear 15 - 20 years before clinical onset this suggests that these oligomeric forms are present in the very early stages of AD.

Although much evidence has been gathered that corroborates the amyloid hypothesis, it is important to recognise that issues have been raised that challenge it [103, 122, 154, 182]. For example amyloid plaques are found in aged brains with no symptoms of dementia; transgenic mice models that only over-express A β only develop some AD-like symptoms, suggesting that A β is "necessary but not sufficient" to cause AD [172]; and perhaps most significantly, there has been no success to date in drugs trials, the vast majority of which target A β [182]. As a result of this, there is an ongoing debate about the role of A β in AD and whether it is indeed the primary mediator of AD pathogenesis. Several other theories, such as the cholinergic hypothesis [96], exist and are also being explored in AD research. Nevertheless, what is evident is that A β dysregulation is a very early event in AD pathology and is most likely a key factor of the downstream processes that lead to AD neurodegeneration, hence the need to fully understand the pathological impacts and the processes underlying A β pathology [172, 213].

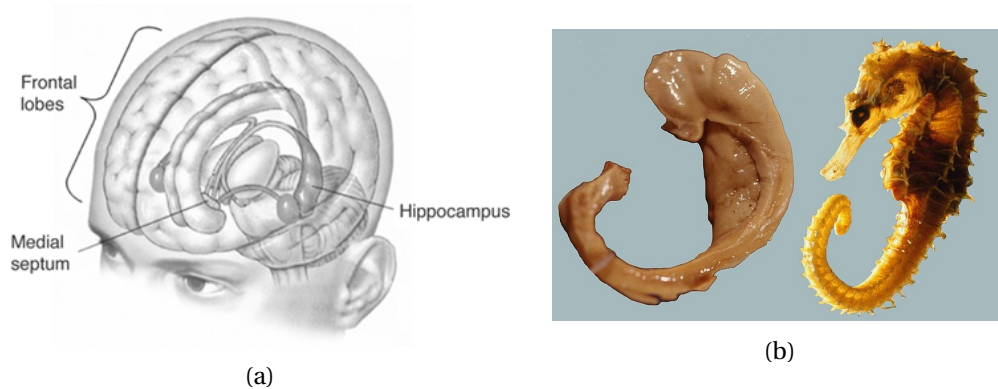


Figure 2.1 | The hippocampus and its location. (a) The hippocampi are mirrored on each brain hemisphere within the temporal lobes (Source: Wikimedia/Creative Commons) (b) Picture of a prepared human hippocampus, so named because of the similarity in its shape to a seahorse (*hippocampus* in greek). Photo: Laszlo Seress' preparation of a human hippocampus alongside a sea horse (1980). Source: Wikimedia/Creative Commons

2.2 The Hippocampus

2.2.1 Hippocampal Structure

The hippocampus, which means 'seahorse' in Ancient Greek, is named after its distinctive shape (see Figure 2.1). It is located within the medial temporal lobe, which also includes the entorhinal, perirhinal and parahippocampal cortices. Due to bilateral symmetry there are two mirrored hippocampi on either side of the brain hemisphere, which are centrally connected by the commissure of fornix.

The hippocampus has a highly organised structure, with clearly defined neuronal layers and regions of connectivity. This structure has led to the identification of five hippocampal subfields regions, the Dentate Gyrus (DG), the four Cornu Ammonis (CA) subfields CA1 - CA4 and the subiculum. The majority of the connections between these subfields lie on the same plane as a hippocampal cross-section and form highly directional neural pathways [4]. This is advantageous for hippocampal research as it means that the main aspects of the hippocampal circuit are preserved in a hippocampal slice (a cross-section of a few hundred microns thick) [218]. The key regions and pathways of the hippocampal circuit are shown in Figure 2.2.

The majority of the information routes in and out of the hippocampal circuit are transmitted via the entorhinal cortex (EC), forming a closed loop. There are two main neural

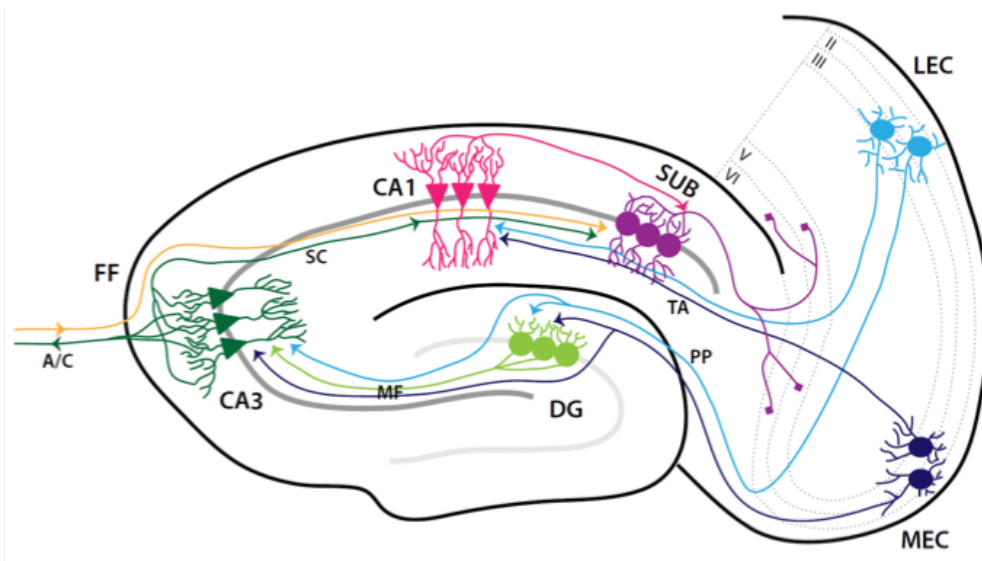


Figure 2.2 | The hippocampal circuit. A schematic showing the well defined circuitry of the hippocampal formation, which is maintained within a transverse hippocampal slice (figure created by B. Winters [252])

pathways that transmit signals from the EC to the hippocampus. These are the perforant pathway (PP), which propagates signals from the EC to the DG and CA3 subfields and the temporoammonic pathway (TA), which connects the EC to the CA1 via the subiculum [4]. Internally, the hippocampus is connected by what is known as the tri-synaptic circuit, which connects the DG, CA3 and CA1 subfields. The two pathways that make up the tri-synaptic circuit are the mossy fiber pathway (MF), which connects the DG to the CA3, and the Schaffer collateral pathway (SC), which projects from the CA3 to CA1. The hippocampus also receives input from the medial septum via the septal nuclei, which connect to the DG, CA3 and CA1 regions. The septal inputs are mostly cholinergic and GABAergic [74].

Output signals from the hippocampus originate from the CA1 subfield, and pass via the subiculum to the EC, closing the loop. There are also direct connections in both directions between the CA1 and the EC and to neocortical areas, such as the perirhinal and postrhinal cortex [76]. Overall, this means that the CA1 sub-region is the primary source of all feed-forward projections out of the hippocampus [237].

2.2.2 Oscillations in the Hippocampus

Neural oscillations are an inherent feature of brain activity. They reflect the rhythmic fluctuations of neural activity that occur within and across brain regions. This synchronised

behaviour is believed to have a fundamental role in cognitive functions, such as learning and memory, and other neural processes [45, 243]. Synchronised neural activity (cell firing) generates an oscillatory external electric field that can be measured. These fluctuations can be observed from small neuronal populations using local field potential (LFP) recordings and can be measured on a larger scale (brain-wide) using electroencephalographic (EEG) recordings. As LFP recordings are invasive, *in vivo* studies of neural oscillations within humans are usually limited to external scalp EEG recordings, although intracranial EEG (iEEG) which can provide better resolution are sometime used [91, 133, 143]. However, similar neural oscillation patterns are observed in other primates and mammals, which has enabled more detailed *in vivo* and *in vitro* studies into the mechanisms that underlie the generation of these oscillations and their function in neural processes [38, 239, 256].

Neural oscillations have a frequency spectrum that spans five orders of magnitude from 0.05 Hz to 500 Hz [39]. This spectrum has been divided into different frequency bands: the slow oscillations (<1 Hz), delta rhythm (1 - 4 Hz), theta rhythm (4 - 8 Hz), alpha rhythm (8 - 12 Hz), the beta rhythm (12 - 30 Hz), the gamma rhythm (30 - 120 Hz) and high-frequency oscillations which are associated with sharp-wave ripples (120 - 200 Hz) and fast ripples (200 - 500 Hz). EEG and LFP recordings from human and other mammals have indicated that different brain regions support oscillations of different frequencies and that the oscillation frequency and region involved depends on the specific task that is being carried out [35, 120, 128, 158, 245].

The main brain rhythms that are detected within the hippocampus are theta frequency oscillations, gamma frequency oscillations and sharp-wave ripple complexes [45]. The presence of these rhythms has been found to correspond with specific behaviours and is therefore believed to have distinct roles in hippocampal processing. For example, the theta rhythm has been associated with navigation and memory encoding [36, 44], the gamma rhythm with learning and memory [27, 70, 107], whilst SWRs are associated with memory consolidation [11, 37]. The cross-frequency interactions or coupling of oscillations is also believed to facilitate neural processing; phase-amplitude coupling (nesting) of theta and gamma frequency oscillations has been observed in both humans and animal models and appears important in memory encoding [91, 143, 148, 233].

The CA1 is a locus of gamma oscillations in the hippocampus and they have been well characterised in this region through both *in vivo* and *in vitro* studies [47, 51, 166]. The oscillations can be split into low (25 - 60 Hz) and high frequency oscillations (55 - 100 Hz),

which are believed to correspond with inputs from different regions; low frequency gamma leads to increased coherence with inputs from the CA3 whereas the higher frequency is associated with increased coherence with the EC [46, 207].

Gamma oscillations are often nested within a theta oscillation. It is believed that theta-gamma nesting provides a gating mechanism for different inputs to the hippocampus by providing entrainment with either the EC or DG [27, 46, 207]. In humans the theta-gamma phase-amplitude coupling increases during the acquisition of episodic memories [143]. Reducing the theta-gamma coupling has been found to impair memory retrieval performance [217]. There is also a lot of study about the formation of cell assemblies in the CA1 by theta-nested gamma as it has been proposed that they play an important role in the encoding and retrieval of memories [64].

The evidence for the role of gamma frequency oscillations in memory formation is twofold. First, it has been observed in both humans and in animal studies that an increase in hippocampal gamma activity accompanies successful memory task performances [120, 209, 239, 256]. Secondly, the disruption of hippocampal gamma activity in animal model studies has been found to reduce memory performance [75, 217, 256]. Combined, these observations support the hypothesis that gamma oscillations have a functional role in memory processing in the hippocampus.

2.2.3 AD and the Hippocampus

As previously mentioned, an early characteristic symptom of AD is a distinct impairment in recent episodic memory function. Episodic memory is a distinct cerebral function associated with the hippocampal formation [223]. It is now widely accepted that the hippocampus has a significant role in the encoding of new episodic memories, acting as a mediator for the transfer of new memories to long-term storage [169]. Current theories also posit that the hippocampus is involved in recent memory retrieval but opinions differ as to whether this involvement is required in remote memory retrieval [257]. The hippocampus is also associated with spatial memory which deteriorates in AD [145, 180].

Both neuronal loss and NFTs are found in the EC in the very mild stages of the disease and then progress to the hippocampus before spreading to other cortical regions [88, 129]. The greatest amounts of neurodegeneration occur in the neurons that interconnect the hippocampal formation with other areas of the cortex, particularly those in the CA1 region which is the primary area that relays hippocampal output to the surrounding cortices [247].

Due to the susceptibility of the CA1 region to AD [246], a lot of research has focused on the changes within this region.

2.3 Computational Models of AD

AD is associated with progressive synaptic and neuronal dysfunction. The following examples demonstrate the insight that biophysical models of single cell and network level neural dynamics that incorporate these experimental changes can bring to AD research. The majority of these studies focus on those regions that are affected in the early stages of AD, namely the hippocampus and thalamus and their associated networks. The models of individual neuron activity have simulated AD-related changes in the hippocampal CA1 or CA3 neuronal populations, primarily because these models are well developed and a lot of AD research has focused on change in these cells. Obviously the effects of AD are far more wide spread and affect many different neuronal types. There are already many models of different cell types and regions ready for use but as the field develops and knowledge accumulates about the structural connectivity (connectome) of other neural regions and about the electrophysiological properties of other cell types, further studies that follow along the lines of investigation discussed here could be carried out.

2.3.1 Modelling Neuronal-level Dysfunction

Signal processing within a neuron is related to changes in the cell's membrane potential that occur as a result of ion flow across the cell membrane and synaptic transmission. Biophysical neuron models that incorporate these intrinsic neuronal properties (e.g. ion channels) can be used to simulate the signalling dynamics within the cell. Numerous AD-related modifications in synaptic and cellular properties have been recorded, such as altered ion channel expression [29, 255], increased synaptic release probability [1, 230], and altered synaptic receptor profiles [138, 215, 248]. By incorporating these experimental observations into biophysical neuron models it is possible to investigate how these AD-related changes in cell properties affect the signalling properties of the neurons. To date, modelling studies have been carried out that investigate the effects on neuronal signal processing of reduced Na^+ and K^+ ion channel conductance, altered Ca^{2+} dynamics (caused by the K^+ -channel inhibition), increased membrane conductance, and decreased synaptic release.

Ion Channel Dysfunction

Several studies have investigated the impact of A β -related dysregulation of ion channel function [90, 168, 250]. A cell's excitability, which is its ability to generate action potentials in response to a stimulus [116], is (in part) determined by the relative contributions of the different ionic currents; a single compartment biophysical model of a pyramidal neuron with the same set of ion channels but with different conductances is able to reproduce the different excitability profiles of CA3 and CA1 neurons [178]. This model was also used to investigate the sensitivity of the fitted pyramidal neuron model to changes in ion channel conductance. They found that reducing K⁺ and Na⁺ channel conductance enhanced the neuron's excitability. Although this Na⁺ effect is counterintuitive, given that Na⁺ activation enables the rapid depolarisation of the cell during an action potential, it is in agreement with *in vitro* observations from an AD mouse model that displays decreased Na⁺ currents [29].

The dysregulation of Ca²⁺ dynamics is believed to play a fundamental role in AD-related neurodegeneration. It has been established that A β can destabilise calcium homeostasis but the underlying mechanisms are still in question [7, 142, 187]. Several studies have used biophysical neuron models to investigate how A β -related reduced K⁺-channel conductance can affect neuronal calcium dynamics. A link between the fast-inactivating A-type potassium channel (I_A) and calcium dynamics was first identified in an early modelling study by Good *et al.* [90]. They simulated a hippocampal neuron using a Hodgkin-Huxley-based "wrinkled"-sphere model, with a calcium diffusion model and synaptic receptors, to investigate how A β -related K⁺-channel inhibition would affect intracellular Ca²⁺ levels and excitability [90]. They found that modelling increasing levels of A β as a decrease in K⁺ lead to increased excitability and an increase in/influx of intracellular calcium in agreement with their experimental observations, suggesting that K⁺-channel inhibition could be a pathway for A β -mediated Ca²⁺ dysregulation.

A more recent study probed the intracellular effects of K⁺-channel inhibition in more detail [168]. Previous electrophysiology work, measuring from the soma and apical dendrite, had indicated that A β block of A-type K⁺ currents caused enhanced back-propagating action potentials (bAPs) and increased Ca²⁺ influx [40]. Morse *et al.* used a detailed multi-compartment CA1 pyramidal neuron model (built in NEURON) to further investigate the effects of K⁺-channel inhibition in regions beyond the experimental recording sites, in the distal dendrites. They found that the bAPs induce hyperexcitability and enhance Ca²⁺-levels across the cell, with increased sensitivity to K⁺-channel blockage in the oblique dendrites. This work suggests a potential mechanisms by which the distal dendrites are selectively

vulnerable in A β and may be the first parts of the cell to malfunction and degenerate, which given their role in neuronal signal processing could mean that the cell's signalling capacity is altered in the very early stages.

Biophysical neuronal models can be designed to simulate experimental recordings thereby providing outputs that can be experimentally tested and validated. These models can be used to predict how changing different components of the neuron model would affect the output. In a study by Wilson *et al.* they simulated patch clamp experiments (using a similar "wrinkled"-sphere model as Good *et al.*) to investigate if the neuronal signalling generated by two different actions of A β on the cell membrane, specifically the blocking of fast-activating K $^+$ -channels or increased membrane conductance, could be distinguished experimentally [250]. They found that the cell signalling and intracellular Ca $^{2+}$ dynamics were significantly different depending on whether the A β -mediated affect was due to K $^+$ channel alteration or membrane conductance changes. This produced an experimentally testable set of results.

Synaptic Dysfunction

Experimental work has shown that endogenous A β enhances the release probability at CA3-CA1 synapses [1]. In a study by Romani *et al.* they investigate how the enhanced synaptic release probability would alter the cell's ability to process incoming signals using a detailed multi-compartment model of a CA1 pyramidal neuron (built in NEURON) with the addition of a model of short-term synaptic plasticity (Tsodyks 1998 [235]) [198]. They fit the model to experimental recordings of AMPAR-mediated EPSCs in A β -treated and control CA1 neurons, which were generated by APs evoked at 100Hz in the presynaptic CA3 neuron. The recordings from the A β -treated neurons could be reproduced by increasing the pre-synaptic release probability from 0.15 to 0.36. They investigated how this altered synaptic plasticity and integration at different frequencies (5 - 200Hz) and the cells response to 'natural' synaptic stimulation patterns which had been recorded *in vivo* in CA3 neurons. They find that increased synaptic release significantly alters the CA1 neurons firing response and the response to gamma and theta frequency stimulation.

Mixed Dysfunction

The modelling studies discussed in the previous sections simulated neuronal signalling in response to AD-related changes in one neuronal property at a time. However, these changes may be occurring concurrently. Understanding how they combine to alter cell

function is important but can be difficult to determine experimentally. Models can be used to address this issue. Culmone and Migliore investigated how several experimentally observed beta-amyloid related neuronal changes (reduced A- and DR-type K^+ currents, Na^+ current and synaptic conductance) would alter the probability that a neuron would reach the spiking threshold [53]. Using a detailed multi-compartment CA1 model they investigated the individual and combined contributions to the cell's spiking probability as progressively more areas of the cell were affected by $A\beta$. They then tested which of these channels could be targeted to restore the neuronal activity to the healthy level and found that A-type K^+ channel manipulation (or smaller combined changes in Na^+ and A-type K^+ or synaptic conductance) could potentially compensate for the effects of $A\beta$. Although progressive membrane dysfunction may not be realistic as compensation mechanisms may take effect when the cell's activity first begins to decrease, this study illustrates the potential for models to suggest and test therapeutic treatments.

Reverse Modelling

The previously mentioned modelling studies all begin with an identified subcellular effect of AD and then investigate how that property will alter neuronal-level function. Models that simulate experimental recordings can also be used to identify (or validate) processes that may underlie a given observation. For example, in the work by Romani *et al.* they were able to match the experimental observations (EPSC recordings) from control and $A\beta$ -treated neurons by altering the pre-synaptic release probability of the model, which was in agreement with the experimental findings.

Models have also been used alongside experimental work to suggest the sub-cellular level changes that underlie altered activity in mouse model studies [21, 228]. In both these studies the intrinsic excitability properties of CA1 pyramidal neurons in transgenic AD-mouse models and wild-type mice were compared. Using a single-compartment Hodgkin-Huxley type CA1 neuron models they identified which reproduce the differences in the average behaviour recorded in the WT and $A\beta$ -treated cases.

COMPUTATIONAL MODELS

In this thesis mathematical models are used to investigate how $A\beta$ alters neural signalling at three scales within the CA1 region of the hippocampus; at the level of the synapse (Chapter 5), of single cells (Chapter 6) and across a population of connected cells (Chapter 5). Three general types of models are used to achieve this: kinetic synapse models, single-compartment conductance-based neuronal models and an excitatory-inhibitory neural network model. More specifically, in Chapter 5 a first-order kinetic synapse model is used to simulate spontaneous synaptic transmission in a CA1 pyramidal neuron. In Chapter 6 a single-compartment conductance-based neuronal model is used to simulate the intrinsic excitability of a CA1 pyramidal neuron. In Chapter 7, the data-informed models are used in the construction of an excitatory-inhibitory (E-I) neural network model which is used to simulate gamma frequency oscillations within the CA1 region. The E-I network is composed of two synaptically connected neuronal populations, CA1 pyramidal neurons (E) and fast-spiking CA1 interneurons (I), which are represented using single-compartment conductance-based models. A list of the models and which chapters they are used in is given in the table in Figure 3.1.

There were several considerations that influenced the choice of these models. Firstly, for consistency and to facilitate the incorporation of the findings from the synaptic investigations into the network-level simulations, it was desirable that the same synapse and single-cell CA1 model were used to construct the neural-network model. Consequently, the synapse and single-cell models were required to be relatively simple with low computational

	First-order kinetic synapse model	Pyramidal neuron model	Fast-spiking interneuron model
Chapter 5	●		
Chapter 6		●	
Chapter 7	●	●	●

Figure 3.1 | Chapter model use guide. A reference table showing in which chapters the synapse model, pyramidal neuron model and fast-spiking interneuron model are used. All three are used in Chapter 7 in the construction of the EI network model.

costs so that they could be incorporated into a network model whilst also maintaining enough level of detail that they could provide insight into how $A\beta$ may be altering neural signalling. Secondly, the network model needed to be able to generate rhythms that are known to occur within the CA1 region of the hippocampus, specifically gamma frequency oscillations. Finally, it was desirable that the single-cell and network models were flexible and could be extended (or simplified) if necessary for future extensions of the work (beyond this thesis).

In the following sections, a brief overview of each of the modelling approaches is given followed by descriptions of the specific models used for the work in this thesis.

3.1 Model Backgrounds

3.1.1 Ion Channel Gating Mechanisms

All cell membranes contain ion-channels, which are pores formed by intermembrane proteins that allow the influx and efflux of ions (such as potassium K^+ , calcium Ca^{2+} and sodium Na^+) from the extracellular space into the cell [104]. These ion-channels can be permeable to just one type of ion or to several different types. The membrane proteins that form the ion channels have specific conformational states which determine whether the channel

is open, enabling the flow of ions, or closed. Passive ion channels (also known as leakage channels) are always open, whereas active ion channels have 'gates' that determine whether the channel is open or closed. Gated ion channels can have multiple conformational states between open and closed which can affect the flow of ions through the channel, which is otherwise known as the channel conductance.

Ion channels can be classified by their activation/inactivation mechanisms (i.e. what triggers the transition from a non-conducting state to a conducting-state and vice versa). The two main types are: voltage-gated ion channels, where the channel is activated/inactivated by changes in the membrane potential, and ligand-gated ion channels, where the binding/unbinding of extracellular ligands (binding molecules) to the ion channel causes it to open or close respectively. Examples of ligand-gated ion channels are AMPA receptors, NMDA receptors and GABA receptors, all of which are predominantly found in neuronal cells at the post-synaptic terminal. In the case of the voltage-gated ion channels another distinction is made between persistent (non-inactivating) and transient (inactivating) ion channels. Persistent ion channels (e.g. the A-type K^+ channel and the persistent Na^+ channel) only have one type of gate, an activation gate, which has to open for the channel to conduct and then deactivates by closing. The transient ion channels (e.g. the transient Na^+ and Ca^{2+} channels) have two gates, an activation gate and an inactivation gate which has an opposite voltage dependence and therefore inactivates the channel before the activation gate has closed/deactivated. Some voltage-gated ion channels, such as the delayed-rectifier K^+ channel, have very slow time-dependent inactivation so can either be considered as a persistent channel or as a transient channel with a very slowly responding inactivation gate.

Another ion-channel gating mechanism is via secondary messengers, which are intracellular molecules that can activate/inactivate the channels. An example channel of this type is the hyperpolarization-activated, cyclic nucleotide-gated (HCN) channel which is a non-selective cation channel that is activated by intracellular cyclic nucleotides when the cell becomes hyperpolarised. As the activation is still voltage-dependent it can be modelled using the same format as the voltage-gated ion channels. There are several other types of ion-channel gating mechanisms but these are not modelled in this thesis so will not be discussed here.

Kinetic Models of Ion Channel Gating

Ion channel gating can be described using a kinetic Markov scheme similar to that used to model chemical reactions [61]. This approach models the time-dependent transition of the

ion channel between conducting and non-conducting states (which reflects the conformational state of the membrane protein). As with chemical reactions a state diagram can be used to represent the kinetics of the ion channel gating. Below is a diagram representing the most simple first-order kinetic scheme where the gate has only two-states, open O and closed C , and the transition rates between the two states, r_1 and r_2 . For the voltage-gated ion channels the transition rates are dependent on the membrane voltage (V) whereas the ligand-gated ion channel transition rate depend on the ligand (neurotransmitter) concentration [60].



Assuming a short time step where the transition rate remains constant, the probability that the gate is open, y , varies with time according to the following kinetic equation:

$$\begin{aligned} \frac{dy}{dt} &= r_1(1 - y) - r_2y \\ &= \frac{y_\infty - y}{\tau} \end{aligned} \quad (3.2)$$

where

$$y_\infty = \frac{r_1}{r_1 + r_2} \quad \text{and} \quad \tau = \frac{1}{r_1 + r_2} \quad (3.3)$$

y_∞ is the steady state probability at a given voltage or transmitter concentration that is approached exponentially with time constant τ . When considering a large number of identical ion channels y can instead be thought of as the fraction of open channels (rather than as a probability) [59].

Although ion channels have multiple conformational states, gating models with only two-states (open and closed) can provide reasonable fits to data recorded from both ligand-gated ion channels and voltage-gated ion channels. The Hodgkin-Huxley formalism for voltage-gated ion channels (discussed in more detail in the next section) only uses two-state gating models: the state of a given type of ion channel can depend on the gating of a identical activation gates, m and, in the case of transient ion channels, also on b identical inactivation gates, h . In this case the overall ion channel opening probability p_{open} (or fraction of number of open channels) is given by

$$p_{\text{open}} = m^a h^b \quad (3.4)$$

The voltage/transmitter dependent rates of channel activation, deactivation and inactivation (in other words the channel kinetics), and the number of gates used to model specific ion channels have been determined through experimental observations.

3.1.2 Conductance-based Neuronal Models

Conductance-based models use a biophysical representation of the cell membrane to simulate the electrical behaviour of the cell. In these models the cell membrane is represented as an electrical circuit, known as the equivalent circuit, where the different features of the membrane are modelled as electrical components. The cell membrane is represented as a capacitor as the extracellular and intracellular mediums, which are the terminals of the circuit, are conducting whereas the bilipid layer that forms the membrane is insulating. Connected in parallel to the cell membrane capacitor are the conducting ion channels. Active ion channels (both ligand and voltage-gated) are represented as variable resistors. Inactive ion channels and ion pumps (which act together to stabilise the membrane potential) are grouped together into a single leak channel which is represented as a fixed resistor. The ionic concentration gradients across the membrane generate electromotive forces and so are represented as batteries in serial with the ion channel resistor.

The total current that flows across the membrane is generated by the membrane capacitance, $I_C = C_m \frac{dV}{dt}$, and the movement of ions across the membrane (via ion channels and pumps). As the total current across the cell must sum to zero, following Kirchoff's law:

$$C_m \frac{dV}{dt} = I_{v\text{-gated}} + I_{l\text{-gated}} + I_{\text{leak}} \quad (3.5)$$

where $I_{v\text{-gated}}$ is the total current flowing through the voltage-gated ion channels, $I_{l\text{-gated}}$ is the total current flowing through the ligand-gated synaptic receptors, and I_{leak} is the total current passing through the leak channels.

For a given ion channel the current is determined by the reversal potential of the channel (E), which is the membrane potential at which no ions flow through the channel (typically calculated using the Nernst potential), the membrane voltage (V), and the conductance of a channel (g), which reflects how easily the ions can pass through the channel. The channel conductance is determined by the state, p , of the ion channel (i.e. how open or closed it is, see Section 3.1.1) and the maximum possible conductance of the channel \bar{g} when it is fully open. This gives the following equation for the current across an ion channel given a

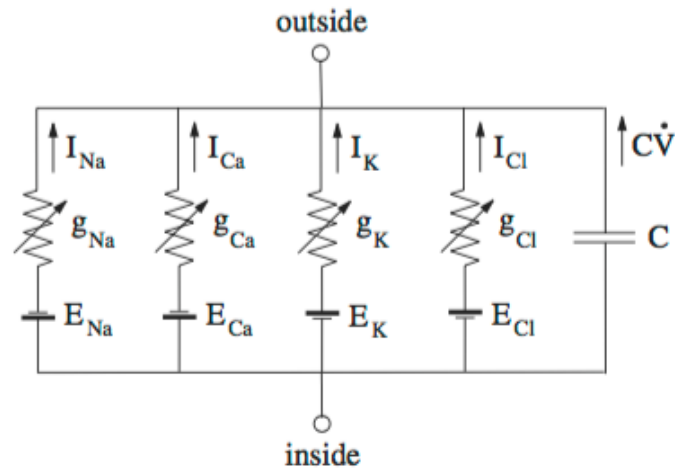


Figure 3.2 | Example equivalent circuit of a neuron. An example equivalent circuit of a neuron where the membrane potential is governed by the current across four ion channels represented in parallel (Na^+ , Ca^{2+} , K^+ and Cl^-) and the membrane capacitance (figure from [116]).

particular membrane voltage:

$$I = g(V - E) \quad (3.6)$$

where

$$g = \bar{g}p \quad (3.7)$$

This approach was first presented in 1952 by Hodgkin and Huxley (H-H) when they modelled the action potential in a giant squid axon. H-H formalism has since become one of the most widely used models in neuroscience [105]. This formalism can be used to generate cell models of varying detail. The simplest version presented above is where the cell is represented as a single-compartment. More complex, multi-compartment models have been developed that take into account the scale and structure of neurons and the distribution of ion channels along the the cell membrane. Models also vary in the number of ion channels that they include. The multi-compartment conductance-based neuron models can provide detailed simulations of neuronal signalling, however they also have higher computational costs.

3.2 Synapse Model

A simple conductance-based kinetic model of a chemical synapse is used in Chapters 5 and 7 to model synaptic transmission. The model is taken from the work by Destexhe et al. [62].

Following the formalisms introduced in Section 3.1.2, the post-synaptic current generated by a synaptic event is given by the following equation:

$$I_{syn,j} = g_{syn} s_{syn}(t)(E_{syn} - V_j) \quad (3.8)$$

where g_{syn} is the maximum conductance of the synapse, s_{syn} is the synaptic gating variable, E_{syn} is the reversal potential of the synapse and V_j is the post-synaptic voltage. The reversal potential of the synapse depends on the type of synapse, for example excitatory AMPA synapses and inhibitory GABA_A synapses (the two types of synapse modelled in this thesis) have reversal potentials of 0 and -80 mV respectively.

The synapse gating variable ($0 < s_{syn} < 1$) is given by:

$$\frac{ds}{dt} = \rho\alpha(1 - s) - \beta s \quad (3.9)$$

where ρ represents the incoming signal, α is the activation rate of the synapse and β the deactivation rate of the synapse.

Two different models are used in this thesis to represent the incoming signal, ρ . The first simulates the post-synaptic response to synaptic transmission at a single synapse. A single synaptic event is represented by a step pulse of neurotransmitter of duration t_x with concentration C_T :

$$\rho = \begin{cases} C_T & \text{if } 0 < t < t_x \\ 0 & \text{otherwise} \end{cases} \quad (3.10)$$

The second model is dependent upon the generation of an action potential in the pre-synaptic cell. The incoming signal is given by a smoothed Heaviside function dependent on voltage of the pre-synaptic, V_i [66]:

$$\rho(V_i) = \frac{1 + \tanh(V_i/4)}{2} \quad (3.11)$$

3.3 Single Cell Models

3.3.1 Pyramidal neuron model

A single-compartment conductance-based pyramidal neuron is used in Chapters 6 and 7. The model is based on the CA1 pyramidal neuron model presented in Nowacki et al. [178],

which included eight fast-activating ionic currents, with the addition of HCN voltage-gated ion channels (I_h) informed by the model in Booth et al. [21]. The eight fast-activating ionic currents included are: a transient Na^+ current (I_{NaT}) and a persistent Na^+ current (I_{NaP}); a transient Ca^{2+} current (I_{CaT}) and a high-voltage activated Ca^{2+} current (I_{CaH}); a delayed-rectifier (I_{KDR}) K^+ current and a M-type K^+ current (I_{KM}), and a leak current (I_L).

The total rate of change in the membrane potential of the system is given by:

$$\frac{dV}{dt} = \frac{1}{C_m} (I_{\text{NaT}} + I_{\text{NaP}} + I_{\text{CaT}} + I_{\text{CaH}} + I_{\text{KDR}} + I_{\text{KM}} + I_h + I_L + I_{\text{stim}}) \quad (3.12)$$

where C_m represents the membrane capacitance and I_{stim} the external input to the neuron.

In Chapter 6 the stimulation current represents an externally applied current as used in electrophysiology protocols. In the network model used in Chapter 7, the cells receive inputs from both synaptic transmission and an externally applied current.

The individual ionic currents (not including the h-current) are modelled by the following equations:

$$I_{\text{NaT}} = g_{\text{NaT}} m_{\text{NaT}}^3 h_{\text{NaT}} (E_{\text{Na}} - V) \quad (3.13)$$

$$I_{\text{NaP}} = g_{\text{NaP}} m_{\text{NaP}} (E_{\text{Na}} - V) \quad (3.14)$$

$$I_{\text{CaT}} = g_{\text{CaT}} m_{\text{CaT}}^2 h_{\text{CaT}} (E_{\text{Ca}} - V) \quad (3.15)$$

$$I_{\text{CaH}} = g_{\text{CaH}} m_{\text{CaH}}^2 h_{\text{CaH}} (E_{\text{Ca}} - V) \quad (3.16)$$

$$I_{\text{KDR}} = g_{\text{KDR}} m_{\text{KDR}} h_{\text{KDR}} (E_{\text{K}} - V) \quad (3.17)$$

$$I_{\text{KM}} = g_{\text{KM}} m_{\text{KM}} (E_{\text{K}} - V) \quad (3.18)$$

$$I_L = g_L (E_L - V) \quad (3.19)$$

where g_* is the maximal conductance of the specific ion channel; m_* and h_* represent the channel activation and inactivation respectively ($0 \leq m/h \leq 1$); V is the membrane potential; and E_* is the ion channel reversal potential.

The activation and inactivation steady states (m_∞ and h_∞ respectively) at voltage V for a given ion-channel are represented with a Boltzman function:

$$\chi_\infty = \frac{1}{1 + \exp(-(V - V_\chi)/k_\chi)} \quad (3.20)$$

where χ represents m or h , V_χ is the ion-channels half-activation/deactivation voltage and k_χ is a constant governing the ion-channels sensitivity to voltage.

The Na^+ channel activation is assumed to be instantaneous, therefore $m_{\text{Na}} = m_{\infty}(V)$. For the other channels with slower activation/inactivation time scales, the rate of change in the ion-channel activation and inactivation is given by:

$$\frac{d\chi}{dt} = \frac{\chi_{\infty} - \chi}{\tau_{\chi}} \quad (3.21)$$

where τ_{χ} is the channel activation/deactivation rate. These are assumed to be constant for all channels except for the transient sodium channel which is given by:

$$\tau_{\chi} = 0.2 + 0.007 \exp(\exp(-(V - 40.6/51.4))) \quad (3.22)$$

The HCN voltage-gated ion channels (I_h) included in the model for the work in Chapter 6 is based on the model given in Booth et al. [21]. The channel activation is separated into a fast, m_{h-f} , and a slow component, m_{h-s} . The current equation is as follows:

$$I_h = g_h p m_{h-f} + (1 - p) m_{h-s} (E_h - V) \quad (3.23)$$

where p represents the fraction of the current generated by the fast-activating component and the channel activation and inactivation functions are given by Equations 3.20 and 3.21.

3.3.2 Fast-spiking interneuron model

The fast-spiking interneuron used in the network model in Chapter 7 is based on the model developed by Wang and Buzsáki et al. [244]. The model includes three ionic currents: one Na^+ current (I_{Na}), one K^+ current (I_{K}), and a leak current (I_{L}).

$$\frac{dV}{dt} = \frac{1}{C_m} (I_{\text{Na}} + I_{\text{K}} + I_{\text{L}}) \quad (3.24)$$

The individual currents are given by:

$$I_{\text{Na}} = g_{\text{Na}_i} m_{\text{Na}_{\infty}}^3 h_{\text{Na}} (E_{\text{Na}} - V) \quad (3.25)$$

$$I_{\text{K}} = g_{\text{K}_i} m_{\text{K}}^4 (E_{\text{K}} - V) \quad (3.26)$$

$$I_{\text{L}} = g_{\text{L}_i} (E_{\text{L}} - V) \quad (3.27)$$

The activation/inactivation functions, m_{K} and h_{Na} are given by Equation 3.21. However, the activation/deactivation rates, τ_{χ} , are different to those of the neuron:

$$\tau_{\chi} = \frac{1}{\alpha_{\chi}(V) + \beta_{\chi}(V)} \quad (3.28)$$

where

$$\alpha_{h_{Na}} = 0.07 \exp(-(V + 58)/20) \quad (3.29)$$

$$\beta_{h_{Na}} = \frac{1}{1 + \exp(-0.1(V + 28))} \quad (3.30)$$

$$\alpha_{m_K} = \frac{0.01(V + 34)}{1 - \exp(-0.1(V + 34))} \quad (3.31)$$

$$\beta_{m_K} = 0.125 \exp(-(V + 44)/80) \quad (3.32)$$

3.4 Network model

An excitatory-inhibitory neural network model used in Chapter 7 to simulate gamma frequency oscillations within the CA1 region of the hippocampus. Two cell populations are used to construct this network: an excitatory pyramidal neuron population, E, composed of N_E cells and a fast-spiking (FS) inhibitory interneuron population, I, composed of N_I cells.

The network, illustrated in Figure 3.3, is based on the cortical network model by Kopell et al. [135]. Each individual cell is described by a biophysical Hodgkin-Huxley type single-compartment model (see the previous section) that is synaptically coupled to other cells within the network. Cells of the same and different neural types can be connected. Network activity is driven by external deterministic (I_{det}) and/or stochastic (I_{stoch}) currents that input to each cell. Signals then propagate across the neural network via the synaptic connections.

The equation for membrane potential of a given cell is extended to include the extra inputs:

$$C_m \frac{dV}{dt} = I_{v-gated} + I_{syn} + I_{det} + I_{stoch} \quad (3.33)$$

Network Formation

The network is connected randomly using the Erdos-Renyi model. Two factors determine the structure of the network at the cellular level: the probability that two cells in the network are connected and the strength of these connections.

The probability that two cells in the network are synaptically connected depends on the cell types and the direction of the connection (as the model considers AMPA and GABA_A receptor-mediated synapses which are both unidirectional). As such, there are independent

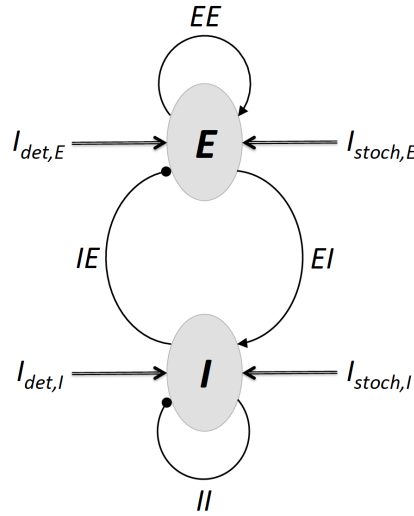


Figure 3.3 | The excitatory-inhibitory network model structure. The excitatory-inhibitory network used to simulate network activity in the CA1 region of the hippocampus. The network consists of two neuronal populations: a neuron population E and an interneuron population I that receive both stochastic and deterministic inputs. Arrow-heads indicate excitatory synaptic connections and circular-heads indicate inhibitory synaptic connections.

probabilities for neuron-neuron connectivity p_{EE} , interneuron- interneuron connectivity, p_{II} , interneuron-neuron connectivity, p_{IE} and so on. To construct the network the cells are randomly connected according to these probabilities; for example a synaptic connection between any neuron i and any interneuron j will be present with probability p_{EI} . In Kopell's original E-I network model $p_{EE} = p_{II} = p_{EI} = p_{IE} = 1$, which means that the network has all-to-all connectivity.

The strength of the connection between two cells, in terms of electrical signal propagation, is described by the synaptic conductance g . All cells from the same neural population, for example pyramidal neurons, have the same expected value for the total excitatory synaptic conductance affecting a cell, \hat{g}_{E*} , and the same expected value for the total inhibitory synaptic conductance affecting a cell, \hat{g}_{I*} . As the synaptic connections are directed, i.e. a connection from cell i to cell j is distinct from a connection from cell j to cell i , there are different expected values for the total excitatory synaptic conductance affecting an inhibitory interneuron, g_{EI} and the expected value of the total inhibitory synaptic conductance affecting an inhibitory interneuron, g_{II} . The effective synaptic conductance of, for example, the connections¹ from interneuron i to neuron j , is given by dividing the expected value of

¹One synapse in the model represents many synaptic connections

the total inhibitory synaptic conductance affecting a neuron, by the expected number of interneurons that that neuron receives synaptic input from:

$$g_{IE,ij} = \chi_{IE,ij} \frac{\hat{g}_{IE}}{p_{IE} N_I} \quad (3.34)$$

where $\hat{g}_{IE} \geq 0$, $0 < p_{IE} \leq 1$, and

$$\chi_{IE,ij} = \begin{cases} 1 & \text{with probability } p_{IE}, \\ 0 & \text{with probability } 1 - p_{IE}. \end{cases} \quad (3.35)$$

External Inputs

In addition to synaptic transmission the cells also receive external drive. The external drive to the neuron population is considered to be independent of the drive to the interneuron population. This external input is separated into two components: a deterministic current (I_{det}) and a stochastic current (I_{stoch}). The deterministic current can be used to represent periodic or predictable input from other neural regions and also to simulate experimental conditions e.g. an externally applied current pulse. The stochastic current, simulating random synaptic inputs to the cells, has the form of a Poisson spike train of mean frequency f_{stoch} , which depends on the cell type. The stochastic drive to a given cell i , for example an excitatory neuron, is given by:

$$I_{\text{stoch},E_i} = g_{\text{stoch},E} s_{\text{stoch},E_i} (V_E - V_i) \quad (3.36)$$

where the conductance $g_{\text{stoch},E}$ and the reversal potential are the same for cells of the same type. The stochastic component is incorporated in the gating variable, s_{stoch,E_i} , which jumps to 1 at each time step, δt , with a probability $\delta t f_{\text{stoch},E} / 1000$ (as the frequency is given in Hz). Each cell has an independent gating variable that decays with time constant τ_{stoch} , which depends on the cell type:

$$\frac{ds_{\text{stoch},E_i}}{dt} = s_{\text{stoch},E_i} e^{-t/\tau_{\text{stoch},E}} \quad (3.37)$$

Computational Methods

These models were simulated in MATLAB (The MathWorks, Inc.). The models were solved numerically using the midpoint method (an explicit second-order Runge-Kutta method) with a time step of $dt = 0.01$.

THE ACUTE EFFECT OF INTRACELLULAR A β ON SPONTANEOUS SYNAPTIC TRANSMISSION

Synaptic dysfunction is believed to play a major role in AD pathology [211]. A β_{1-42} oligomers (oA β) have been found to dysregulate synaptic function. Most studies have focused on prolonged extracellular oA β exposure but it is of interest to understand how oA β may alter synaptic function when it first enters a cell. A previously published study found that the intracellular infusion of oA β in CA1 neurons caused a rapid enhancement in evoked excitatory post-synaptic currents (EPSCs) [248]. In this chapter, as a follow on from this study, the immediate effect of intracellular oA β -infusion on individual synaptic events is investigated by recording spontaneous miniature EPSC (mEPSCs).

4.1 Background

4.1.1 A β and Synaptic Dysfunction

The loss of synapses, particularly in the entorhinal cortex (EC) and hippocampus, is a characteristic feature of AD [56, 95]. This degeneration begins in the early stages of the disease [159, 204, 205] and is the strongest neuropathological correlate for the severity of cognitive impairments in AD [57, 195, 231]. Given the fundamental role of synapses in memory processing and the specific impairment in memory function that clinically characterises the early stages of AD, much research has focused on the mechanisms that

underlie this synaptic degeneration.

Oligomeric A β has been found to have a wide range of dysregulatory effects, both structural and functional, at synapses in the hippocampus [50, 221]. These include the degeneration of synapses [199, 215] and the dysregulation of synaptic plasticity, specifically the enhancement of long-term depression (LTD) and the blocking of long-term potentiation (LTP), as a result of AMPAR endocytosis [108, 119, 216]

4.1.2 Acute Synaptic Effect of Intracellular oA β

The extracellular application of oA β , via perfusion or injection, is a widely employed method in studies investigating the synaptic effects of oA β [52, 141, 216, 229]. Under this protocol most effects take over an hour to manifest and are either a result of membrane-related interactions or internalisation. However, in a study by Whitcomb et al. (2015) the immediate effect of intracellularly-applied oA β on synaptic function was investigated [248]. In this work, 1-5 nM oA β was directly infused into whole-cell patched cultured CA1 neurons via the patching pipette. This concentration of oA β , the majority of which were low-n oligomers, was used to mimic the reported intraneuronal levels in AD-affected brains [101, 110]. Once the patch was obtained they recorded the EPSC evoked by periodic electrical stimulation, at 30 second intervals, of the Schaffer Collateral. They found that the direct infusion of oA β caused an immediate increase in the EPSC amplitude which began within 7 minutes of patching the cell and stabilised within 20 minutes at $181 \pm 15\%$ of the baseline (Figure 4.1a).

The increase in EPSC amplitude was specific to oligomeric forms of A β ₁₋₄₂ and was AMPAR-mediated. The blockade of calcium-permeable AMPARs (CP-AMPARs), a sub-type of AMPAR typically composed of only GluA1 subunits, reversed the increase in EPSC amplitude (Figure 4.1b). In addition, biotinylation assays found that extracellular perfusion of oA β , which also lead to an increase in EPSC amplitude (although slower - starting within 25 minutes and stabilising within 40 minutes), caused an increase in the surface expression of GluA1 but not GluA2/3. Overall, these results suggested that intracellular oA β infusion increased the amplitude of AMPAR-mediated EPSCs via the synaptic insertion of CP-AMPARs.

4.1.3 AMPA Receptors

AMPA (α -amino-3-hydroxy-5-methyl-4-isoxazolepropionic acid) receptors are ligand-gated ion channels (aka ionotropic receptors) activated by glutamate. They are expressed throughout the central nervous system (CNS) and are the most common subtype of ionotropic

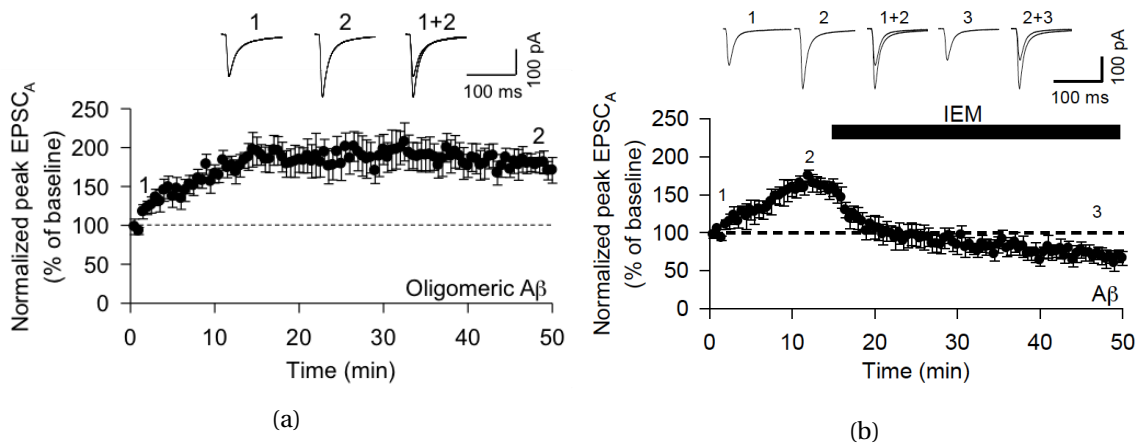


Figure 4.1 | A β infusion increases EPSC amplitude. (a) Direct infusion of A β _{1–42} into hippocampal CA1 neurons causes a rapid increase in AMPA receptor-mediated EPSC amplitude. (b) Application of the CP-AMPA inhibitor IEM prevents the increase in EPSC amplitude. Figures taken from Whitcomb et al. (2015) [248]

glutamate receptor (iGluR), which also includes NMDA (N-methyl-D-aspartate), kainate and delta receptors. AMPARs are responsible for the majority of fast excitatory synaptic transmission in the CNS [9]; in the hippocampus, blocking AMPARs silences all excitatory transmission [194]. They are also involved in several forms of synaptic plasticity [113].

AMPARs are formed of four subunits, where a subunit can be GluA1-4 [152]. The combination of these subunits determines the AMPAR's properties. In general, AMPARs have fast kinetics, opening and closing quickly in response to glutamate neurotransmitter. There are, however, differences in the properties of the different subtypes of AMPARs as a result of their particular subunit composition. For example, GluA2-lacking AMPARs are typically calcium-permeable and have a larger single channel conductance [206], faster desensitisation [234], and an inwardly rectifying current-voltage relationship [63]. Given the role of AMPARs in synaptic function and transmission, it is important to understand how A β impacts on their synaptic expression and properties.

4.1.4 Spontaneous Transmission and Miniature EPSCs

Most neurotransmitter releases at glutamatergic synapses are evoked by action potentials (AP); the arrival of an action potential depolarises the axon, activating the local voltage-gated Ca²⁺ channels, which leads to an influx of Ca²⁺ into the terminal that then triggers synaptic vesicle exocytosis [149]. In spontaneous neurotransmission, vesicle exocytosis occurs in

the absence of an AP. It is a stochastic process that occurs at all chemical synapses with an average frequency, in the hippocampus for example, of approximately 0.03 Hz per terminal [80]. Spontaneous transmission typically involves neurotransmitter release from a single, or occasionally two, vesicles [73].

Classically it was thought that spontaneous vesicle release occurred because of random conformational changes in the AP-responsive vesicle machinery but there is increasing evidence that spontaneous transmission is at least mechanistically, if not also spatially, distinct from AP-dependent release [125, 192]. It is now believed there are two distinct pools of vesicles, those that release in response to an action potential and those that spontaneously fuse with the plasma membrane via independent molecular pathways [42, 72], with further evidence that they target separate receptor populations [10, 203] and that different synapses on a single neuron can have a propensity towards spontaneous or stimulation-dependent transmission [184]. In the hippocampus, for example, around 30% of synapses tend to exhibit either spontaneous or evoked release (rather than both as in the remaining synapses) [125].

There is a growing consensus that spontaneous release has functional roles in the development and stability of synaptic connections, as opposed to just being background noise as was originally thought [125]. Studies have found that spontaneous transmission is involved in the refinement of synaptic connections during neural development and that changes in spontaneous transmission can trigger homeostatic-type synaptic responses [89, 251]. For example, reducing spontaneous transmission, either by pre-synaptically preventing or reducing the frequency of vesicle release [49, 177, 191], or by blocking post-synaptic receptors to prevent activation from spontaneous transmission, has been found to trigger AMPAR-mediated upscaling [117, 225]. It has been proposed that this synaptic scaling is a specific form of homeostatic plasticity whereby spontaneous transmission acts as a measure and regulator of synaptic efficacy [89].

Miniature EPSCs are the post-synaptic currents generated by spontaneous neurotransmission. The discovery of these apparently random miniature currents, with a distinctive shape and relatively consistent amplitude, occurred fairly early on in the development of cellular recordings [69]. They contributed to the discovery that synaptic transmission is a quantal process, where each vesicle holds an individual packet or 'quantum' of neurotransmitter [58]. As mEPSCs are generated by the neurotransmitter release from a single vesicle they have proven to be an essential analytical tool for probing synaptic properties

and mechanisms [83, 155].

A typical mEPSC profile is shown in the inset of Figure 4.2. The profile is affected by both pre and post-synaptic properties. Important variables that influence the shape of the mEPSC include: the vesicular glutamate content; the neurotransmitter clearance rates within the cleft; the vesicle release site position relative to the post-synaptic active zone; the distribution of receptors and the type of receptors (and their respective properties e.g. conductance and binding, unbinding rates and desensitisation rates) [71, 254].

Miniature EPSC recordings are a commonly used experimental paradigm in synapse studies. They are typically recorded in the presence of tetrodotoxin (TTX), which blocks Na⁺ channels and thereby prevents any spontaneous AP generation [124, 174]. As mEPSCs reflect transmission at single synapses, recordings of mEPSCs are often carried out in conjunction with other electrophysiology measurements that capture collective synaptic transmission, such as evoked EPSC recordings. By analysing the properties of the recorded mEPSCs, these experiments can both corroborate findings of altered synaptic transmission, from LTP or LTD for example, and provide further insight into the underlying synaptic changes [83, 155].

The features typically analysed in mEPSC experiments are the frequency and the amplitude of the mEPSC [1, 5, 118, 123, 155, 156]. A change in the mEPSC amplitude is traditionally taken to reflect a change at the post-synapse, such as a change in the receptor profile [149]. However, mEPSC amplitude can also be determined by pre-synaptic properties such as vesicle glutamate concentration and multi-vesicular release. Miniature EPSC frequency is usually taken to reflect pre-synaptic changes as it is governed by the rate of vesicle release at the pre-synapse (although it could also be related to receptor desensitisation rates) [83, 149].

Although the recent developments in our understanding of the segregation between spontaneous and evoked synaptic transmission mechanisms (discussed above) could suggest that mEPSCs are not necessarily indicative of synaptic changes observed in evoked-response experiments, the large number of studies over the years that have used these experiments in combination and shown corroborative data indicates that is likely that mEPSCs do reflect 'general' synaptic changes. Therefore, the traditional use of mEPSC recordings still provides a useful measure of synaptic transmission and potentially, given recent insight, has more interesting information to divulge/has more functional implications than previously thought.



Figure 4.2 | Example mEPSC recording. An extract of a current trace recorded from a pyramidal neuron in patch clamp. Inset shows a magnified mEPSC. The mEPSC profile is typical of an AMPAR-mediated mEPSC.

4.2 Experimental Methods

Electrophysiological techniques were used to record AMPAR-mediated mEPSCs in A β -treated and control CA1 neurons in organotypic cultured hippocampal slices. In this section the methods used to obtain the mEPSC data are described in detail. To summarise, the key steps are as follows:

1. Cultured hippocampal slices were placed in the recording chamber of an electrophysiology rig and continuously perfused with artificial cerebrospinal fluid (ACSF).
2. CA1 neurons in the slices were whole-cell patched and voltage clamped at -70mV.
3. Oligomerised A β_{1-42} (1 - 5 nM) was directly infused into the neurons via the filling solution of the patching pipette (in the control experiments a Cs-based only filling solution was used).
4. The AMPAR-mediated current was pharmacologically-isolated via the ACSF.
5. The whole-cell current was recorded continuously for 6 minutes, starting 10 minutes after patching.
6. The current data was analysed offline to identify the mEPSCs and measure their properties (amplitude, half-width, rise and decay times).

4.2.1 Hippocampal Slice Preparation

Organotypic slice cultures were prepared by colleagues in the lab from 7 day old Wistar rats according to a previously established method (as described in [248]). The slices were

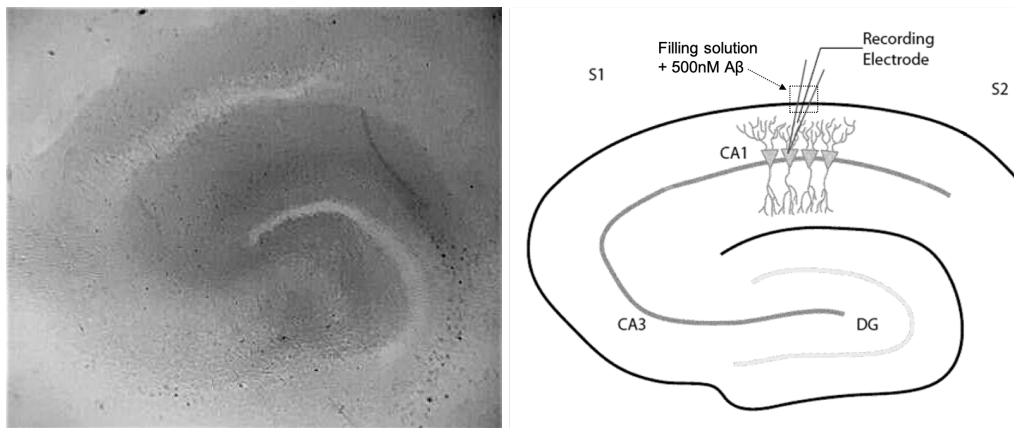


Figure 4.3 | A typical cultured hippocampal slice. Miniature EPSCs were recorded from whole-cell patched CA1 neurons in cultured hippocampal slices. (a) A bright field image of the cultured hippocampal slice as viewed through the microscope's 4x objective. (b) A simple schematic of the hippocampus showing the recording electrode placement when whole-cell patching CA1 pyramidal neurons. The neurons were A β -treated by adding 500nM A β solution to the microelectrode filling solution.

cultured *in vitro* in an incubator at 35°C in a 5% CO₂ enriched atmosphere for 6 - 8 days before use. A bright-field photo of a typical cultured hippocampal slice as used in the experiments is shown in Figure 4.3a.

4.2.2 Amyloid- β_{1-42} Preparation

Synthetic A β_{1-42} solution was prepared from amyloid- β 1-42 peptide (Millipore, UK) using a previously described method (see [248]). Prior to use, the solution was diluted to the required concentration using Dulbecco's Phosphate-Buffered Saline (DPBS) and then incubated for 2 hours at room temperature to allow for oligomerisation. This protocol produces a heterogeneous amyloid- β solution containing 1 - 5 nM amyloid- β oligomers, of which a high percentage (60%) are low-n oligomers [248]; Figure 4.4 shows the oligomeric size distribution in the working A β solution (from [248]). The biological activity of the A β solution was confirmed by verifying that LTP was inhibited in acute hippocampal slices pre-treated for 2 hours with 500nM A β_{1-42} solution (an established synaptic effect of A β [216, 241]).

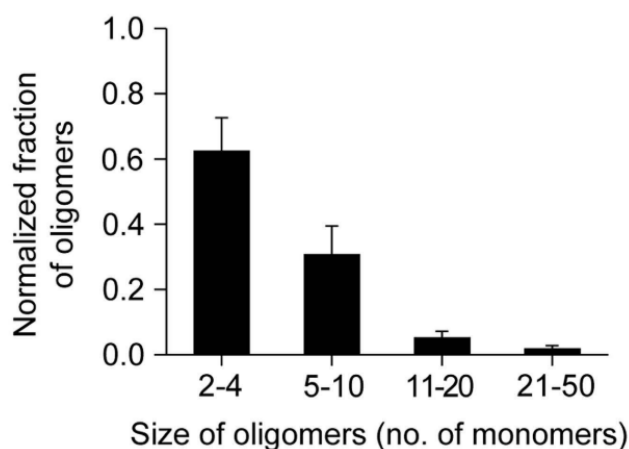


Figure 4.4 | A β oligomer size distribution in working solution. Histogram from Whitcomb et al. (2015) showing the size distribution of the amyloid- β oligomers in the prepared working A β solution. Over 60% are low n-number oligomers composed of 2 - 4 monomers [248].

4.2.3 Electrophysiology Equipment

A standard electrophysiology rig was used to record the mEPSCs. A schematic of the electrophysiology rig used is given in Figure 4.5. The key components of the rig that are referred to in the text are labelled in the figure. Photos of the actual rig used in the experiments are shown in Figure 4.6.

The cultured slices were placed on a glass coverslip in an open diamond bath recording chamber and held in place using an in-house constructed nylon mesh. The recording chamber was secured to the xy stage of an Olympus BX51 WI microscope. The slices were visualised using a Hitachi KP-M1AP camera which was attached to the microscope and connected to a 12-inch PC monitor.

To keep the slices in good condition the recording chamber was continuously perfused (at a rate of 2 ~ 3 ml/min) with ACSF containing (in mM): NaCl, 119; KCl, 2.5; CaCl₂, 4; MgCl₂, 4; NaHCO₃, 26; NaH₂PO₄, 1; glucose, 11; 2-chloroadenosine, 0.01 [131]. To isolate AMPAR mediated mEPSCs three antagonists were added to the ACSF: 50 μ M D-AP5, an NMDAR antagonist [176]; 20 μ M bicuculline, a GABA_AR antagonist; 500nM TTX, a Na⁺ channel inhibitor [216]. The ACSF stock was preheated in a waterbath to approximately 35°C and was continuously perfused with 5 % CO₂ / 95 % O₂. The ACSF was pumped to the recording chamber via a fine bore polyethylene tube connected to a peristaltic pump. Immediately before entering the recording chamber the ACSF was reheated via a heated

perfusion tube to ensure the recording chamber temperature was maintained at 28 - 30°C. The excess ACSF was continuously removed from the recording chamber via suction by using a syringe needle attached to a vacuum pump.

The mEPSCs were recorded using glass pipette microelectrodes. The pipettes were made from borosilicate glass capillaries using a Brown-Flaming horizontal electrode puller, which produced glass pipettes with a tip resistance of 4 - 6M Ω . The pipettes were filled with Cs-methane sulfonate filling solution (Cs filling solution) for the control experiments, and with Cs filling solution with an additional 500nM A β -solution for the A β -treated experiments. The Cs filling solution (pH 7.2) contained (in mM): CsMeSO₄, 130; NaCl, 8; Mg-ATP, 4; Na-GTP, 0.3; EGTA, 0.5; HEPES 10 and QX-314, 6 [248]. The microelectrode was threaded over a chloride-coated silver wire (\varnothing 0.2mm) connected to the headstage of a MultiClamp 700B Microelectrode amplifier. The wire length was set so that it was in contact with the filling solution but did not reach the tip of the glass pipette. The microelectrode was secured to an electrode holder attached to an xyz-micromanipulator to enable precise positioning of the microelectrode. A second chloride-coated silver wire was placed in the recording chamber to provide a ground reference. The electrode equipment was fixed to a Scientifica SlicePlatform. The SlicePlatform, microscope and camera were attached to a Newport air table within an in-house constructed Faraday cage to reduce external noise.

4.2.4 Whole-cell Patch Protocol

The CA1 neurons were whole-cell patched and voltage clamped at -70mV according to the following standard protocol [94]. The recording electrode and camera were positioned above the bath recording chamber over the CA1 region of the slice (see Figure 4.3a as an example of the hippocampal slice viewed through the microscope). Throughout the experiment the electrode tip resistance was continuously monitored by measuring the current generated across the tip by 1 mV - 100 ms pulses. Before submerging the electrode a small positive pressure was applied pneumatically to prevent debris entering the pipette. The microelectrode was then slowly lowered into the CA1 cell layer until the pipette was directly above the surface of the target cell (the schematic in Figure 4.3b demonstrates the electrode positioning). The positive pressure was then removed so that the pipette tip came into contact with the cell membrane, causing an increase in the pipette tip resistance. The membrane patch was then achieved by applying a short sharp burst of negative pressure. A patch attempt was deemed to be successful if the seal resistance was greater than 1 G Ω . At this point, a holding potential of -30mV was applied via the microelectrode and

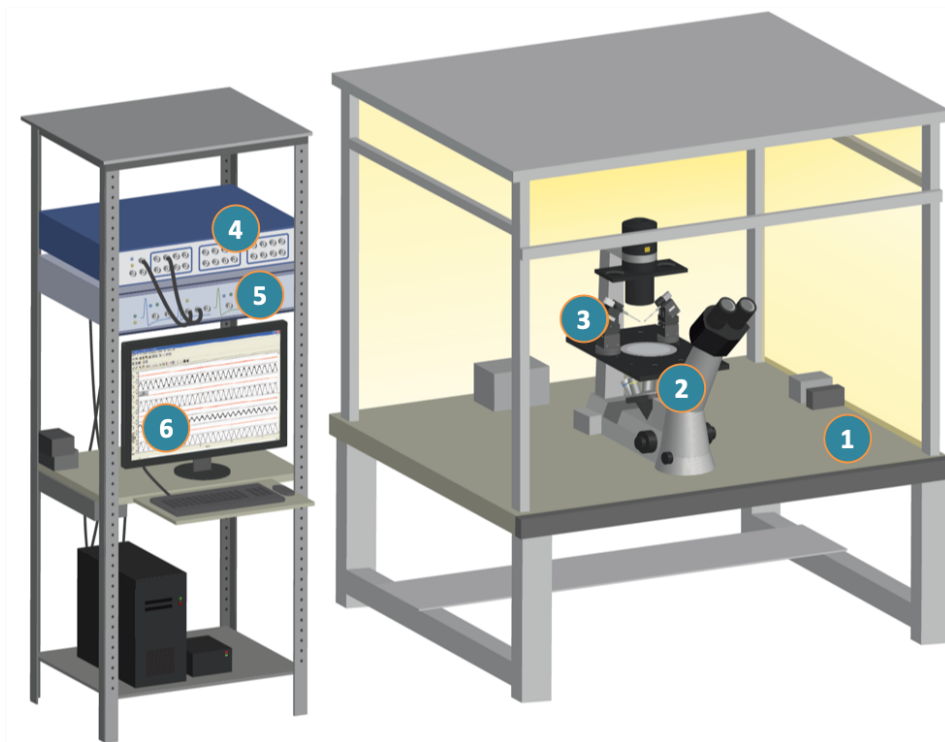


Figure 4.5 | Electrophysiology rig infographic. An electrophysiology rig with key components highlighted (figure adapted from [165]). ① The electrophysiology rig was attached to a Newport air table within an in-house constructed Faraday cage to reduce external noise ② The slice was placed in a diamond recording bath attached to the xy stage of an Olympus BX51 WI microscope. ③ Electrode holders connected to xyz manipulators were used to position the recording microelectrode. ④ A Multi-Clamp 700B Microelectrode amplifier and integrated headstage was used to record the electrical signals within the slice. ⑤ A digitiser converted the recordings into a digital signal. ⑥ The direct current, series resistance and input resistance were continuously monitored and analyzed online using WinLTP software

then gradually decreased to -70mV . As an indicator of cell health and viability, the resting membrane potential (RMP) was measured before starting the recording; only cells with a RMP between -50mV and -70mV were used.

4.2.5 Miniature EPSC Recording Protocol

Whole-cell current recordings began 10 minutes after successfully achieving a whole-cell patch to allow time for the diffusion of the electrode filling solution into the cell. As mentioned previously (Section 4.2.3), the control experiments used a Cs-methane sulfonate microelectrode filling solution only, whereas for the A β experiments 500nM A β solution was

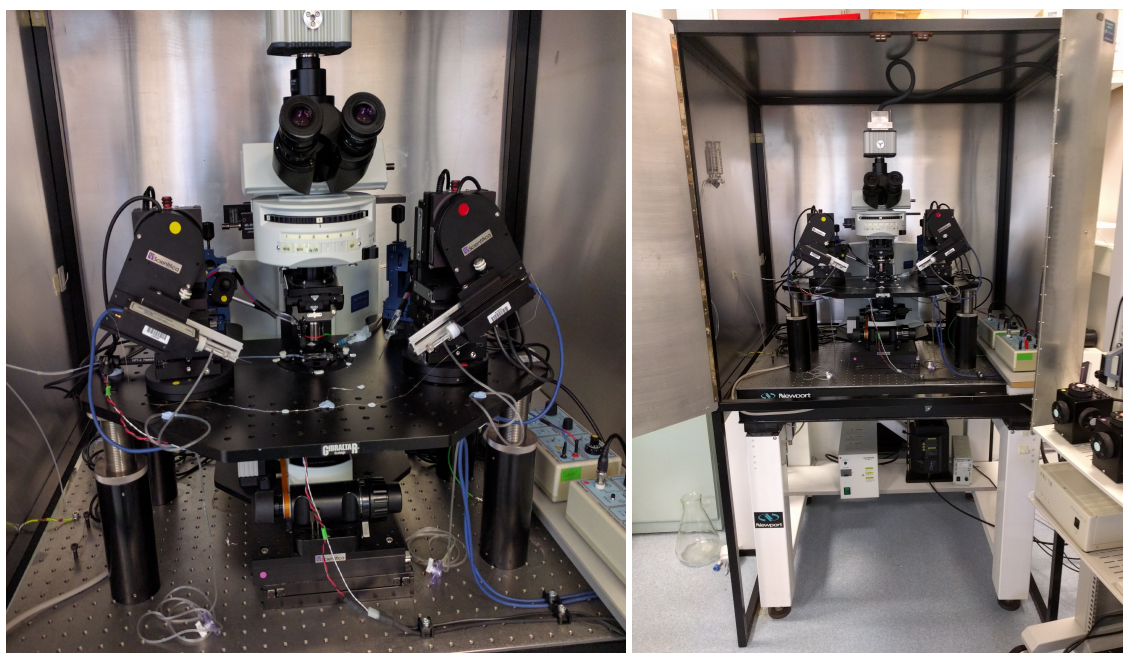


Figure 4.6 | Photos of the electrophysiology rig. The rig used for the patch-clamp recordings. The microscope, slice platform and electrode holders (left panel) were housed within a Faraday cage on a noise-damping Newport air table (right panel).

added to the Cs-based solution. For each hippocampal slice, recordings from both control and $A\beta$ -treated cells were carried out. The whole-cell current was recorded continuously for 6 minutes. Throughout each experiment the series resistance, R_S (which is synonymous with the electrode resistance), and the membrane resistance, R_M was measured to monitor the cell's condition. Only recordings from cells that maintained a series resistance below 20 MW which varied less than 10% from the baseline were used (see Figure A.1 in the Appendix for the recorded R_S).

4.2.6 Data Acquisition and Analysis

The direct current, series resistance and input resistance were continuously monitored using the WinLTP software. The data was low-pass filtered at 2 kHz and sampled at 20kHz.

The mEPSC data was analysed offline using MiniAnalysis 6.0.3 (Synsoft) [226]. Each current trace (refer back to Figure 4.2 for an example trace segment) was scanned by MiniAnalysis for spontaneous events with a minimum amplitude threshold of 6pA (approximately three times the baseline noise) and minimum area threshold of 10 fC. Each event detected was visually inspected to eliminate false events. Events that did not display the typical

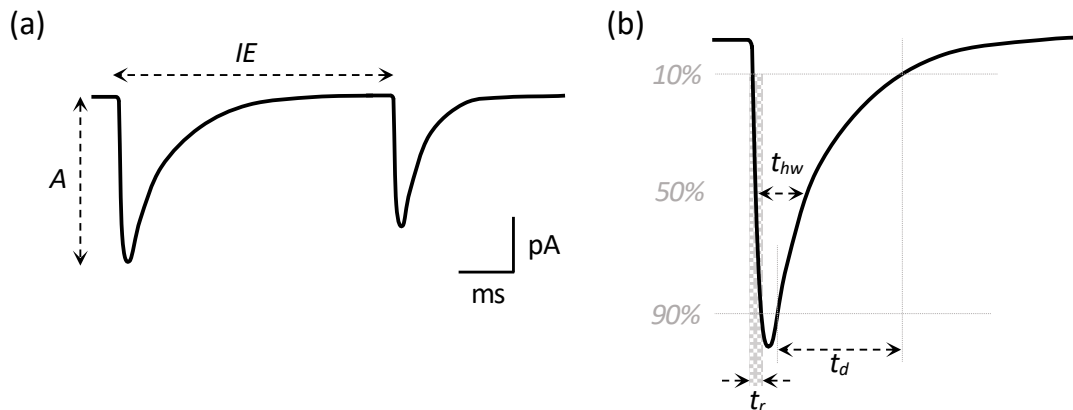


Figure 4.7 | Miniature EPSC measures. Representative mEPSCs showing the properties extracted from the mEPSC recordings. (a) A current trace with two mEPSC events showing the amplitude (A) and inter-event interval (IE) measures. (b) A single mEPSC labelled with the 10-90% rise time (t_r), 90-10% decay time (t_d) and half-width at 50% of the amplitude (t_{hw}).

characteristics of a mEPSC, namely a fast rise time relative to the decay time and an approximately exponential decay [236], were rejected. Events were also rejected when their duration exceeded 50 ms. The majority of false events were easily identifiable and were typically related to fluctuations in the baseline current or noise; false events accounted for less than $\sim 5\%$ of the events detected. Finally, events that overlapped were removed from the data set to ensure that only single-event parameters were analysed, these overlapping events accounted for less than $\sim 1\%$ of the events detected.

For each confirmed mEPSC, the amplitude (A), rise time (t_r), decay time (t_d), half-width (t_{hw}) and time of the event were extracted by MiniAnalysis. The rise time was defined as the time taken for the current to increase from 10% to 90% of the maximum amplitude, the decay time was the time taken for the current to drop from 90% to 10% of the maximum amplitude and half width was the width of the mEPSC at 50% of the maximum amplitude. The inter-event interval (IE), the time between events, was calculated by taking the time difference between consecutive events. These properties are labelled on the stylised current traces shown in Figure 4.7. The IE was used to calculate the instantaneous frequency (IF) for each mEPSC, where $IF = 1 / IE$.

Statistical comparisons were carried out using non-parametric tests as the data was non-normally distributed. The tests used are the Wilcoxon rank-sum test (wrs) and the Kolmogorov-Smirnov (ks) test to compare distributions. Correlation analysis was carried out using Spearman's rank correlation (r_s) coefficient. Descriptive statistics are reported

as median \pm C.I. where the confidence interval (C.I.) is calculated as: $\pm 1.58 * IQR / \sqrt{n}$ which gives an approximately 95% confidence that the medians are different (*IQR* is the interquartile range). Tukey box plots show: the median (centre line), the 95% C.I. (notches), the interquartile range (*IQR*, boxed area), the range of the data that falls within $\pm 1.5 * IQR$ (whiskers) and the outliers (dots). All box plots were generated using the BoxPlotR web tool [222]. In the figures *p*-values are indicated using the following labels: **p* < 0.05, ***p* < 0.01, ****p* < 0.001.

4.3 Results

In total, recordings from 12 untreated (Control) and 11 A β -treated (A β) CA1 pyramidal neurons were analysed. Each recording consisted of 6 minutes of continuous current data sampled at 20kHz and filtered at 2kHz. Figure 4.8a shows representative recordings of the basal current from an A β -treated neuron and from a Control neuron. In total 1209 and 1263 mEPSCs were identified in A β -treated and Control cells respectively. The mEPSC frequency, amplitude and kinetic properties (rise time, decay time and halfwidth) were measured and the results from the A β and control cells were compared.

4.3.1 mEPSC Amplitude & Frequency Analysis

There was a statistically significant increase in the amplitudes of the AMPAR-mediated mEPSCs following direct A β_{1-42} infusion compared to the Control group (Figure 4.8b). The median mEPSC amplitude increased from 13.6 ± 0.58 pA in the Control group to 14.9 ± 0.71 pA in the A β -treated group, which is an increase of approximately 10% (Figure 4.8b:Left *p* < 0.001, Wilcoxon rank-sum test). There was also a significant difference between the cumulative frequency distribution of the mEPSC amplitudes in the control group compared to the A β -treated group (Figure 4.8b:Right *p* < 0.001, Kolmogorov-Smirnov test).

No statistical difference was found between the instantaneous frequency of the mEPSCs in the control group and the A β -treated group (Figure 4.8c). The median instantaneous frequencies were 0.52 ± 0.06 Hz and 0.53 ± 0.06 Hz for the Control group and the A β -treated group respectively (Figure 4.8c:Left *p* = 0.70, Wilcoxon rank-sum test). No difference was measured between the cumulative frequency distribution of the instantaneous mEPSC frequency for the control group compared to the A β -treated group (Figure 4.8c:Right *p* = 0.26 Kolmogorov-Smirnov test).

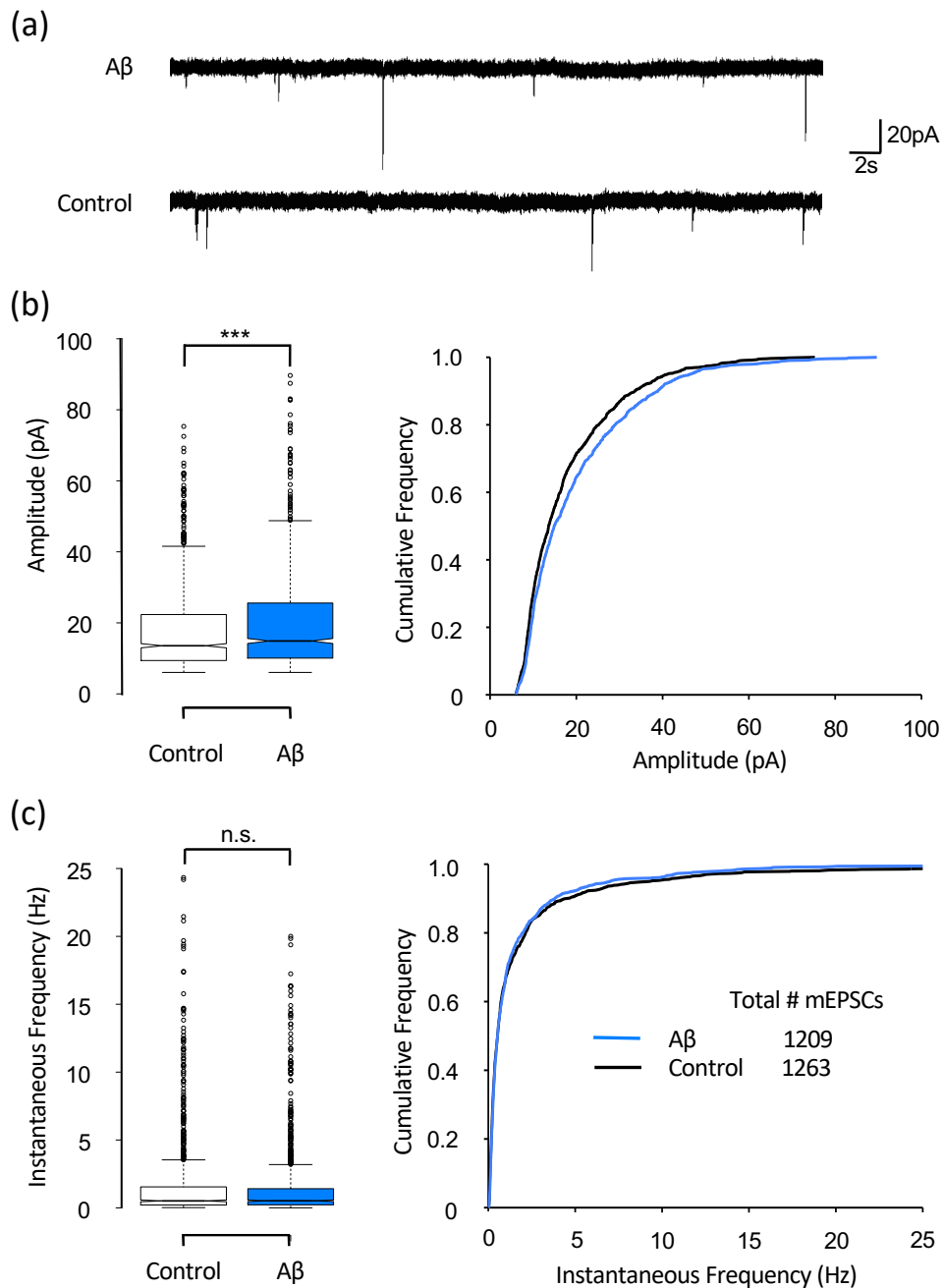


Figure 4.8 | Recorded mEPSC amplitude and frequency distributions. Analysis of the amplitudes and instantaneous frequencies of the mEPSCs recorded from A β -treated and un-treated (control) CA1 pyramidal neurons (A β : $n = 11$, # mEPSCs = 1209; Control: $n = 12$, # mEPSCs = 1263). (a) Representative basal current recordings from A β -treated and control cells. (b) A β -treatment significantly increased the mEPSC amplitudes; the median amplitude of the mEPSCs increased from 13.6 ± 0.58 pA (control) to 14.9 ± 0.71 pA in A β -treated cells (box plot, $p_{WTS} < 0.001$) and the distribution of the recorded amplitudes shifted towards larger amplitudes (CDF plot, $p_{ks} < 0.001$). (c) There was no significant difference in the instantaneous frequencies of the mEPSCs recorded from the control and the A β -treated cells ($p_{WTS} = 0.70$, $p_{ks} = 0.26$).

4.3.2 mEPSC Kinetics Analysis

The two statistical tests used to analyse the data produced different results (Figure 4.9a). The Wilcoxon rank-sum test, which tests whether one data set is significantly larger than the other, found no statistical difference in the median of the rise time of the AMPAR-mediated mEPSCs following direct $A\beta_{1-42}$ infusion compared to the Control group. The median rise times were 2.56 ± 0.09 ms and 2.74 ± 0.11 ms for the Control group and the $A\beta$ -treated group respectively (Figure 4.9a:Left $p = 0.17$). However, the Kolmogorov-Smirnov test, which assesses the difference in the distributions, showed a significant difference between the distribution of the mEPSC rise times in the Control group compared to the $A\beta$ -treated group (Figure 4.9a:Right $p < 0.01$).

No statistical difference was found between the mEPSC decay times of the control group and the $A\beta$ -treated group (Figure 4.9b). The median decay times were 7.20 ± 0.18 ms and 7.25 ± 0.21 ms for the Control group and the $A\beta$ -treated group respectively (Figure 4.9b:Left $p = 0.95$, Wilcoxon rank-sum test). No difference was measured between the distribution of the mEPSC decay times for the Control group compared to the $A\beta$ -treated group (Figure 4.9b:Right $p = 0.22$, Kolmogorov-Smirnov test).

There was no statistical difference between the mEPSC half-widths of the the control group and the $A\beta$ -treated group (Figure 4.9c). The median half-widths were 7.82 ± 0.22 ms and 7.83 ± 0.26 ms for the Control group and the $A\beta$ -treated group respectively (Figure 4.9c:Left $p = 0.26$, Wilcoxon rank-sum test). No difference was measured between the distribution of the mEPSC half-widths for the Control group compared to the $A\beta$ -treated group (Figure 4.9c:Right $p = 0.06$, Kolmogorov-Smirnov test).

4.4 Discussion

It was found that direct intracellular infusion of $A\beta$ oligomers into CA1 pyramidal neurons caused an increase in the amplitude of AMPAR-mediated mEPSCs. This increase in mEPSC amplitude occurred rapidly after $A\beta$ infusion; the amplitude was enhanced by the time recording started 10 minutes after the whole-cell patch was obtained. There was no significant difference in the frequency of the mEPSC events following $A\beta$ -treatment. Analysis of the mEPSC kinetics identified no change in the mEPSC decay times or half-width. There was no significant difference found in the duration of the rise times of the $A\beta$ -treated and Control data but the distribution of those rise times was found to be significantly different.

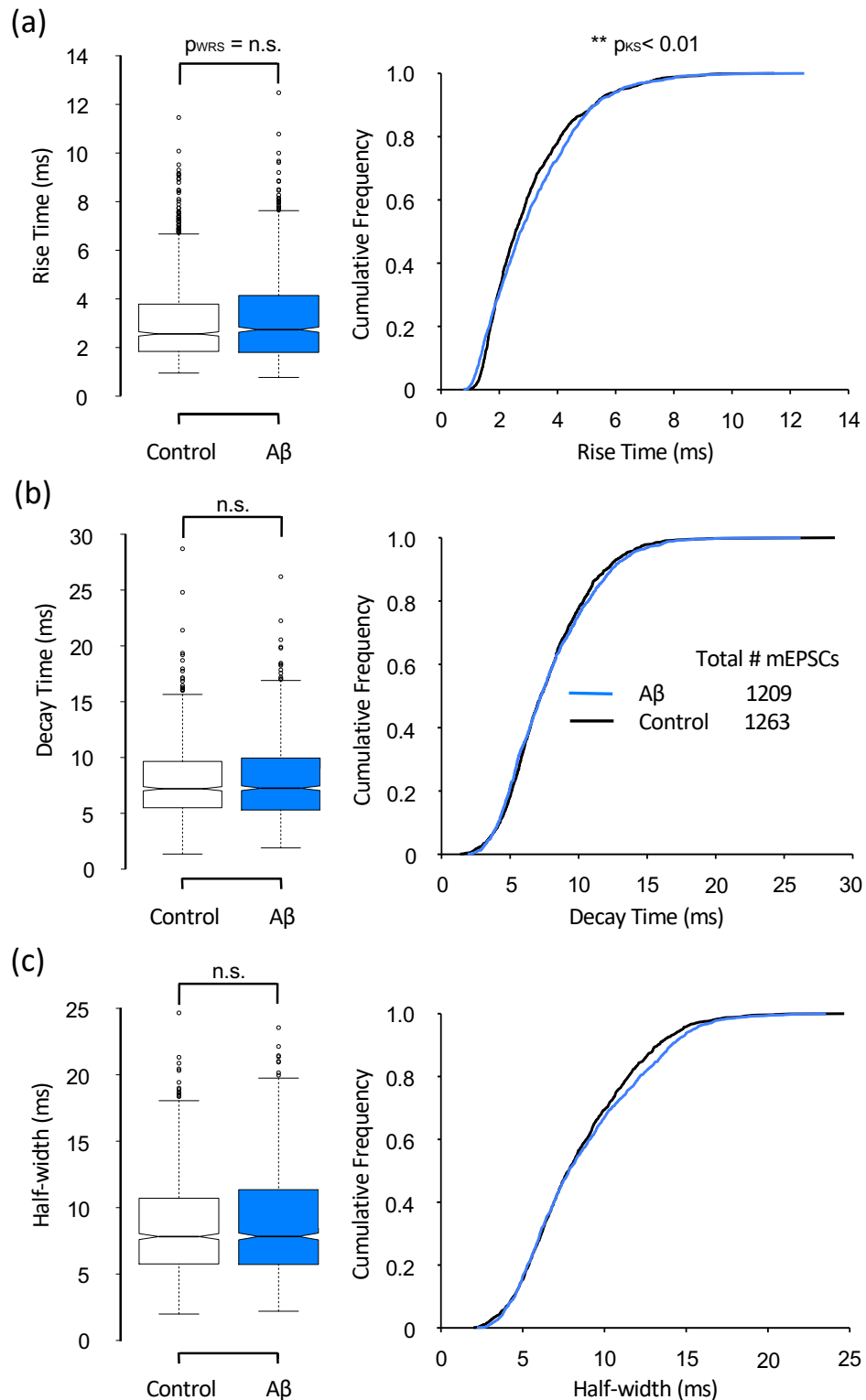


Figure 4.9 | Recorded mEPSC kinetics. Analysis of the mEPSC kinetics from A β -treated and un-treated (control) CA1 pyramidal neurons (A β : $n = 11$, # mEPSCs = 1209; Control: $n = 12$, # mEPSCs = 1263). (a) There was no significant change in the median mEPSC rise times (box plot, Control: 2.56 ± 0.09 ms, A β : 2.74 ± 0.11 , $p_{\text{WRS}} = 0.17$) but there was a significant difference in the rise time distribution (CDF plot, $p_{\text{KS}} < 0.01$).

Figure 4.9 (continued) (b) There was no significant change in the mEPSC decay times in the A β -treated cells ($p_{\text{wrs}} = 0.95$, $p_{\text{ks}} = 0.22$). (c) There was no significant change in the mEPSC half-widths in the A β -treated cells ($p_{\text{wrs}} = 0.26$, $p_{\text{ks}} = 0.06$).

Changes in mEPSC amplitude are traditionally taken to reflect post-synaptic alterations, although it can reflect changes in pre-synaptic vesicle content [83, 149]. In this case, given that there was no observable difference in the mEPSC frequency, which is typically associated with pre-synaptic release properties, and considering the timescale of the experiments it is unlikely that A β has altered the neurotransmitter concentration at the pre-synapse. It is therefore reasonable to hypothesise that the acute A β treatment caused an increase in the amplitude of AMPA-mediated mEPSCs by altering the post-synaptic AMPA receptor profile of individual synapses. This supports the claim of the study discussed in Section 4.1.2 that acute A β -treatment enhances AMPAR-mediated EPSCs via the insertion of CP-AMPARs at the post-synapse [248].

Given that kinetic observations and amplitude changes have a complicated interaction with post-synaptic properties, without further research it is not possible to determine exactly how the AMPA receptor profile has changed when considering the increase in AMPAR receptor in conjunction with the absence of any kinetic changes. Further studies would be need to be carried out to determine the changes underlying the increase in synaptic transmission and to determine conclusively if there is a shift in the mEPSC rise times and if this result is CP-AMPAR mediated. It is worth noting that these findings are recorded from cultured hippocampal slices from young mice. CP-AMPAR expression is significantly reduced in adult synapses therefore it is important that this experiment is repeated in older mice to determine if this is a consistent mechanism.

MODELLING THE EFFECT OF ACUTE $A\beta$ ON SYNAPTIC TRANSMISSION

Amyloid- β has been found to dysregulate both synaptic function and structure [50, 138, 216, 240]. Models can be used to investigate the functional consequences of this $A\beta$ -mediated synaptic dysfunction [53, 198]. In the previous chapter it was shown that the intracellular infusion of $A\beta$ causes a rapid increase in the amplitude of spontaneous mEPSCs. In this chapter the experimental data is used to develop a minimal biophysical model of synaptic transmission that simulates the mEPSC waveform and accounts for the distribution in mEPSC amplitudes recorded in the untreated control cells by using a lognormal distribution of transmitter concentration. Using this model it is shown that the same underlying distribution can account for the recorded effect of $A\beta$, purely by altering the conductance of the synapse.

5.1 The mEPSC Model

5.1.1 Method Overview

A first-order kinetic model of an excitatory synapse was used to simulate AMPAR-mediated mEPSCs. The model was parameterised using the mEPSC waveforms that were recorded in the experiments described in the previous chapter. First, the model was fit to the individual control mEPSCs to generate parameter distributions and to investigate their correlation

with the recorded mEPSC amplitudes. This work was used to identify which parameter distributions were required to describe the mEPSC amplitude distribution and to inform the parameter values used in the control model. Through this method a lognormal distribution of neurotransmitter concentration was obtained. Drawing the neurotransmitter concentration from this distribution, whilst keeping the other parameters fixed at values obtained through the fitting, generated mEPSCs that fit well to the amplitude distribution of the Control data. Subsequently, Monte Carlo simulations were run to investigate if the experimentally observed increase in mEPSC amplitude in the A β -treated neurons could be accounted for using the Control model but with only altering the synaptic conductances.

5.1.2 Model Set-up

As discussed in Section 4.1.4, a mEPSC is generated by spontaneous quantal transmission (i.e. the signal generated at a single synapse by a single vesicle release). In the experiments, AMPAR-mediated mEPSCs were isolated pharmacologically, by applying ion-channel and receptor blockers, and by voltage-clamping the cell at -70mV to prevent NMDAR activation and to keep the current contribution from other voltage-gated ion channels constant. Therefore, the recorded mEPSCs could be represented (assuming perfect clamping and channel blocking) by a model of synaptic transmission that only considered currents from a fast-activating ligand-gated receptor population. A simple first-order kinetic model of synaptic transmission was chosen to simulate the mEPSCs as the signal-to-noise ratio present in the recordings and the fact that they were recorded at the soma through whole-cell patch clamp meant the resolution was not suitable for a more detailed model.

The general form of the synapse model used to describe the mEPSC behaviour is given in Section 3.2. To simulate AMPAR-mediated mEPSCs, the five parameters used to describe synaptic transmission in the model are interpreted as: the total conductance of the AMPAR population at that synapse (g); the activation rate of the AMPARs (α); the deactivation rate of the AMPARs (β); the concentration of the neurotransmitter (C_T); the duration of neurotransmitter exposure (t_{pulse}). As the reversal potential of an AMPAR is 0 mV and the cell is voltage-clamped at V_{clamp} , Eqn. 3.8 becomes:

$$I_{\text{mEPSC}} = -gV_{\text{clamp}}r(t) \quad (5.1)$$

where r is the fraction of open receptors, which can be written as:

$$\frac{dr}{dt} = \alpha(1-r) - \beta r \quad (5.2)$$

with

$$\gamma = \begin{cases} \alpha C_T & \text{if } 0 < t < t_{\text{pulse}} \\ 0 & \text{otherwise} \end{cases} \quad (5.3)$$

Given that g (the maximal synaptic conductance) is also constant, this means that the waveform of the mEPSC is determined by the fraction of open receptors. An example of a mEPSC-type trace generated by the model and the behaviour of $r(t)$ is shown in Figure 5.1.

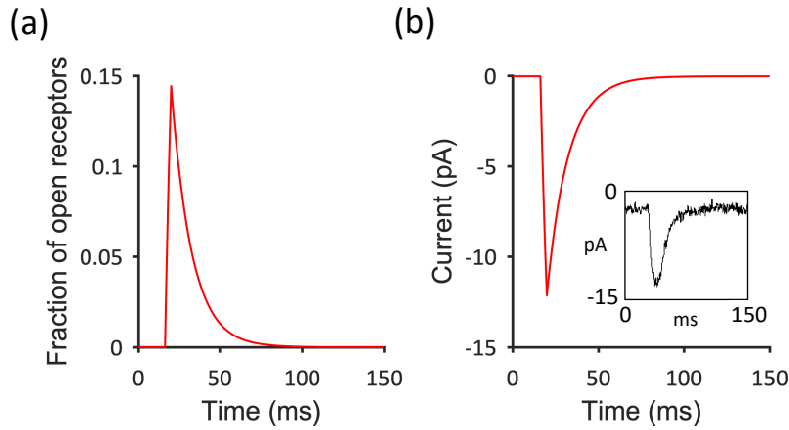


Figure 5.1 | Example mEPSC simulations. Example simulated mEPSC-type trace generated by a 1ms pulse of neurotransmitter. (a) The fraction of open receptors (r) as a function of time. (b) The simulated mEPSC (I_{rec}). Inset shows a recorded mEPSC for shape comparison.

The sketch in Figure 5.2 outlines how the model parameters define the dynamics of the receptor opening and, by extension, the simulated mEPSC. The exponential rise and decay phase can be considered separately, where the rise time and decay time constants, τ_r and τ_d respectively, are given by [61]:

$$\tau_r = \frac{1}{\gamma + \beta} \quad , \quad \tau_d = \frac{1}{\beta} \quad (5.4)$$

The fraction of open receptors, r_{max} , can be derived from Equation 5.2 as:

$$r_{\text{max}} = r_{\infty} \left(1 - \exp\left(-\frac{t_{\text{pulse}}}{\tau_r}\right) \right) = \frac{\gamma}{\gamma + \beta} \left(1 - \exp\left(-(\gamma + \beta)t_{\text{pulse}}\right) \right) \quad (5.5)$$

where r_{∞} is the fraction of open receptors at infinite time. Therefore, the mEPSC amplitude, I_{max} , is given by:

$$I_{\text{max}} = r_{\text{max}} \cdot g V_{\text{clamp}} \quad (5.6)$$

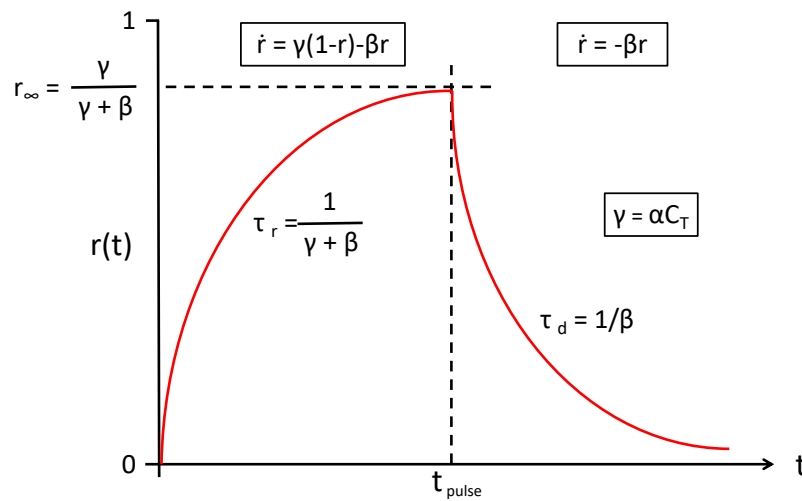


Figure 5.2 | mEPSC model: fraction of open receptors profile. Sketch illustrating the properties that determine the time-course of the fraction of open receptors, $r(t)$, and by extension in voltage-clamp the mEPSC time-course. γ : product of C_T (transmitter concentration) and α (binding rate), τ_r : rise time constant, τ_d : decay time constant, β : unbinding rate, t_{pulse} : transmitter release duration, r_∞ : maximum number of open receptors at infinite time.

and depends on t_{pulse} and the ratio of $\gamma:\beta$, where an increase in β decreases the maximum decreases. As the numbers of receptor activated following the release of a single vesicle occurs well below saturation levels ($< 50\%$ of the total available AMPARs [115, 151]) this requires $r_\infty < 0.5$ or $t_{\text{pulse}} \lesssim 0.7\tau_r$ or a combination of these constraints.

5.1.3 Parameter Sensitivity Analysis

To illustrate how the model parameters affect the shape of the simulated mEPSC when situated within an approximately biological range, the results from one-at-a-time (OAT) sensitivity analysis are shown in Figure 5.3. Using this method the impact of each parameter is assessed by measuring the amplitude, rise time and decay time of the simulated mEPSCs when the parameters are varied one-at-a-time. Note that the half-width, which was measured in the experimental chapter, is not discussed as it is closely correlated with the decay time. As a point of reference, the best-fit parameter values obtained by fitting the simulated trace to an average recorded control mEPSC (method described in Section 5.2.1) are marked on the plots.

The amplitude of the simulated mEPSC is governed by g (Fig. 5.3a) and, as expected

from Equation 5.5, on γ , β and t_{pulse} (Fig. 5.3d, g and j). The rise time, which is governed by τ_r (Eqn. 5.4), depends on γ , β and t_{pulse} (Figures 5.3e, h and k). The mEPSC decay time is governed by the decay time constant τ_d (Eqn. 5.4), which is determined by the unbinding rate β (Fig. 5.3i).

5.2 Model Fitting

5.2.1 Simulating mEPSC Amplitude Variability

In the first stage of the mEPSC model development, the model was fit to each individual mEPSC using multivariate gradient descent with two free variables, γ and β (an overview of this standard fitting method is given in Appendix B). The other two synaptic properties in the model, the total conductance, g , and neurotransmitter pulse duration, t_{pulse} , were defined prior to fitting; g was fixed at 0.8 nS [33, 161] and t_{pulse} was measured as the time from start to peak of the recorded mEPSC. Examples of the fits obtained are shown in Figure 5.4.

The inherent variability of the recorded mEPSCs resulted in variations in the fitted parameter values, γ and β , and also in the measured t_{pulse} . The parameter distributions are shown in Figure 5.5, the median values of γ , β and t_{pulse} were 0.04 ms^{-1} , 0.08 ms^{-1} and 3.9 ms respectively. To identify which continuous distribution best approximated the parameter distributions, the fit of four probability density functions (normal, lognormal, gamma and Weibull) were compared to the empirical parameter distributions. The skewed distributions of all three parameters were best fit with lognormal distributions (shown in Figures 5.5a, c and e).

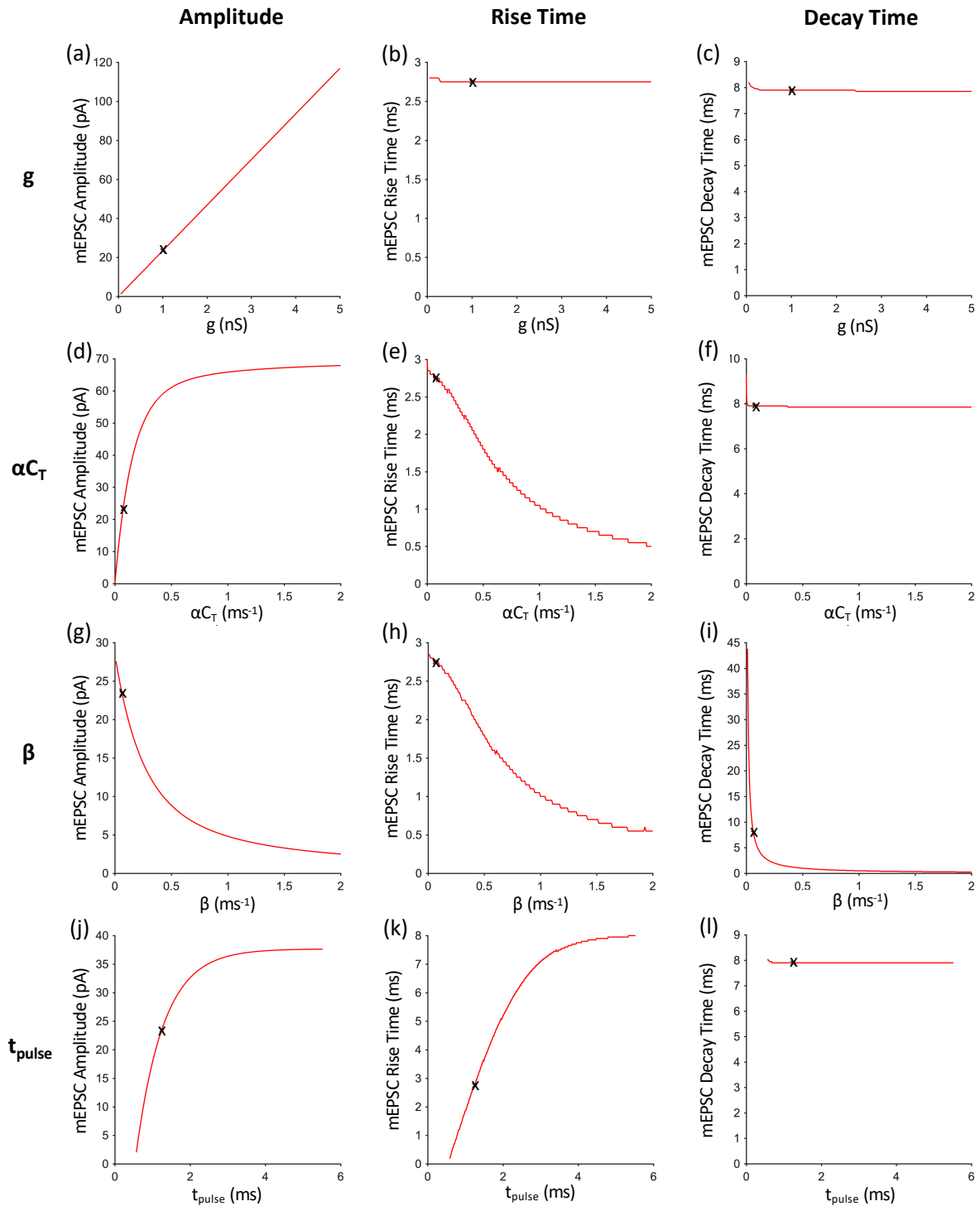


Figure 5.3 | mEPSC synapse model: parameter sensitivity. OAT parameter sensitivity analysis of the mEPSC model. The simulated mEPSC's amplitude (Col. 1), rise time (Col. 2) and decay time (Col. 3) were measured as the synapse parameters were altered, one-at-a-time, across a range of parameter values. Row 1: maximal synaptic conductance (g), row 2: product of the transmitter binding rate and the transmitter concentration (αC_T), row 3: receptor unbinding rate (β), row 4: transmitter pulse duration (t_{pulse}). **x**: best-fit parameter values obtained by fitting the simulated trace to the average recorded control mEPSC.

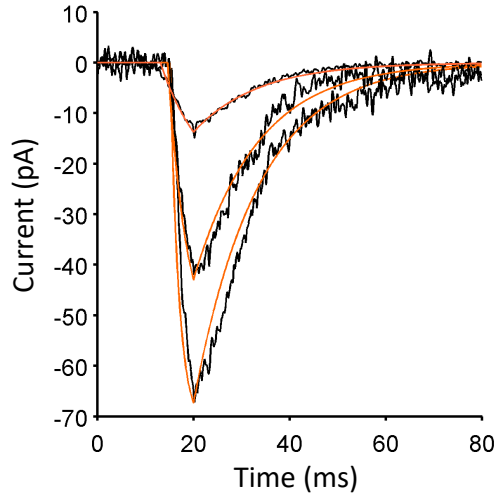


Figure 5.4 | Example fits of simulated mEPSCs to data. Examples of the mEPSC fits obtained using multivariate gradient descent, with two free variables γ and β , to parameterise the synapse model. Black line: data, Orange line: simulation

To understand how the γ , β and t_{pulse} properties contributed to the mEPSC amplitude the correlation between the fitted parameters and the mEPSC amplitudes was investigated. As is evident in Figure 5.5, γ correlated most closely with the mEPSC amplitude (Fig. 5.5b) with Spearman rank correlation coefficient, $\rho_{\gamma} = 0.62$, whereas β (Fig. 5.5d) and t_{pulse} (Fig. 5.5f) had low correlation with $\rho_{\beta} = 0.12$ and $\rho_t = 0.07$ respectively. The larger variability in the fitted parameters at lower amplitudes can be partly attributed to the relative increase in the noise from the recordings that remained after filtering.

The low dependence of the amplitude on β can be understood analytically. Given that the values of β and γ obtained through the fitting are small, the amplitude of the mEPSCs given in Equation 5.6 can be approximated using the Taylor expansion to:

$$I_{\text{max}} \approx \gamma t_{\text{pulse}} \cdot gV_m \quad (5.7)$$

where gV_m are constant throughout the fitting.

This gives approximately equal weighting to t_{pulse} and γ in determining the model amplitude but in the experimentally measured mEPSCs there was effectively no correlation between t_{pulse} and amplitude (Figure 5.5f). Therefore, it was predicted that γ captured the variability in mEPSC amplitude.

To investigate the extent to which the γ distribution alone captured the mEPSC amplitude variability, the original fitted mEPSC amplitudes were compared with the amplitudes calculated analytically from Eqn. 5.6 using only the fitted γ values and median values for β

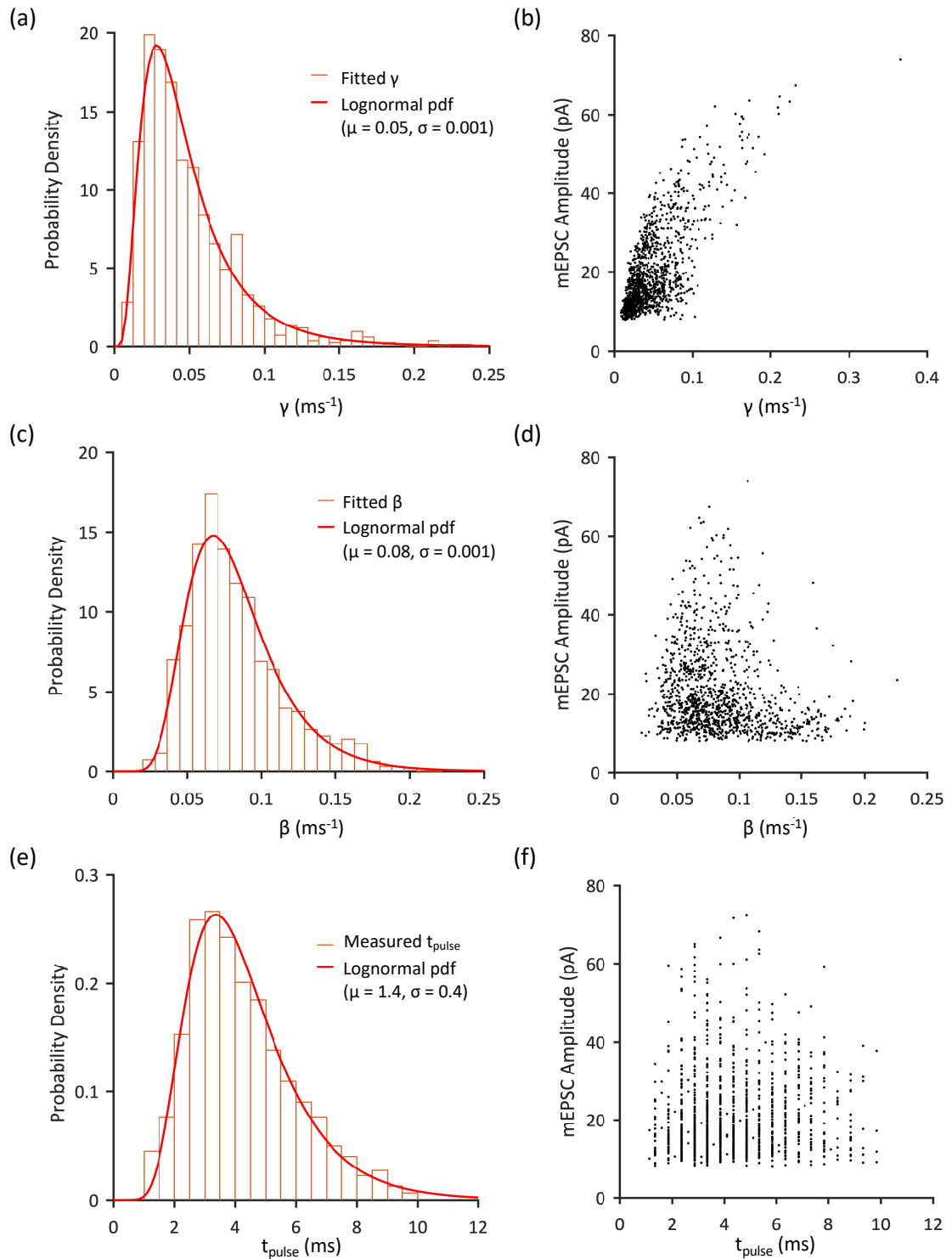


Figure 5.5 | Fitted mEPSC parameter distributions and their correlation with the mEPSC amplitudes. The fitted parameters, γ and β , were obtained by fitting to each individual experimental control mEPSCs (Rows 1 and 2). The t_{pulse} values were measured directly from the recorded mEPSCs (Row 3). (a, c and e) The probability density distributions of the parameters were best fit with lognormal distributions. (b, d and f) The fitted parameters and the associated mEPSC amplitudes had the following Spearman rank correlation coefficients: $\rho_{\gamma} = 0.62$, $\rho_{\beta} = 0.12$ and $\rho_t = 0.07$.

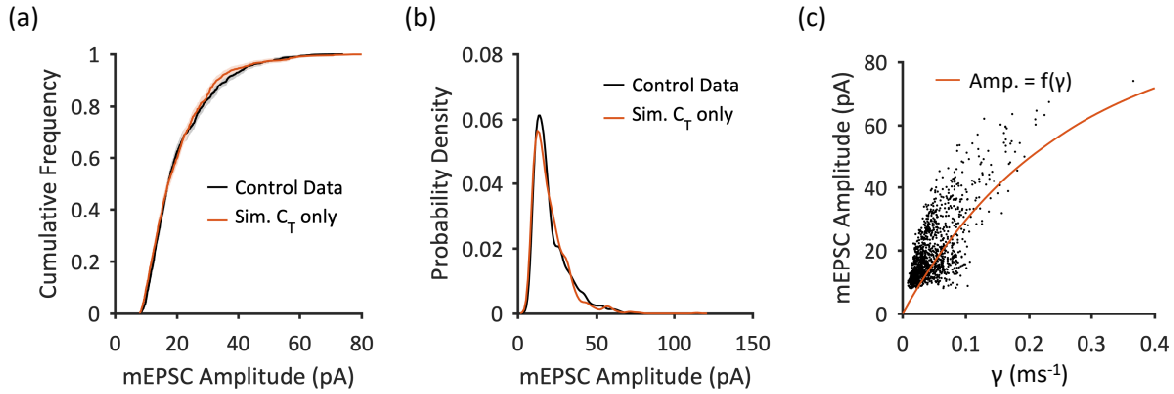


Figure 5.6 | mEPSC amplitude distribution with variability only in γ . The γ -amplitude dependence was tested by rederiving the mEPSC amplitudes from Eqn. 5.6 using only the fitted γ values and median values for β and t_{pulse} . (a) and (b) The empirical CDF and PDF distributions of the calculated mEPSC amplitudes compared to the data ($p_{\text{KS}} = 0.14$, Kolmogorov-Smirnov test). (c) The γ -amplitude relationship when $\beta = 0.08 \text{ ms}^{-1}$ and $t_{\text{pulse}} = 3.9 \text{ ms}$.

and t_{pulse} (see Figures 5.6a and 5.6b). This was equivalent to assuming the non-variable relationship, between C_T and the mEPSC amplitude that is plotted in Figure 5.6c. Although the amplitudes were not perfectly reproduced, a Kolmogorov-Smirnov goodness-of-fit test showed that this simplification still produced a good approximation of the control mEPSC amplitudes ($p_{\text{KS}} = 0.14$).

As the recorded increase in mEPSC amplitude following intracellular $A\beta$ -infusion (presented in the previous chapter) was attributed to post-synaptic alterations in the AMPAR profile and no change was evident in the pre-synaptic properties, the neurotransmitter concentration was a good candidate for incorporating the underlying mEPSC amplitude variability present in healthy cells. Therefore the fitted γ values were separated into the component variables, α and C_T . By fixing α at $0.04 \text{ ms}^{-1}\text{mM}^{-1}$ this resulted in a lognormal distribution (shown in Figure 5.7a) with parameters $\mu = 0.1$, $\sigma = 0.66$, and median $C_T \sim 1 \text{ mM}$ which is within the biological range [208].

To simulate the mEPSCs generated in control cells Monte Carlo simulations were run, with C_T drawn from the lognormal distribution. The other properties in the model were kept at the median values established through the initial fitting. In Figure 5.7b the distribution of simulated mEPSC amplitudes is compared with the amplitude of the recorded mEPSCs; the simulated amplitudes fit well to the data ($p_{\text{KS}} = 0.35$, Kolmogorov-Smirnov test) and were

significantly different from the A β -treated mEPSC amplitudes ($p_{KS} < 0.01$).

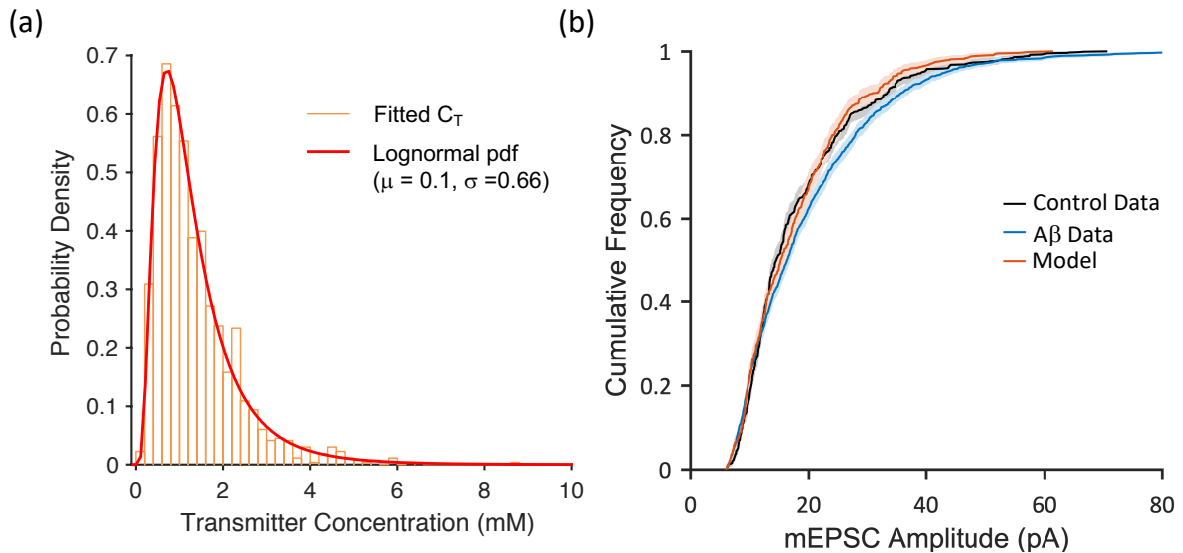


Figure 5.7 | Input and output of the parameterised mEPSC Control model. In the Control model, sampling C_T from a lognormal probability distribution ($\mu = 0.1$, $\sigma = 0.66$) simulated the inherent amplitude variability of the mEPSCs recorded in control cells. (a) The probability density of the transmitter concentration obtained by fitting the synapse model to the control mEPSC data. (b) Comparison of the recorded mEPSC amplitude distribution and the simulated distribution obtained from 1000 runs of the Control model. The model output fits well with the recorded control distribution ($p_{KS} = 0.35$, Kolmogorov-Smirnov test) and is significantly different from the recorded A β distribution ($p_{KS} < 0.01$).

5.2.2 Simulating the A β Effect

A significant increase in the AMPAR-mediated mEPSC amplitudes was recorded following acute intracellular A β -infusion (see Figure 4.8b). However, kinetics analysis of the recorded mEPSCs showed no conclusive evidence of changes in the rise time, decay time or half-width of the mEPSCs (see Figure 4.9). Therefore when simulating the A β -treated mEPSCs it was important that there was no shift in the rise and decay times alongside the increase in amplitude.

Given the model parameter sensitivities (shown in Figure 5.3), the synaptic conductance (g), which significantly alters the mEPSC amplitude with minimal alterations to the rise and decay times (row 1 of Figure 5.3), was varied to simulate the increased mEPSC amplitude distribution. Monte Carlo simulations were run for incremental steps in the synaptic

conductance from the original control model value $g_C = 0.8nS$. Simulations were run from $g = 0.5g_C$ to $g = 2g_C$ at intervals of $0.25g_C$. The resultant amplitude distributions for $0.5g_C$, g_C and $1.5g_C$ are shown in Figure 5.8. The best fit was obtained at $1.5g_C$, a 50% increase in the maximal conductance of the control from $g_C = 0.8nS$ to $g_{A\beta} = 1.2nS$.

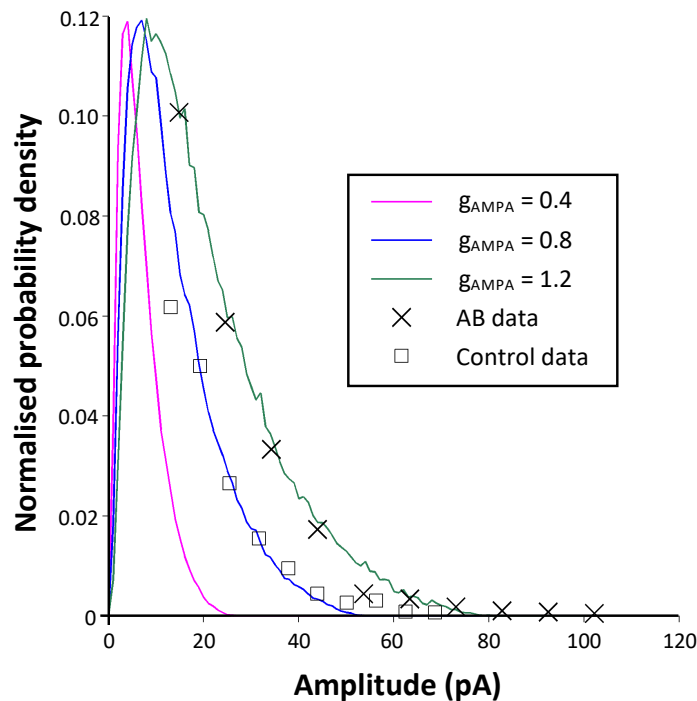


Figure 5.8 | Increased synaptic conductance simulated A β -mediated increase in mEPSC amplitude. A comparison of the mEPSC amplitudes generated through Monte Carlo simulations (1000 runs each) for different synaptic conductances ($g = 0.4, 0.8$ and 1.2) with the recorded A β and control data (presented as scaled empirical PDFs). The increase observed in control CA1 hippocampal neurons following acute A β exposure can be attributed to a 50% increase in AMPAR conductance ($p_{KS} = 0.27$, Kolmogorov-Smirnov test).

5.3 Discussion

A first-order kinetic synapse model was used to simulate the increase in AMPAR-mediated mEPSC amplitude that was observed in the experiments presented in Chapter 4. The model was first fit to the mEPSC data recorded in healthy (control) pyramidal neurons. The

inherent variability in mEPSCs was captured in the neurotransmitter concentration. To improve the fit of the model to the data a Hill function was incorporated to simulate positive cooperativity between the neurotransmitter concentration and binding in AMPARs. To reproduce the increased mEPSC amplitude distribution without altering the mEPSC kinetic properties, the conductance of the AMPARs was increased by 50%, which is in the range of the recorded increase in the EPSC study discussed in Section 4.1.2 that led to this work ([248]). This supports the hypothesis that acute A β -treatment causes an increase in the number of AMPARs and that the kinetics of the inserted receptors are unchanged. However, a more detailed synapse model (such as the NEURON simulation environment used in Postlethwaite et al. 2007 [188]) would be necessary to test the potential receptor distribution that could produce this result without impacting the kinetic properties, and to quantify the number of synapses inserted.

Future work: modelling increased CP-AMPA expression

In this work the consequence of the effect of acute A β was only considered in relation to the altered electrical response that resulted from the increased AMPAR expression. However, it was indicated by the EPSC study that the increase in synaptic transmission was potentially a result of CP-AMPA insertion [248]. There is growing interest in the contribution of CP-AMPA to the onset and progression of synaptic pathology and neurodegeneration [102, 137, 249]. A range of different experimental studies have found evidence that CP-AMPA may be involved in AD pathology. Another recent study found that acute extracellular A β application on primary hippocampal cultures caused CP-AMPA synthesis and lead to an over response in homeostatic synaptic plasticity [81]. CP-AMPA are typically homomeric GluA1 containing receptors. There is also evidence from AD mouse models of increased GluA1 phosphorylation and CP-AMPA expression prior to neuropathology [164]. These studies all used young mice so further studies need to be carried out to investigate if these processes still occur at mature synapses. Importantly, however, there is supporting evidence of increased CP-AMPA expression in human studies; increased GluA1 levels have been measured in the hippocampi of AD patients, suggesting an increase in GluA1-containing receptors [157].

A key question, if CP-AMPA expression is indeed altered, is how might any such changes contribute to AD pathology. Assuming CP-AMPA do have a physiological role in transmission and plasticity as research suggests, their dysregulation is going to have some effect. Dysregulated calcium homeostasis is believed to be an important factor in AD pathology

[139]. The over-expression of CP-AMPARs could dysregulate intracellular calcium levels leading to Ca^{2+} -excitotoxicity or other pathological processes associated with Ca^{2+} , such as tau hyperphosphorylation [93, 144, 186, 249]. Given that CP-AMPARs have different properties to CI-AMPARs (e.g. increased conductance), altered synaptic AMPAR profiles could alter synaptic excitability and dysregulate neural dynamics. For example, the disruption of homeostatic synaptic plasticity caused by CP-AMPAR over-expression could contribute to the aberrant network activity that has been detected in the early stages of AD [81]. Therefore, it would be particularly of interest for future work to use a more detailed biophysical synapse model that incorporates Ca^{2+} dynamics to investigate how increased CP-AMPAR expression might alter Ca^{2+} dynamics and the potential impact of that on the cell excitability and synaptic plasticity.

MODELLING ALTERED INTRINSIC EXCITABILITY IN A TRANSGENIC MOUSE MODEL OF AD

The overexpression of $A\beta$ has been found to dysregulate intrinsic excitability [29, 228]. Neuronal models can be used to investigate the cell membrane changes that cause this dysregulation as well as the subsequent effects on neural dynamics. The aim of the work in this chapter is to develop an improved single-compartment conductance-based CA1 model that can simulate recorded excitability data and be used to investigate the changes in intrinsic excitability in an $A\beta$ -overexpressing AD mouse model.

6.1 Background

6.1.1 $A\beta$ and Altered Intrinsic Excitability

Intrinsic excitability is the capacity of a cell to respond to electrical stimulation and to generate an action potential. The intrinsic excitability of a cell is determined by the cell's ion channel and receptor composition. Changes in the number or properties of these channels can alter the cell's intrinsic excitability thereby altering the functional response of the neuron to incoming signals and the propagation of that signal.

6.1.2 Na⁺ Channels

There are different transient Na⁺ channel subtypes; Na_v1.2 and Na_v1.6 are the predominant subtype found in excitatory neurons. They aggregate in different regions of the axon initial segment (AIS), which is the initiation site of action potentials (AP) in pyramidal neurons, and are believed to have different roles in neuronal excitability [110]. The Na_v1.6 channels, which are particularly prevalent in the distal end of the axon initial segment (AIS), have a lower voltage threshold and are believed to have a key role in AP initiation [110, 200]. The Na_v1.2 channels, which have a higher voltage threshold and are located in and near the soma, are thought to have a role in the backpropagation of APs to the soma [110]. A difference of up to 15mV in the half-activation and half-inactivation voltages have been recorded [110, 258]. A small number of studies have used computational models (in combination with experimental work) to investigate the roles of Na_v1.2 and Na_v1.6 channels in AP initiation and propagation [110, 200, 258]. These studies have incorporated the two Na⁺ channel subtypes within single-compartment Hodgkin-Huxley type models [110, 258] and also in multi-compartment pyramidal neuron models (built-in NEURON, [110, 200, 258]).

6.2 Model-Data Fitting Method

Two versions of a single-compartment CA1 pyramidal neuron model (described in Section 3.3.1) were fit to previously published intrinsic excitability data, recorded from wild-type (WT) and A β -overexpressing transgenic mice [127], to investigate which changes in cell membrane properties could lead to the altered intrinsic excitability. The two versions of the pyramidal neuron model were identical apart from the representation of the transient-Na⁺ voltage-gated ion channels; the first model included a single transient Na⁺-channel current, whereas the second model split the contribution into the two predominant transient Na⁺-channel subtypes described above.

The model fitting was primarily achieved by hand-tuning the parameters to improve the fit of the simulated outputs to the experimental data. This data included three types of voltage-recordings that were used to assess the intrinsic excitability of the cells, specifically the average AP waveforms and firing patterns evoked through positive current stimulation and the hyperpolarised 'sag' trace evoked by negative stimulation.

The model was parameterised using the data in two stages. In the first stage the aim was to improve the fit of the models to the WT data to create a 'control' model to provide a basis

for investigating what alterations in the cell properties (ion channel and membrane properties) could account for the observed differences between the WT and PDAPP mouse model. In the second stage, using the control models as the starting point, the parameters were then tuned to the PDAPP data using the same fitting process but focused on the ion channel properties suggested in the literature as potential mechanisms for these amyloidopathy-related changes [127, 255].

The intrinsic excitability data, model versions and the model fitting method are described in detail in the following sections.

6.2.1 Intrinsic Excitability Data Summary

The intrinsic excitability data, obtained from a previous study by Kerrigan et al. (2014), was recorded from CA1 pyramidal neurons in 9 - 10 month old PDAPP transgenic mice (an A β -overexpressing transgenic mouse model: Indiana mutation, V717F) and their age-matched wild-type littermate controls [127]. The PDAPP-mutation is used as a model of AD. PDAPP mice exhibit cognitive deficits, particularly in spatial and recognition memory, and also some of the characteristic features of AD, specifically extracellular A β deposition, loss of synaptic and dendritic density in the hippocampus, dystrophic neurites and gliosis [77].

Below are descriptions of the two sets of recordings carried out, with the protocol used for each recording and the properties measured. Before starting each protocol the resting membrane potential (RMP) was measured and then the membrane potential was set to approximately -80mV by injecting the required holding current.

Protocol 1: A 500ms negative current stimulation of -100pA was applied to patch-clamped neurons to measure subthreshold membrane properties.

Output: The average response recorded in both the PDAPP and WT neurons is shown in Figure 6.2, this will be referred to as the 'sag' trace throughout this Chapter. The voltage 'sag' (V_{sag}), caused by the activation of hyperpolarization-activated cyclic nucleotide-gated (HCN) channels, was measured as the difference between the maximum negative voltage (V_{maxneg}) and the hyperpolarised-steady state (V_{ss}). The membrane time constant (τ_{mem}) was calculated by fitting a single exponential to the downward slope from 10% - 95%. They found no significant change in the intrinsic subthreshold properties in the PDAPP neurons.

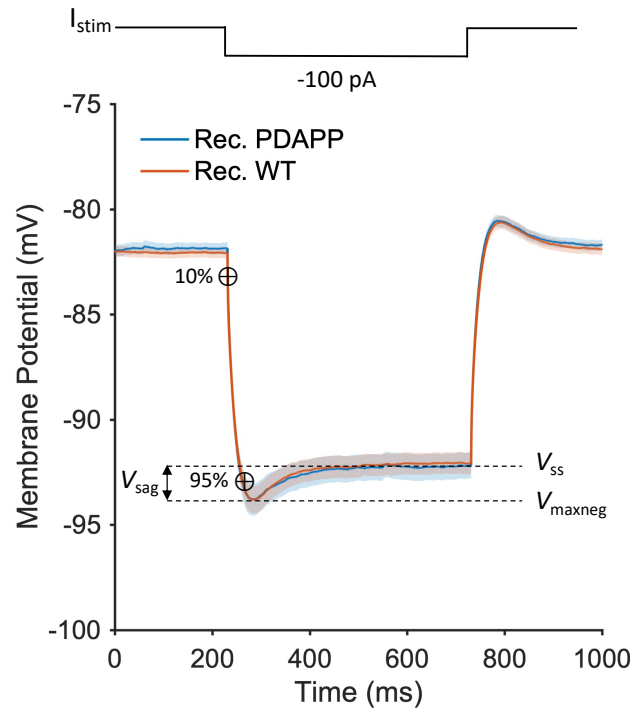


Figure 6.1 | Average hyperpolarised traces recorded in WT and PDAPP CA1 neurons. The average 'sag' traces generated by -100pA stimulation to measure the passive properties of the cell (from [127]). The membrane time constant (τ_{mem}) is measured by fitting a single exponential to the downward slope from 10% - 95%. V_{sag} is measured as the difference between the maximum negative voltage (V_{maxneg}) and the hyperpolarised-steady state (V_{ss}). The bounded-line shows the standard error mean (SEM).

Protocol 2: A 500ms positive current stimulation was applied to patch-clamped neurons at 6 different intensities from $+50\text{pA}$ to 300pA to record action potential (AP) firing properties

Output: The total number of spikes and the instantaneous firing frequencies (f_{inst}) of the first 10 spikes were measured at each stimulation intensity. The instantaneous frequency was calculated as $f_{\text{inst}} = 1/IEI$ where IEI is the inter-event interval (measured in seconds). An example of the typical evoked firing response at 300pA is shown in Figure 6.2a. The PDAPP transgenic mice displayed increased instantaneous firing frequencies for the first 10 APs (see Figure 6.6c, column 3).

The following properties were measured from the first AP generated by the $+300\text{pA}$ stimulation: AP peak voltage, maximum rate of rise (dV/dt), AP threshold (when $dV/dt > 15\text{Vs}^{-1}$), AP width (at 15mV) and after-hyperpolarisation

(AHP). AHP is the hyperpolarisation that occurs immediately after an AP, measured as the difference between the minimum voltage and the cells normal resting potential). The average APs from the WT and PDAPP-neurons is shown in Figure 6.2b. The AP width was reduced by 0.1 ms from 0.7 ± 0.01 ms in the WT mice to 0.6 ± 0.01 ms in the PDAPP transgenic mice.

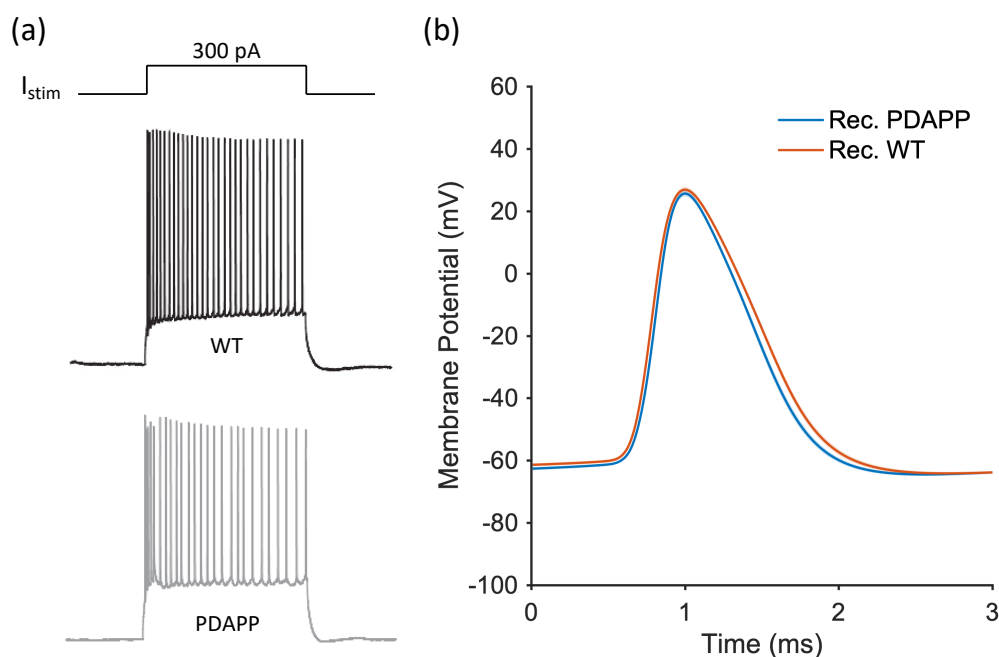


Figure 6.2 | Action potential and typical firing pattern in WT and PDAPP neurons. WT and PDAPP CA1 neuron responses to 500ms 300pA stimulation (from [127]). (a) Typical firing responses observed. (b) The average APs measured from the first spike generated at 300pA. Lines include the standard error mean (SEM).

6.2.2 The Models

To investigate the potential causes of the altered intrinsic properties in the PDAPP neurons, two versions of a single-compartment conductance-based neuronal model, which were identical apart from the representation of the transient- Na^+ voltage-gated ion channels, were parameterised by fitting to the data described above. The basis for both models was the CA1 pyramidal neuron model described in Section 3.3.1. This model was unmodified for the first version of the model, which will be referred to as the ‘single Na^+ channel model’ as it included one transient Na^+ channel (Na_T). In the second version, the pyramidal neuron model was developed by replacing the single Na_T channel with two Na_T channel subtypes:

$\text{Na}_v1.2$ and $\text{Na}_v1.6$ (briefly discussed in Section 6.1.2). These channels were added to make the model more biophysically realistic. This model will be referred to as the ‘split Na^+ channel model’.

The current equations for the two Na^+ channels had the same form as the Na_T described in Chapter 3 and were given as:

$$I_{\text{Na}_{1.2}} = g_{\text{Na}_{1.2}} m_{\text{Na}_{1.2}}^3 h_{\text{Na}_{1.2}} (E_{\text{Na}} - V) \quad (6.1)$$

$$I_{\text{Na}_{1.6}} = g_{\text{Na}_{1.6}} m_{\text{Na}_{1.6}}^3 h_{\text{Na}_{1.6}} (E_{\text{Na}} - V) \quad (6.2)$$

where $g_{\text{Na}_{1.2}}$ and $g_{\text{Na}_{1.6}}$ are the $\text{Na}_v1.2$ and $\text{Na}_v1.6$ ion channel maximal conductance; m_* and h_* represent the ion channels’ activation and inactivation functions respectively ($0 \leq m/h \leq 1$); V is the membrane potential; and E_{Na} is the Na^+ channel reversal potential. The channels activation and inactivation voltages and time constants have the same standard form as used for the other channels in the model (see Equations 3.20 and 3.21 in Section 3.3.1).

Initial Parameter Settings

The model was initially parameterised with parameter values based on biological measurements and those used in previous versions of the model [21, 109, 178]. The behaviour of the model using these initial data sets in comparison to the experimental data, is shown in Figure 6.3.

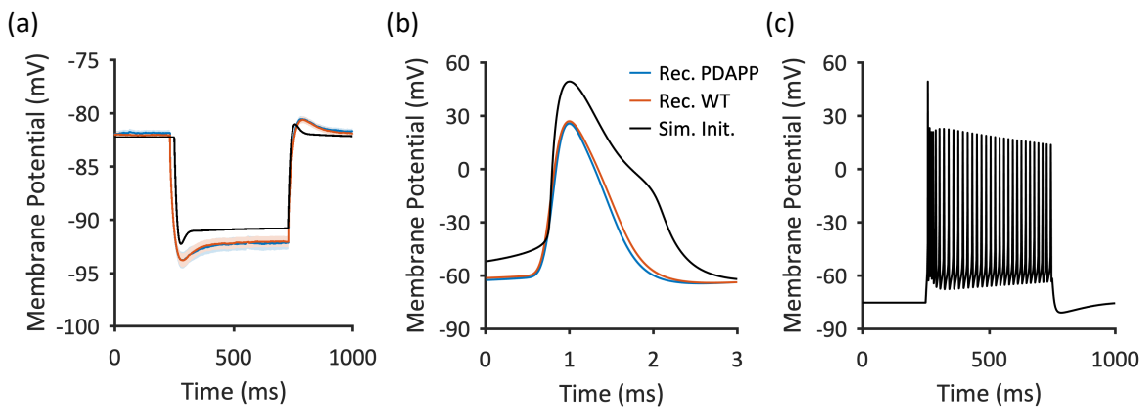


Figure 6.3 | Pyramidal neuron model behaviour with initial parameterisation. A comparison of the outputs from the single Na^+ channel model using the initial parameter set with the experimentally recorded excitability data. (a) The ‘sag’ response of the model. (b) The averaged first AP waveform. (c) The simulated firing pattern.

The initial parameters of the $\text{Na}_v1.2$ and $\text{Na}_v1.6$ channels were based on published recordings of the Na^+ currents measured in the axon and soma of pyramidal neurons from

the prefrontal cortex of 2-3 week old rats [109]. The somatic currents were interpreted as $\text{Na}_v1.2$ mediated currents and the axonal currents as $\text{Na}_v1.6$ mediated currents in line with experimental observations [109, 200]. Figure 6.4 shows the recorded Na^+ channel activation and inactivation curves fitted with the Boltzmann equation: the half-activation and half-inactivation voltages were $-29.7 \pm 1.0\text{mV}$ (with Boltzmann constant, $k_B = 5.8 \pm 0.2$) and $-67.0 \pm 1.7\text{mV}$ ($k_B = 7.1 \pm 0.3$) at the soma and $-43.9 \pm 1.3\text{mV}$ ($k_B = 5.7 \pm 0.2$) and $-80.0 \pm 1.0\text{mV}$ ($k_B = 5.4 \pm 0.2$) in the axon.

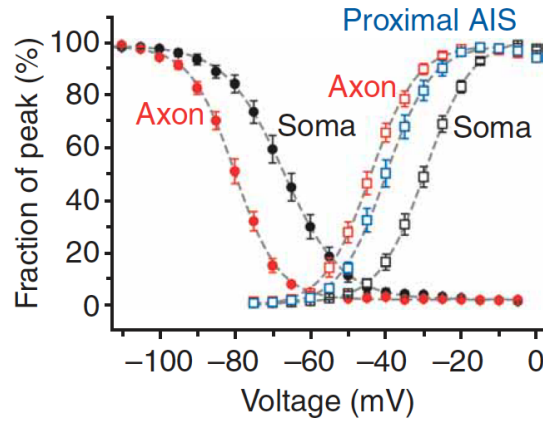


Figure 6.4 | Published Na^+ ion channel kinetics. Na^+ channel activation voltage and deactivation functions recorded from the soma and axon (and AIS) of a pyramidal neuron by Hu et al. (2009) [109]. These were used to inform the $\text{Na}_v1.2$ and $\text{Na}_v1.6$ channel parameters in the split Na^+ channel model.

Simulating the Experimental Protocols

To parameterise the cell model using the experimental data, the two stimulation protocols described above were simulated *in silico*. To implement the experimental set up and the 500ms current injections within the model:

- The 500ms negative current (-100 pA) and positive current injections (100, 200 and 300 pA) were converted to current densities for use in the model (with units of $\mu\text{A}/\text{cm}^2$). This was calculated using Equation 6.3:

$$I_{\text{model}} = I_{\text{exp}} \frac{C_m}{c_m} = \frac{I_{\text{exp}}}{A} \quad (6.3)$$

where c_m is the total capacitance measured in the whole-cell patch experiments ($c_m \approx 140\text{pF}$), C_m is the standard approximation for the specific membrane capacitance of a lipid membrane ($C_m \approx 1\text{F}/\text{cm}^2$) and A is the approximate area of the

cell membrane (in cm^2) [87]. Using this method, a 100 pA injection current in the experiment was equivalent $0.7 \mu\text{A}/\text{cm}^2$ in the cell model.

- The models' voltage-gated ion channel reversal potentials (E) were calculated from the ionic concentrations of the intracellular and extracellular recording solutions using the Nernst Equation [104].
- A holding current was applied to hold the cells at -80mV , as in the experiments.

6.2.3 Fitting Method

The purpose of the fitting was to improve the behaviour of the following model outputs in comparison with the experimental data:

- The simulated 'sag' trace, which was generated by negative stimulation as described in Protocol 1.
- The simulated firing pattern generated at each stimulation level, as described in Protocol 2.
- The simulated AP, which was the first AP generated by the 300pA (equivalent to $2.1 \mu\text{A}/\text{cm}^2$ in the model) current stimulation, as described in Protocol 2.
- The model cell's RMP.

This was a complex problem as it involved optimisation across multiple behaviours. The fitting was primarily carried out by hand-tuning the parameters. An automated fitting algorithm was also used to identify parameter settings by fitting to measures from the AP and 'sag' traces, but these identified parameter sets performed poorly at reproducing the observed firing patterns and required significant further manual tuning. Hand-tuning of parameters is an iterative, empirical process informed by a combination of goodness-of-fit measures and visual inspection. For this reason, it is difficult to explicitly state all parameter changes that were investigated during the fitting process. Therefore the preceding text is focused on the general considerations that informed the fitting process.

The process for tuning parameters involved starting with small iterations around the initial values to investigate their individual impact on the different behaviours (within that parameter space). Then, as knowledge was gained, combinations of parameters were simultaneously altered and, if necessary, larger variations from the initial values were tested. To ensure the model remained biologically representative throughout the fitting, the majority of the model parameters were fixed at the original experimentally-informed values, with the

remaining free parameters constrained to biologically reasonable ranges. As the ion channel conductances have been less well-defined biologically, these parameters were the primary focus when fitting to both the WT and the PDAPP data. The parameterisation of the PDAPP was focused on a subset of the ion channels, specifically the delayed-rectified K^+ channel and the transient Na^+ channel which were suggested as potential mechanisms for these amyloidopathy-related changes [127, 130, 255].

The fitting was assessed both visually and by taking into account the following measures:

- The goodness of fit of the simulated AP trace to the data, measured using the RMSD.
- The AP peak, width, threshold and AHP values.
- The instantaneous frequencies of the oscillations at each stimulation level.
- The characteristics of the simulated firing pattern during the 500 ms stimulation. Specifically, their duration, as they should continue throughout the 500 ms stimulation, and the overall shape of the firing pattern (governed by the peaks and troughs).
- The goodness of fit of the ‘sag’ trace, measured using the RMSD and the ‘sag’ voltage (V_{sag}).
- The membrane time constant (τ_{mem}).
- The RMP of the cell.

In the initial stages of the fitting, priority was given to the cell’s RMP, the firing frequency and the AP peak and width. As the fit of these priority measures improved, the other aspects of the behaviour were also considered, such as the overall fit to the AP waveform which included the AP threshold and the AHP as well as qualitative features of the firing pattern. The goodness of fit of the ‘sag’ trace was monitored throughout but was fine-tuned in the later stages of the fitting process. This was because the HCN voltage-gated ion channel properties, which govern V_{sag} , have a minimal impact on the AP waveform and firing frequency. The other ion channel properties, however, do impact on the membrane time constant (measured from the falling voltage of the ‘sag’-trace, see Section 6.2.1) and therefore alter the fit of the simulated ‘sag’ trace to the data.

6.3 Model Fitting Results

6.3.1 Single Na⁺ Channel Model

To simulate the intrinsic excitability recordings from the 9 - 10 month old mice the original model was first fit to the WT data (as described in the previous section). The majority of the fitting was achieved by altering the ion-channel conductances of the original model. However, to lower the AP threshold to a value closer to that observed experimentally (compared to the original model output), the activation threshold voltage of the Na_T-channel was lowered. The activation and inactivation functions used in the model are shown in Figure 6.5, the kinetics that were altered to fit the data are indicated by dashed lines. The final WT fitted parameter set are listed in Table 6.1 with the initial values given in brackets if they were modified during the fitting.

Table 6.1 | CA1 pyramidal neuron model parameters: WT-fitted values vs. initial values. Voltage-gated ion channel parameters used to simulate the WT CA1 neuron data with the initial parameter values given in brackets for those that were modified.

Channel	E(mV)	g(mS/cm ²)	V(mV)		k(mV)		τ(ms)	
			m	h	m	h	m	h
Na _T	55 (60)	48 (65)	-50.0 (-37.0)	-75.0	7.0 (5.0)	-7.0	-	-
Na _P	55 (60)	0.26 (0.1)	-45.0 (-47.0)	-	3.0	-	$\tau_{h_{Na_T}}$	-
Ca _T	90	1.0 (0.6)	-54.0	-65.0	5.0	-8.5	2.0	15.0 (32)
Ca _H	90	1.1 (2.6)	-15.0	-60.0	5.0	-7.0	0.08	300.0
K _{DR}	-100 (-85)	6.8 (9.5)	-5.8	-68.0	11.4	-9.7	1.0	1400
K _M	-100 (-85)	0.8	-30.0	-	10.0	-	75.0	-
h _f	-30	0.011 (0.05)	-82.0 (-102)	-	-13.0	-	15	-
h _s	-30	0.011 (0.05)	-82.0 (-102)	-	-6.0	-	210	-
L	-55 (-65)	0.005 (0.02)	-	-	-	-	-	-

Figure 6.6 shows the results of the fitting of the model to both the WT and PDAPP experimental data. The fitted models were capable of simulating the key features of both the WT and PDAPP intrinsic excitability recordings and reproduced the changes observed. The fit to the PDAPP data was obtained by increasing the current contribution from the Na_T channel and the delayed-rectifier K⁺ channel (K_{DR}), via the conductance, and by decreasing the activation rate of the K_{DR} channel. The ion channel parameters of the fitted models are listed in Table 6.2, the properties altered to fit the PDAPP data are shown in brackets.

In terms of the behaviour of the WT model, the AP peak and width of the WT simulation matched the experimental measurements (see Figure 6.6a), however it proved difficult to

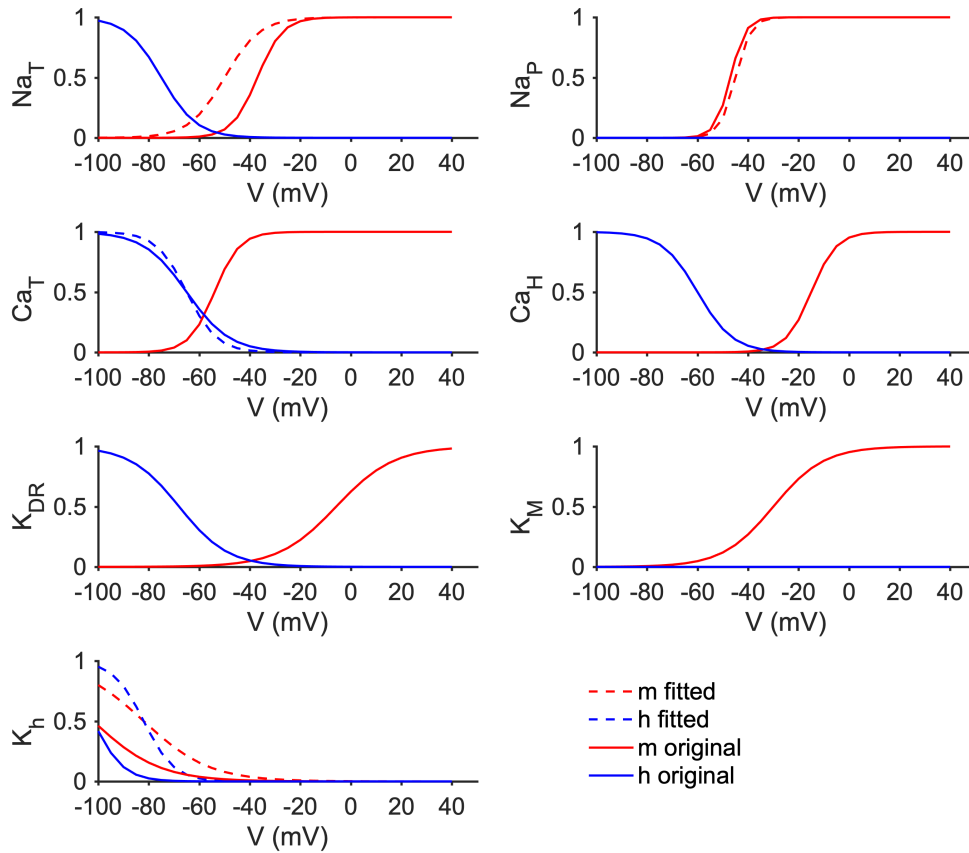


Figure 6.5 | Single Na^+ model ion channel kinetics. These figures show the ion channel activation (m) and deactivation (h) functions. The solid lines show the original versions presented in [178], the dashed lines show those that were altered for the fitted single Na^+ channel model. The half-activation voltage of the Na_T channel was decreased from -35mV to -50mV .

reduce the after-hyperpolarisation (AP tail) without significantly altering the dynamics of the cell firing. The response of the model to negative stimulation fitted with the experimental data although the recovery on the rebound was slightly faster than experimentally observed (see Figure 6.6b). The goodness-of-fit of the simulated AP waveform and the simulated ‘sag’ trace to the data, assessed using the RMSD, were 3.5 mV and 7.32 mV respectively. The firing frequency (first two columns of Figure 6.6c) and instantaneous frequency (third column of Figure 6.6c) of the first ten spikes was slower than recorded for the 50 pA and 100 pA positive stimulation, however it was within the range of the data at the higher currents ($>150\text{ pA}$).

By altering the parameters of the WT model it was possible to simulate the behaviour of the recorded PDAPP data, specifically the observed decrease in AP width and increase in instantaneous frequency (described in Section 6.2.1). The parameterised model reproduced the observed decrease in the AP width, from 0.7 ms in the WT to 0.6 ms in the PDAPP model (Figure 6.6a). There was a slight shift in the response to the negative stimulation (see Figure 6.6b) but this remained within the error bounds of the recordings. The goodness-of-fit of the simulated AP waveform and the simulated ‘sag’ trace to the data, assessed using the RMSD, were 4.5 mV and 7.33 mV respectively. There was a slight increase in the firing frequency in the PDAPP simulation which was not observed experimentally (see Figure 6.6c). However the simulated instantaneous frequency was in agreement with the experimental data, with an increase in frequency in the PDAPP model simulations.

Table 6.2 | Single Na⁺ channel CA1 neuron model: voltage-gated ion channel parameters. Voltage-gated ion channel parameters used to simulate the WT and PDAPP CA1 neuron data with the single Na⁺ channel model. The parameters that were altered to fit to the PDAPP data are written in brackets.

Channel	E(mV)	g(mS/cm ²)	V(mV)		k(mV)		τ (ms)	
			m	h	m	h	m	h
Na _T	55	48 (50)	-50.0	-75.0	7.0	-7.0	-	-
Na _p	55	0.26	-45.0	-	3.0	-	$\tau_{h_{NaT}}$	-
Ca _T	90	1.0	-54.0	-65.0	5.0	-8.5	2.0	15.0
Ca _H	90	1.1	-15.0	-60.0	5.0	-7.0	0.08	300.0
K _{DR}	-100	6.8 (7.2)	-5.8	-68.0	11.4	-9.7	1.0 (0.85)	1400
K _M	-100	0.8	-30.0	-	10.0	-	75.0	-
h _f	-30	0.011	-82.0	-	-13.0	-	15	-
h _s	-30	0.011	-82.0	-	-6.0	-	210	-
L	-55	0.005	-	-	-	-	-	-

6.3.2 Split Na⁺ Channel Model

The split Na channel pyramidal neuron model is described in Section 6.2.2. Initially the other parameters in the model were based on those from the fitting of the single Na⁺ channel model. The model was then fit to the WT data as described in the previous section. The majority of the fitting was achieved by altering the ion-channel conductances. However, to achieve a lower AP threshold (as with the single Na⁺ channel model) the activation threshold of the Na_v1.6 channel was lowered from the initial values shown in Figure 6.4 (discussed in Section 6.2.2). This was deemed to be biologically reasonable as the original channel properties were recorded in young mice (< 1 month old) and a decrease of approximately 6

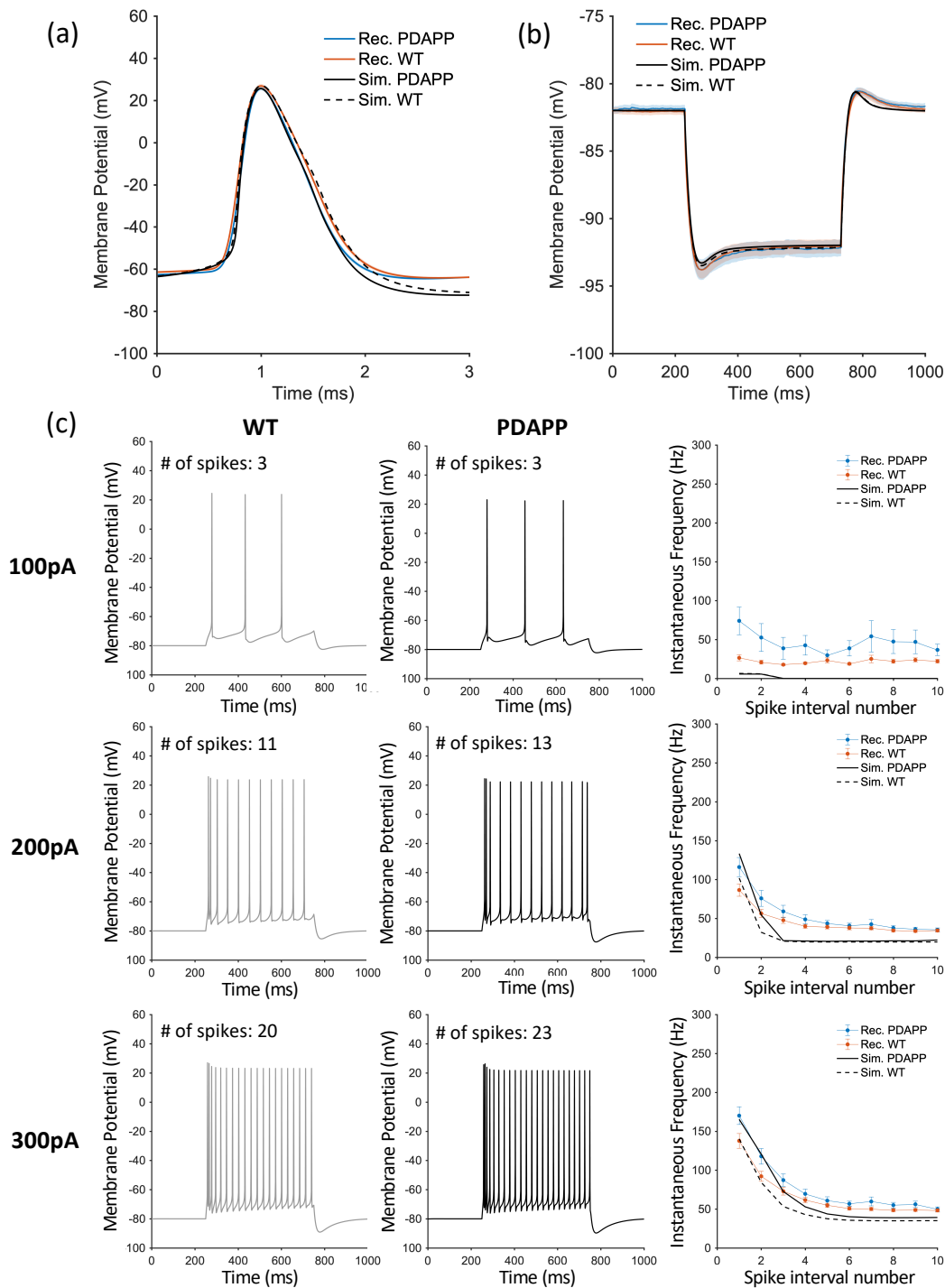


Figure 6.6 | PN model-data comparison: single Na^+ channel. Comparisons of the simulated WT and PDAPP intrinsic excitability properties generated using the single Na^+ channel model with the recorded WT and PDAPP data. (a) The difference in width of the WT and PDAPP APs (0.1ms) was matched by the model. The RMSD of the simulated WT and PDAPP AP waveforms to the data were 3.5 mV and 4.5 mV respectively. (b) The 'sag' voltage was unchanged by the parameter alterations agreeing with the experimental findings. The RMSD of the simulated WT and PDAPP 'sag' waveforms to the data were 7.32 mV and 7.33 respectively. (c) The simulated firing frequencies matched the data at the higher stimulation currents.

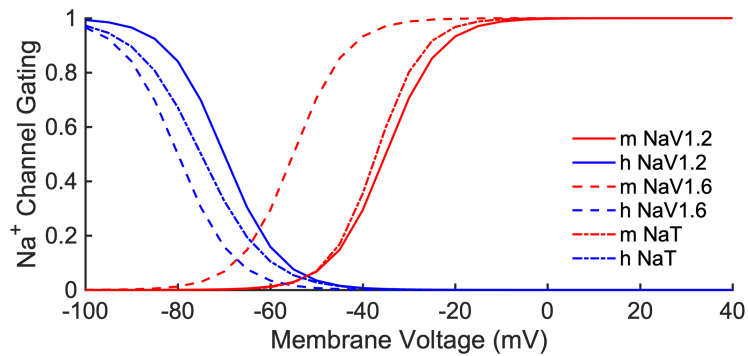


Figure 6.7 | Split Na^+ model $\text{Na}_v1.2$ and $\text{Na}_v1.6$ channel kinetics. Comparisons of the activation voltage (m) and deactivation (h) functions of the original single Na_T -channel and those of $\text{Na}_v1.2$ and $\text{Na}_v1.6$ channels used in the split Na^+ -channel model

mV has been observed in the Na^+ half-activation voltage in 9-10 month old mice compared to younger 1-2 month old mice [29]. The Na^+ channel activation and inactivation functions used in the model are shown in Figure 6.7 alongside the single Na_T channel functions.

Figure 6.8 shows the results from fitting the model to both the WT and PDAPP experimental data. The fitted models were capable of simulating the key features of both the WT and PDAPP intrinsic excitability recordings and reproduced the changes observed experimentally, although not as closely as the single Na^+ channel model. Similar to the single Na^+ channel model, the fit to the PDAPP data was obtained by increasing the current contribution from the Na_T channel and K_{DR} channel, via the conductance, and by decreasing the activation rate of the K_{DR} channel. The ion channel parameters of the fitted models are listed in Table 6.3, the properties altered to fit the PDAPP data are shown in brackets.

In terms of the behaviour of the WT model, the AP peak and width of the WT simulation matched the experimental measurements (see Figure 6.8a), and the after-hyperpolarisation (AP tail) was reduced compared to the single Na^+ channel model. Figure 6.8b shows the response of the model to negative stimulation, the negative peak and the hyper-polarised steady-state levels were within the range of the experimental values. However, the time course of the response was quicker than that observed experimentally. The goodness-of-fit of the simulated AP waveform and the simulated ‘sag’ trace to the data, assessed using the RMSD, were 2.81 mV and 7.41 mV respectively. The number of spikes evoked in the simulations of the 500 ms positive stimulations fell within the range of the experimental data for the medium intensity currents (150 - 250 pA). However, the responses to the high and low intensity were slightly above and below the recorded values respectively (see first

column of Figure 6.8c). The instantaneous frequency of the first ten spikes was slower than recorded for the 50 pA and 100 pA positive stimulation (see third column of Figure 6.8c), however it was within the range of the recorded data at the higher currents (>150 pA).

Table 6.3 | Split Na⁺ channel CA1 neuron model: voltage-gated ion channel parameters. Voltage-gated ion channel parameters used to simulate the WT and PDAPP CA1 neuron data with the split Na⁺ channel model. The parameters that were altered to fit to the PDAPP data are written in brackets.

Channel	E(mV)	g(mS/cm ²)	V(mV)		k(mV)		τ (ms)	
			m	h	m	h	m	h
Na _v 1.2	60	40	-35.0	-70.0	5.7	-6.0	-	-
Na _v 1.6	60	60 (65)	-55.0	-80.0	5.7	-6.0	-	-
Na _p	60	0.1	-47.0	-	3.0	-	$\tau_{h_{NaT}}$	-
Ca _T	90	0.8	-54.0	-65.0	5.0	-8.5	2.0	15.0
Ca _H	90	1.3	-15.0	-60.0	5.0	-7.0	0.08	300.0
K _{DR}	-85	8.8 (8.5)	-5.8	-68.0	11.4	-9.7	1.25 (1.0)	1400
K _M	-85	2	-30.0	-	10.0	-	75.0	-
h _f	-30	0.035	-102.0	-	-13.0	-	15	-
h _s	-30	0.035	-102.0	-	-6.0	-	210	-
L	-75	0.018	-	-	-	-	-	-

By altering the parameters of the WT model it was possible to qualitatively reproduce the changes in the recorded PDAPP data, specifically the observed decrease in AP width and increase in instantaneous frequency (described in Section 6.2.1). The AP generated by the PDAPP model was only 0.07ms narrower than the AP generated by the WT model, compared to 0.1ms in the data (see Figure 6.8a). In agreement with experimental observations, there was no shift in the response to the negative stimulation (see Figure 6.8b). The goodness-of-fit of the simulated AP waveform and the simulated ‘sag’ trace to the data, assessed using the RMSD, were 2.83 mV and 7.54 mV respectively. There was a slight increase in the number of spikes in the PDAPP simulation during the positive current stimulation which was not observed experimentally (see first two columns of Figure 6.8c) and the simulated instantaneous frequency for the PDAPP was higher than observed experimentally. However, the PDAPP instantaneous frequency was also higher than the simulated WT which qualitatively agreed with the recorded data (see third column of Figure 6.8c).

CHAPTER 6. MODELLING ALTERED INTRINSIC EXCITABILITY IN A TRANSGENIC MOUSE MODEL OF AD

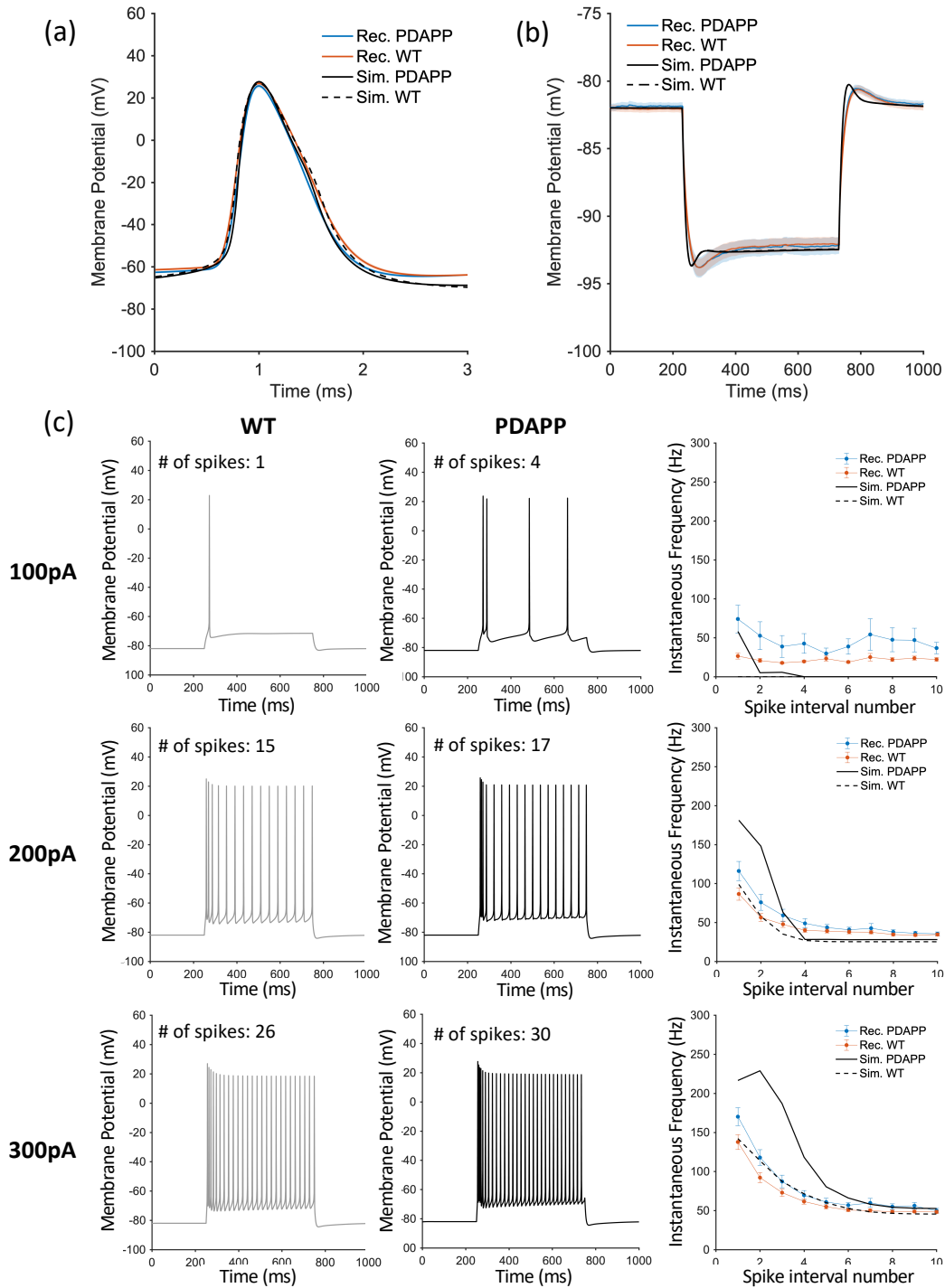


Figure 6.8 | PN model-data comparison: split Na⁺-channel. Comparisons of the simulated WT and PDAPP intrinsic excitability properties generated using the split Na⁺ channel model with the recorded WT and PDAPP data. (a) The simulated difference between WT and PDAPP AP width (0.07 ms) was smaller than in the data (0.1 ms). The RMSD of the simulated WT and PDAPP AP waveforms to the data were 2.81 mV and 2.83 mV respectively. (b) The ‘sag’ was unchanged by the parameter alterations. The RMSD of the simulated WT and PDAPP ‘sag’ waveforms to the data were 7.41 mV and 7.54 respectively.

Figure 6.8 (continued) (c) Although the PDAPP firing frequency was faster than experimentally observed the changes in the firing frequency qualitatively agreed with the experimental results.

6.4 Discussion

The intrinsic excitability data recorded in CA1 pyramidal neurons from 9 - 10 month old WT and PDAPP transgenic mice was simulated using two different versions of a single compartment CA1 pyramidal neuron model; one incorporating a single Na_T channel and the other with two Na_T channels. The original model was extended to include the Na_T channels $\text{Na}_v1.2$ and $\text{Na}_v1.6$, which are the most common subtypes found in pyramidal neurons, to make the model more biologically realistic. The original model was previously parameterised using ion channel properties based on experimental recordings from CA1 neurons [178, 228]. When fitting the model to the intrinsic excitability data, with the exception of the Na_T channel properties, few changes in the ion channel kinetic properties were required, with alterations in the ion channel conductances sufficient to reproduce the WT data. To fit the AP threshold the Na_T channels half-activation and inactivation voltages were lowered by approximately 10 mV from the original values taken from published ion-channel kinetic data recorded in young mice. This was considered biologically reasonable because of the evidence of lower Na^+ channel threshold gating in aged mice [29].

Following parameterisation both models were able to reproduce aspects of the key features of the recorded WT intrinsic excitability data. Both matched the AP peak and the 'sag' voltage and had firing frequencies close to the experimental values. Overall, the PDAPP single Na^+ channel model performed slightly better, matching both the AP width and producing a better fit to the full 'sag' trace. The split Na^+ channel model was still able to qualitatively reproduce the experimental observations and produced a closer fit to the full AP waveform but further work is required to improve the sag response generated by negative stimulation and to address the fast initial firing rate.

In both models the altered intrinsic excitability properties recorded in the PDAPP mice could be accounted for by lowering the K_{DR} and Na_T channel conductance and slowing the K_{DR} channel response. Changes in K^+ and Na^+ channel currents have previously been associated with $A\beta$ [29, 228]. In the experimental observations it was also noted that there was an increase in the after-depolarisation (ADP) in the PDAPP cells (Fig. 5F in [127]). In this work the model was not specifically fit to this aspect of the data, nevertheless, the WT and PDAPP simulations in the split Na^+ model qualitatively reproduced this change. The

model could be further improved by also fitting to the ADP data. In the paper where the WT and PDAPP data was published, it was suggested that the underlying mechanisms could be a result of increased K_{DR} channel contribution (opposite to the findings presented here), reduced contributions from voltage-gated Ca^{2+} channels or through faster Na^{+} channel inactivation [127]. Preliminary simulations carried out to test these suggestions proved unsuccessful at reproducing the changes, however further work is required to robustly investigate the proposed mechanisms.

The data-informed split Na^{+} channel model that was developed can simulate intrinsic excitability recordings enabling future use in work investigating altered neuronal excitability properties. With data-informed parameterised models it is possible to make biologically plausible suggestions as to the potential mechanisms that underlie AD or $A\beta$ -related changes in neuronal activity. Altered intrinsic excitability has also been observed in the interneurons in PDAPP mice and model fitting begun (unpublished). These parameterised models could be incorporated within a network model to investigate the effect of the altered excitability on oscillatory activity in the CA1 (as in Chapter 5).

INVESTIGATING THE IMPACT OF A β -RELATED CHANGES IN NEURONAL ACTIVITY ON GAMMA FREQUENCY OSCILLATIONS

The network model was used to investigate how the altered cell excitability in PDAPP CA1 neurons, as described in Chapter 6, may be impacting the gamma activity in the PDAPP mice and also to investigate how A β -enhanced synaptic transmission at excitatory synapses, based on the measurements from CA1 pyramidal neurons in Chapters 4 and 5, may alter oscillatory activity in the CA1 region. The tests with the altered synaptic conductance were only run on the WT network as the synaptic effects were recorded following acute A β exposure in WT mice whereas the fitted cells in the PDAPP network were from aged PDAPP-transgenic mice where it is assumed prolonged and significant A β exposure has already occurred.

7.1 Gamma Oscillations in the Hippocampus

Gamma frequency oscillations, which have a frequency range of ~25 – 100 Hz, are one of the three principal rhythms detected within the hippocampus, along with the theta rhythm (~4 – 12 Hz) and sharp wave ripples (~110 – 250 Hz) [45]. The presence of these rhythms has been found to correspond with specific behaviours and is therefore believed to have distinct roles in hippocampal processing. Of particular relevance to AD is the association of gamma oscillations with learning and memory [27, 70, 107]. Gamma oscillations have been recorded both *in vivo* and *in vitro* in the CA1 region, which is a locus of gamma oscillations

in the hippocampus. The oscillations can be split into low (25 – 60 Hz) and high frequency oscillations (55 –100 Hz), which are believed to be created by different inputs and propagate to different regions [45, 207]. Low frequency gamma leads to increased coherence with inputs from the CA3 whereas the higher frequency is associated with increased coherence with the EC. Both pyramidal neurons and fast-spiking parvalbumin interneurons are involved in the generation of gamma oscillations [220]. The model is then incorporated in an E-I network composed of CA1 pyramidal and fast-spiking interneurons to investigate how this increase in synaptic transmission may impact gamma frequency oscillations, which are believed to have an important role in memory function.

7.2 The EI Network Model

7.2.1 Network Model Set-Up

The excitatory-inhibitory (EI) network model used to generate gamma frequency oscillations is described in detail in Section 3.4. This model is an extension of the one developed by Kopell et al. (2010) [135], with the original E-cell model replaced by the pyramidal neuron model used in Chapter 6 (see Section 3.3.1 for the cell model details). The base network model, used to represent normal behaviour in control conditions, uses the E-cell parameters obtained by fitting to the WT pyramidal neuron data in Chapter 6. As in the original model, the network is homogeneous, where the cells are identical within a population and the synaptic strengths between populations are uniformly distributed and had all-to-all connectivity.

Gamma frequency oscillations were generated by applying a direct stimulating current to the E-cells ($I_{det,e}$). This stimulation protocol simulates the pyramidal-interneuronal network gamma (PING) generation mechanism [135], which can be induced experimentally through optogenetic stimulation for example [2, 16, 67]. In all simulations, the external currents were applied throughout the simulation, which had a run-time of 200ms with a 50ms run-in. Longer simulation run-times did not significantly alter the properties of the oscillations generated. It is worth noting that as the network did not incorporate any synaptic plasticity, the validity of comparing the predictions made here with experimental results would reduce as the recording time increases.

To make the network simulations more realistic, stochasticity was added to the network in two ways: by initialising the cells at different voltages, which were drawn from a gaussian distribution centred around their resting potential, and by including spontaneous excitatory

synaptic transmission, modelled as an independent poisson process, to both E and I-cell populations. For all investigations Monte-Carlo simulations ($n = 20$) were carried out.

7.2.2 Network Activity Measures

The local field potential (LFP) of each simulation was estimated using an adaptation of the model presented in Bedard et al. (2010) [15], which has previously been used in work simulating experimental LFP recordings in the CA3 region [16]. In this approximation the cells are treated as point sources, normally distributed at a distance of r_j from the hypothetical recording site. Assuming a homogeneous extracellular medium of resistivity R_e , the contributions of the individual cell currents (I_j) are then scaled relative to their distance from the recording site. The LFP is therefore given by:

$$V_{LFP} = \frac{R_e}{4\pi} \sum_j \frac{I_j}{r_j} \quad (7.1)$$

with R_e estimated at $230 \Omega \text{ cm}$ [193] and with the hypothetical distance between the cell and the recording site r_j drawn from a random distribution with $\mu = 75 \mu\text{m}$ and $\sigma = 6$, which was informed by estimations on LFP ranges from [147]. Based on the work presented in [16], which scaled the size of the simulated LFP to levels in agreement with experimental CA3 LFP recordings, the LFP was calculated from a subset of the cells (40 E-cells and 10 I-cells).

The power spectral density (PSD) of the LFP was then calculated by applying a fast fourier transform to the LFP using the Chronux toolbox package [6, 20]. Three measures from the PSD are used to summarise the oscillations: the total power of the oscillations in the gamma frequency range, calculated from the integral of the PSD; the fundamental frequency of the oscillations and the maximum PSD value at the fundamental frequency.

7.2.3 Original and Extended Network Behaviour

Summaries of the behaviour generated by applying a driving current to E-cells in the original network (from [135]) and in the extended network with and without the stochastic input (noise), are shown in Figure 7.1. The gamma frequency oscillations were obtained in the extended network by altering the external drive ($I_{\text{det,e}}$) and the conductance of the inhibitory synaptic inputs to the E-cells (g_{IE}), whilst keeping the other network properties at their original values (a list of all the network properties and their initial values are given in Table C.2 in Appendix C).

Figure 7.1a shows examples of the network activity generated during a single simulation. The firing times of all the cells in the network are shown in the raster plots (row 1), with example E and I-cell firing patterns below (rows 2 and 3). For each example simulation, the local field potential (LFP; row 4) is presented along with the corresponding power spectral density in the gamma frequency range (PSD; row 5). Typically there are two peaks present in the PSD, the fundamental frequency and the first harmonic of the oscillations. The results of the Monte Carlo simulations are summarised in Figure 7.1b, which compares the total power of the oscillations in the gamma frequency range (gamma power), the fundamental frequency of the oscillations and the associated peak PSD value.

Overall, the network incorporating the extended E-cell model produced gamma oscillations with the same general characteristics as the original model; there was no significant difference in any of the three summary properties in Figures 7.1b. The addition of noise to the extended model decreased both the frequency and gamma power of the oscillations, which can be explained by the behaviour of the individual E-cells which no longer fired every cycle (Fig. 7.1a: Row 2). However, further tests (described in the next section) showed that the oscillations generated by the two versions of the extended network model had similar levels of robustness and were in agreement with previously published work on the robustness of the original model [24, 25, 135]. Consequently, for the results in this chapter, only the extended network model with synaptic noise was used as it is more biologically realistic.

7.3 Robustness of the Network Oscillations

Prior to investigating the impact of any $A\beta$ -related alterations on the properties of the network gamma oscillations, robustness tests were run to investigate the dependence of the network behaviour on the parameters chosen for the network construction and external stimulation, and dependence on the network homogeneity. The robustness of the network gamma generation to variations in these properties was investigated using one-at-a-time (OAT) sensitivity analysis.

7.3.1 The Robustness Tests

Eight different robustness tests were performed. The tests can be categorised into three groups: tests 1 - 3 focus on the importance of the general network properties on the network behaviour; tests 4 - 6 focus on the external stimulation settings; tests 7 - 8 are preliminary

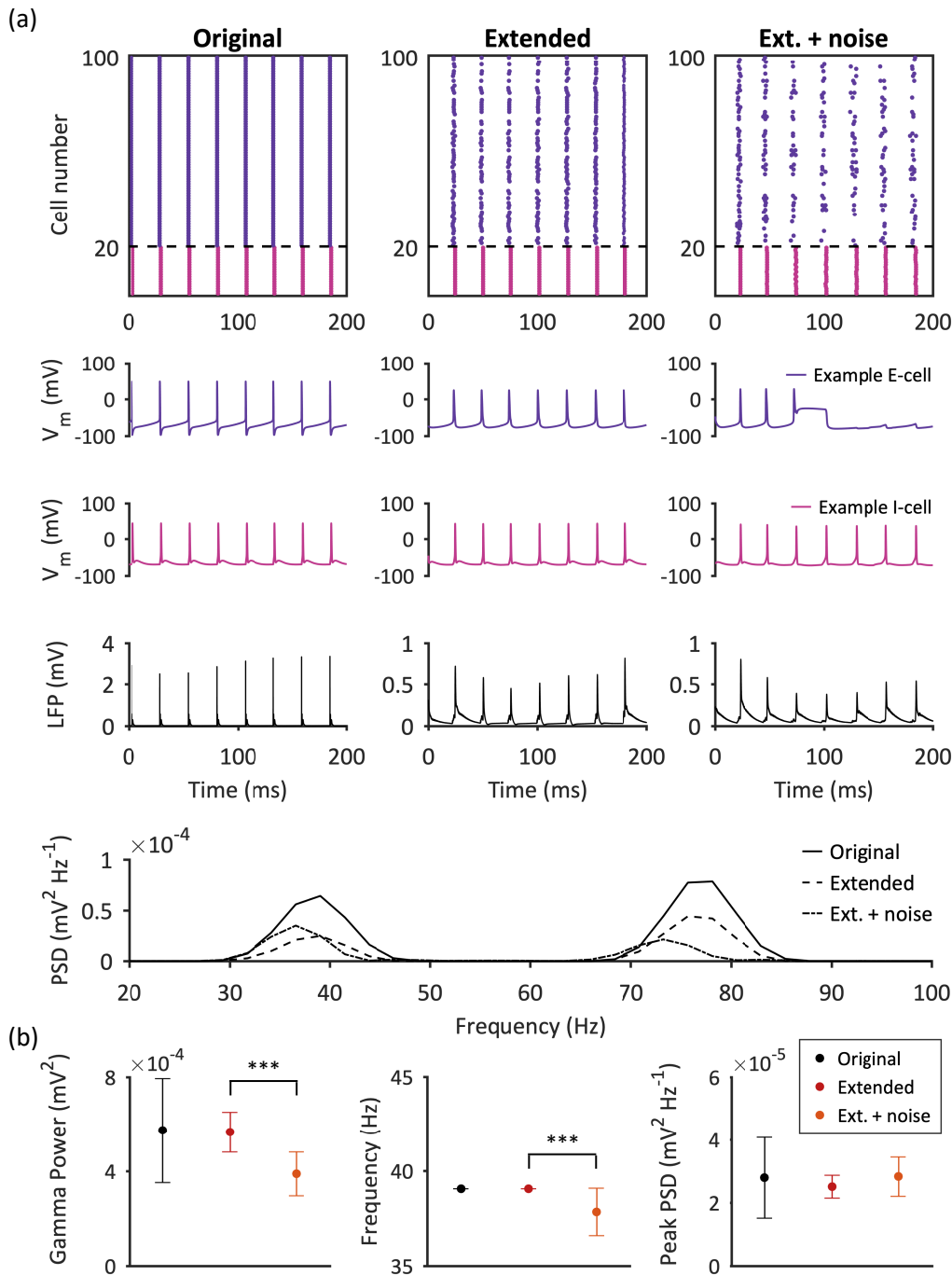


Figure 7.1 | Behaviour of the different EI network models. (a) Examples of the activity generated when a stimulation current is applied to the E-cells. Col. 1: Original network from Kopell et al. (2010) [135]. Col. 2: Extended network using an extended E-cell model fit to CA1 pyramidal neuron data. Col. 3: Extended network with external stochastic synaptic input. Row 1: raster plot (for 80 excitatory and 20 inhibitory cells); row 2: example E-cell activity; row 3: example I-cell activity; row 4: LFP; row 5: PSD. (b) Summary properties of the oscillations generated in each network. Left: power of the oscillations in the gamma frequency range; middle: fundamental frequency of the oscillations; right: PSD at the fundamental frequency.

Figure 7.1 (continued) The total gamma power and frequency of the oscillations were reduced when synaptic noise was added to the extended model (Student's t-test, *** $p < 0.001$). Means estimated by Monte Carlo simulations ($n = 20$), error bars indicate SD.

investigations into the robustness of the behaviour as heterogeneity is introduced to the synaptic strength distribution and to the cell populations. Combinations of these tests are also used later in the chapter to check the robustness of the results generated during the main investigations. Unless otherwise stated the total synaptic conductance between two populations (EI, II or IE) was held constant and was distributed uniformly across the synapses present.

1. **Network size** - Simulations were run for network sizes ranging from 10 to 2000 cells.
2. **Network connectivity** - The probability of a connection existing between two cells, p was varied from 0.25 to 1.
3. **Cell ratio** - The E:I cell ratio was varied from 20:80 to 95:5 in a network of 100 cells.
4. **Strength of stochastic synaptic input** - The conductance of the spontaneous synaptic transmission was varied from 0 to 0.2 mS/cm².
5. **Frequency of stochastic synaptic input** - The frequency of spontaneous synaptic transmission was varied from 5 to 40 Hz.
6. **Stimulation current strength** - The stimulation current strength was varied between 2.5 to 20 μ A/cm².
7. **Non-uniform synaptic strength distribution** - The synaptic strengths were drawn from five gaussian distributions where the coefficient of variation was varied from 0.1 to 0.5 and the mean total synaptic conductance between two populations were held at the original values (see Table C.2).
8. **Cell Heterogeneity** - The transient sodium channel conductance of the E-cell population was drawn from three gaussian distributions where the coefficient of variation was varied from 0.1 to 0.3 and the mean conductance was held at the original value of 48 mS cm².

The OAT tests were carried out on both the all-to-all connected network and in a sparsely-connected network ($p = 0.5$). Although a more thorough multi-factor sensitivity analysis

might reveal particular sensitivity to some parameter selections, the tests carried out (results described in the next section) do indicate that the gamma oscillations generated by the network are robust to biologically reasonable changes in the general network settings. The results of these robustness tests are presented and discussed in more detail below. In general, only the summaries of the results generated through the Monte Carlo simulations are shown (as in Figure 7.1b), except when there is a significant change in the oscillation properties and examples of the network activity help to clarify the underlying behaviour.

7.3.2 Robustness Test Results

Network construction

Test 1: Network size

The EI network used in the main simulations was constructed of 100 cells with 80 excitatory pyramidal neurons (E) and 20 inhibitory fast-spiking interneurons (I). This network size was chosen as at smaller sizes the oscillations generated were less stable and further increasing the network size did not significantly improve the performance of the network (Figure 7.2a) but was associated with a non-linear increase in computational cost (Figure 7.2b).

Test 2: Network connectivity

The network was constructed as a randomly generated graph where a link between two cells is determined by the probability of connectivity, p . In the main investigations the cells were connected all-to-all ($p = 1$) as this simplification did not substantially alter the network behaviour. The effect of increasing the probability of connectivity is shown in Figure 7.3. As mentioned previously, the total network strength was maintained in each simulation by proportionally decreasing the connection strengths as connections were added.

At low levels of network connectivity ($p = 0.25$) the entrainment of the cell firing was low (see the raster plot in Figure 7.3a), which was associated with a smaller LFP (row 2) and resulted in a larger variability in the frequency measured (Figure 7.3b:middle). As the network connectivity increased, the cell firing became more synchronised which increased the gamma power of the oscillations and lead to a decrease in the frequency as the stimulated E-cells became more entrained (Figure 7.3b). By $p = 0.75$ the power and frequency of the gamma oscillations generated had stabilised and further increasing the connectivity had no impact on the oscillations generated (see Figure 7.3b).

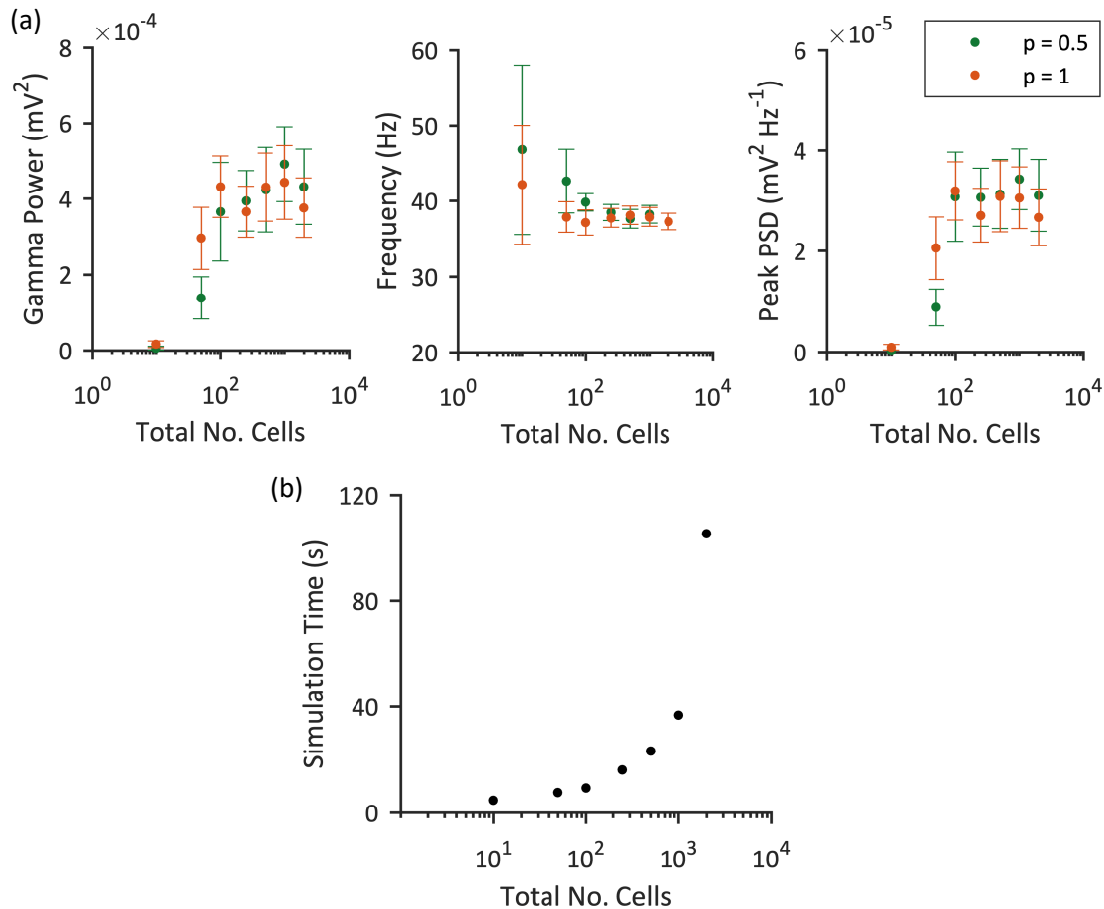


Figure 7.2 | The effect of increasing network size on network behaviour. The total number of cells (with a 4:1 E:I ratio) was varied from 10 to 2000 cells in the all-to-all ($p = 1$) and sparsely-connected ($p = 0.5$) EI networks. Number of cells are plotted on a logarithmic scale. (a) Summary properties of the oscillations generated in the two networks. As the network size increased, variability in the oscillation frequency reduced in both networks (middle), with less variability in the all-to-all network. At network sizes of ≥ 100 cells, the frequency plateaued as did the associated PSD (right) and the total gamma power (left) (calculated from LFP subset of 50 cells). Means estimated by Monte Carlo simulations ($n = 20$), error bars indicate SD. (b) The network simulation time increased non-linearly as the network size increased.

Test 3: Cell Ratio

The 4:1 ratio of E to I cells was assumed as this is an often used approximation for the ratio of glutamatergic to GABAergic neurons within the brain [23, 201]. The effect of altering the E:I cell ratio is shown in Figure 7.4 with little change in the behaviour of the all-to-all connected network in the biologically reasonable range of between 4:1 and 9:1 [185, 201]. Although less stable, gamma oscillations were still generated within this range in the sparsely-connected network, with a peak in the power of the oscillations at the lower ratio of 3:2 (Figure 3:left).

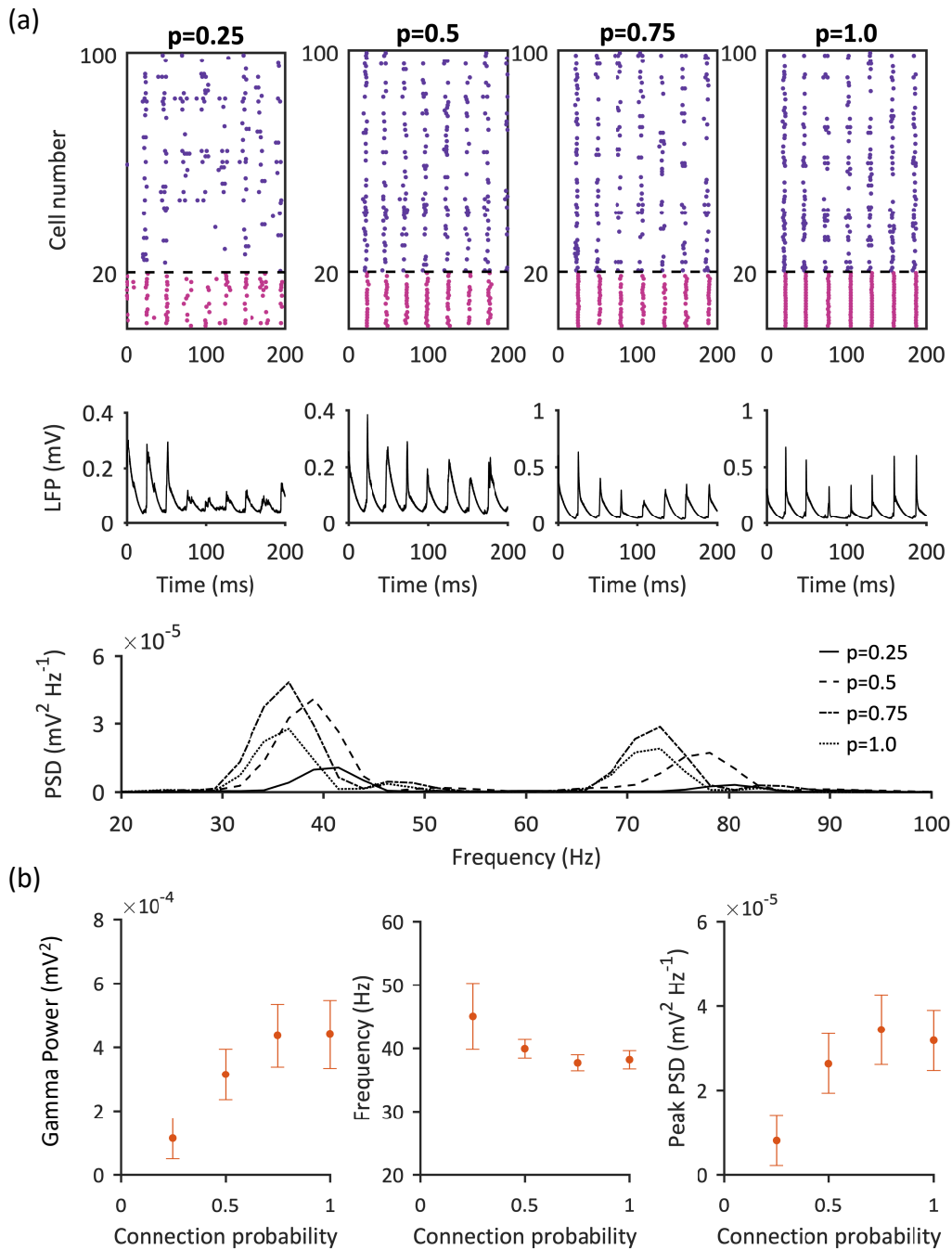


Figure 7.3 | The effect of increasing network connectivity on network behaviour.

The probability of a connection between two cells (p) in the network was increased from $p = 0.25$ to $p = 1$ whilst keeping the total synaptic conductance across the network constant. (a) Columns 1 - 4 show examples of the activity generated at $p = 0.25$, 0.5, 0.75 and 1. Row 1: raster plot (for 80 excitatory and 20 inhibitory cells); row 2: LFP; row 3: PSD. The coherence of the oscillations increased as the network became more connected; at $p = 0.25$ connectivity (col. 1) the cell activity was not fully synchronised but by $p = 0.5$ (col. 2) a clear gamma rhythm had emerged in the LFP.

Figure 7.3 (continued) (b) Summary properties of the oscillations generated. The larger frequency variability (middle) and low oscillation power (left) at $p = 0.25$ indicates low network coherence. The total gamma power of the oscillations (left) and the peak PSD (right) increased as connectivity increased, with the oscillation frequency stabilising at $p \geq 0.5$ (middle). Means estimated by Monte Carlo simulations ($n = 20$), error bars indicate SD.

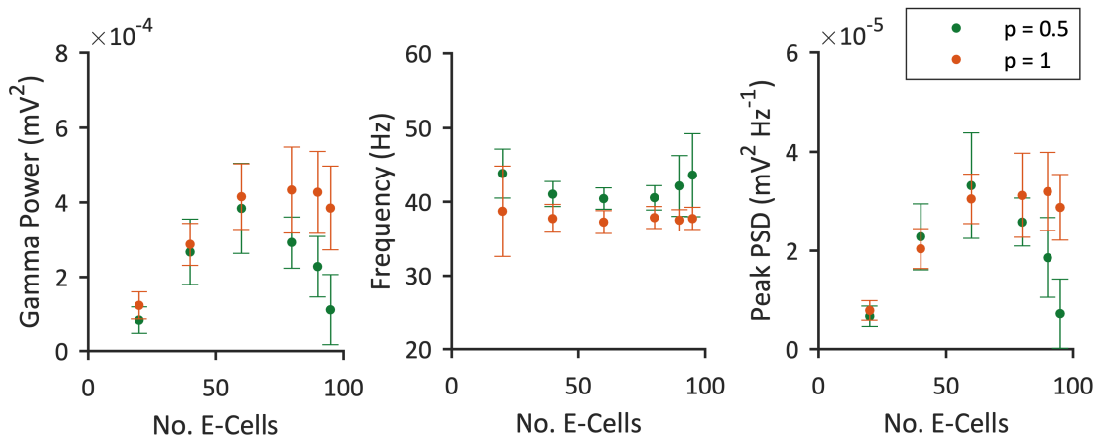


Figure 7.4 | The effect of altering the E:I cell ratio on network behaviour. Summary properties of the oscillations generated when the ratio of E:I cells was varied from 20:80 to 95:5 in the all-to-all ($p = 1$) and sparsely-connected ($p = 0.5$) EI networks. Results are plotted against the number of E-cells in the network, which was composed of 100 cells in total. Oscillations in the all-to-all connected network were comparable for E:I cell ratios between 60:40 and 90:10, with little variation in the mean gamma power (left), frequency (middle) or PSD at the fundamental frequency (right). In the sparsely connected network although frequency remained relatively consistent, the power of the oscillations peaked at 60:40 and deteriorated as the E:I cell ratio became more imbalanced. Means estimated by Monte Carlo simulations ($n = 20$), error bars indicate SD.

External Stimulation

Test 4: Noise Strength

The conductance of the synaptic noise (g_{noise}) input to the E and I-cells was set at 0.02 mS/cm^2 for the main simulations, which was the same order of magnitude as the single synaptic inputs within the network. The robustness of the model response to increasing the synaptic noise, at a frequency of 20Hz is shown in Figure 7.5. As the synaptic noise was strengthened, there was a significant decrease in the oscillation power accompanied by an increase in the frequency variability at $g_{\text{noise}} \geq 0.08 \text{ mS/cm}^2$ (see Figure 7.5a). This was the result of a loss of coherence in the oscillations, as shown in the illustrative raster plots in Figure 7.5b. The

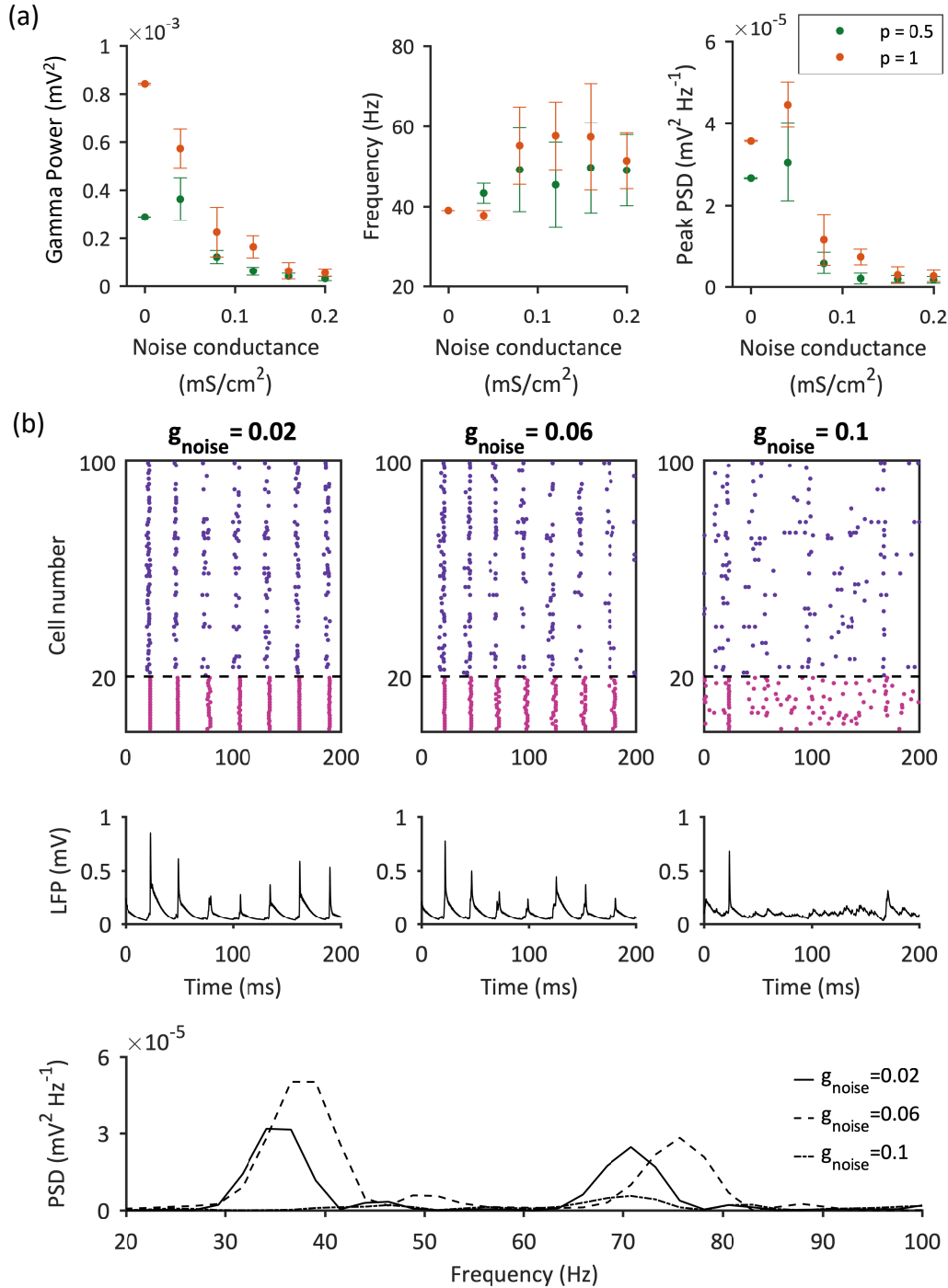


Figure 7.5 | The effect of increasing the synaptic noise strength on network behaviour. The conductance of the stochastic excitatory synaptic input (g_{noise}) was varied between 0 and 0.2 mS/cm² in the all-to-all ($p = 1$) and sparsely-connected ($p = 0.5$) EI networks. (a) Summary properties of the oscillations generated in the two networks. Overall, in both networks, there was an increase in the frequency (middle) but decrease in the gamma power (left) and PSD at the fundamental frequency (right) as noise increased, indicating a loss of coherence prior to oscillation break down at 0.1 mS/cm². Means estimated by Monte Carlo simulations ($n = 20$), error bars indicate SD.

Figure 7.5 (continued) (b) Examples of the activity generated in the all-to-all network at 0.02 mS/cm^2 , the level used in the main simulations (column 1), at 0.06 mS/cm^2 (column 2) and at 0.1 mS/cm^2 (column 3). Row 1: raster plot (for 80 excitatory and 20 inhibitory cells); row 2: LFP; row 3: PSD. As the noise increased the oscillation entrainment reduced and the frequency increased. By 0.1 mS/cm^2 the oscillations were lost with an associated drop in the PSD.

transition from gamma frequency oscillations to unsynchronised activity occurred between $g_{\text{noise}} = 0.06$ and 0.08 mS/cm^2 , which notably is close to the input threshold required to trigger a spike in the I-cell model ($\sim 0.06 \text{ mS/cm}^2$).

Test 5: Noise Frequency

The frequency of the synaptic noise, which was modelled as a poisson process, was set at 20Hz which falls within the range of activity measured in regions connected to the CA1 [45]. The sensitivity of the network behaviour to noise of frequencies between 5 and 40 Hz, at the noise strength used in the main simulations ($g_{\text{stoch},e} = g_{\text{stoch},i} = 0.02$), is shown in Figure 7.6. There was little variation in the gamma oscillations generated in either the sparse or fully connected network as the frequency was altered.

Test 6: Stimulation Current Strength

In the main simulations, the stimulation current that was applied to the E-cells to generate the gamma oscillations was set at $5 \mu\text{A/cm}^2$, which generated spiking in the pyramidal cells at a frequency of $\sim 100 \text{ Hz}$. The dependence of the network response on the stimulation current is shown in Figure 7.7. In the fully connected network, increasing the driving current increased both the power and frequency of the oscillations, which remained within the gamma range until the current surpassed $20 \mu\text{A/cm}^2$. However, the sparsely-connected network was much more sensitive to the increased drive and oscillations broke down at currents larger than $10 \mu\text{A/cm}^2$. Overall, this shows that the input current is important for determining the initial frequency of the oscillations.

Network Homogeneity

Overall the properties of the networks used in the main simulation were homogeneous; all cells in a population were the same and the synaptic strengths were uniformly distributed. In initial investigations on the dependence of the network behaviour on these simplifications, variability was added to the synapse strengths and cell properties to add heterogeneity to the network.

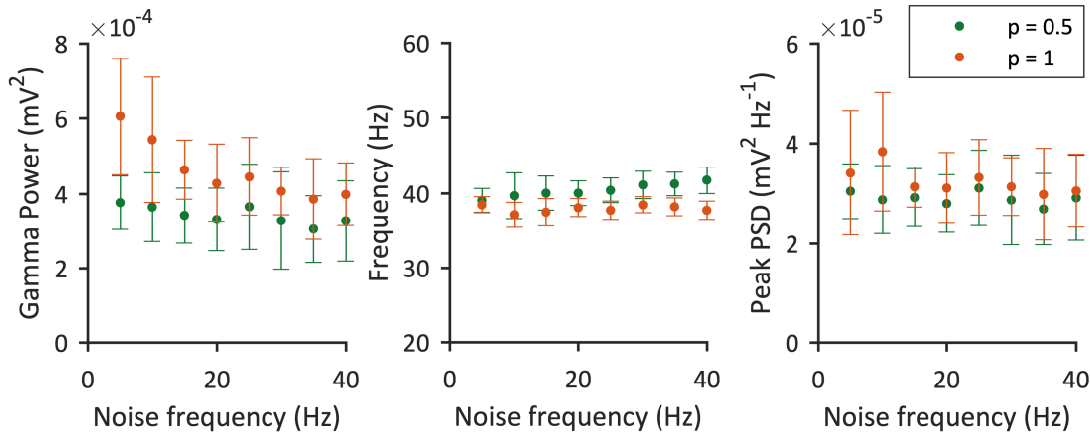


Figure 7.6 | The effect of increasing the synaptic noise frequency on network behaviour. Summary properties of the oscillations generated when the frequency of the stochastic excitatory synaptic input was varied between 5 and 40 Hz in the all-to-all ($p = 1$) and sparsely-connected ($p = 0.5$) EI networks. The gamma oscillations generated were generally consistent across the noise frequency range for both networks. There was little variation in the mean gamma power (left), frequency (middle) or PSD at the fundamental frequency (right), apart from a slight increase in the power and variability at ≤ 10 Hz in the all-to-all connected network. Means estimated by Monte Carlo simulations ($n = 20$), error bars indicate SD.

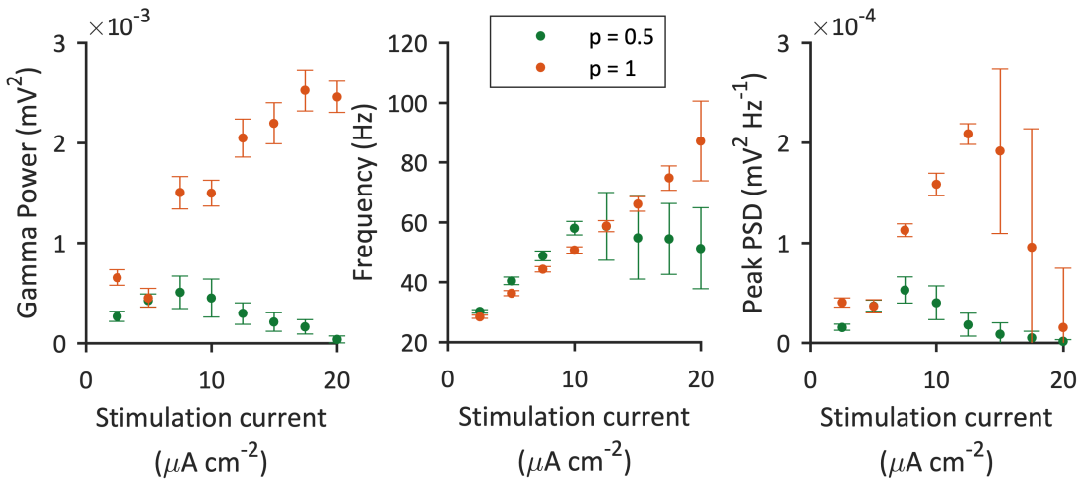


Figure 7.7 | The effect of altering the stimulation current on network behaviour. Summary properties of the oscillations generated when the excitatory stimulation current applied to the E-cells was varied between 2.5 and 20 $\mu\text{A/cm}^2$ in the all-to-all ($p = 1$) and sparsely-connected ($p = 0.5$) EI networks. The response in the two networks was significantly different. The gamma power of the oscillations (left) was consistently lower in the sparse network, where oscillations began to break down at 10 $\mu\text{A/cm}^2$, as indicated by the increasing frequency variability (middle) and decreasing PSD (right). In the all-to-all network the gamma power (left) and frequency (middle) of the oscillations increased with stimulation current. The high PSD variability at $\geq 16 \mu\text{A/cm}^2$ was a result of detection of other harmonics in the FFT. Means estimated by Monte Carlo simulations ($n = 20$), error bars indicate SD.

Test 7: Synaptic strength distribution

Synaptic connections were represented using a simple kinetic model developed by Ermentrout and Kopell [66]. In the main simulations the synaptic conductance was uniformly distributed across the connections present. To investigate how dependent the network response was on this simplification, simulations were also run with normally distributed synaptic strengths, with the total conductance across the network held constant as the coefficient of variation was increased. The results of these simulations are shown in Figure 7.8. There was little variation in the gamma oscillations generated in either the fully-connected or the sparsely-connected network when the range of synaptic strengths was increased, suggesting that the total strength of the excitatory and inhibitory conductances across the network is a more determinant factor.

Test 8: Cell homogeneity

As an initial step towards investigating how dependent the network behaviour was on homogeneous cell populations, simulations were run with variability incorporated into the pyramidal cell excitability. This was achieved by drawing the conductance of the E-cells' transient Na^+ -channels, g_{NaT} , from three Gaussian distributions with increasing deviation about the original mean value (48 mS/cm^2). The results, presented in Figure 7.9, show very little sensitivity to increasing the range of the E-cell excitability, which either suggests that the E-cell excitability is not a determining factor (which is unlikely) or that it is the population excitability that governs the response. The effect of cell heterogeneity could be much more extensively investigated by adding variability to other properties of the E-cell model and by adding similar heterogeneity to the I-cell population.

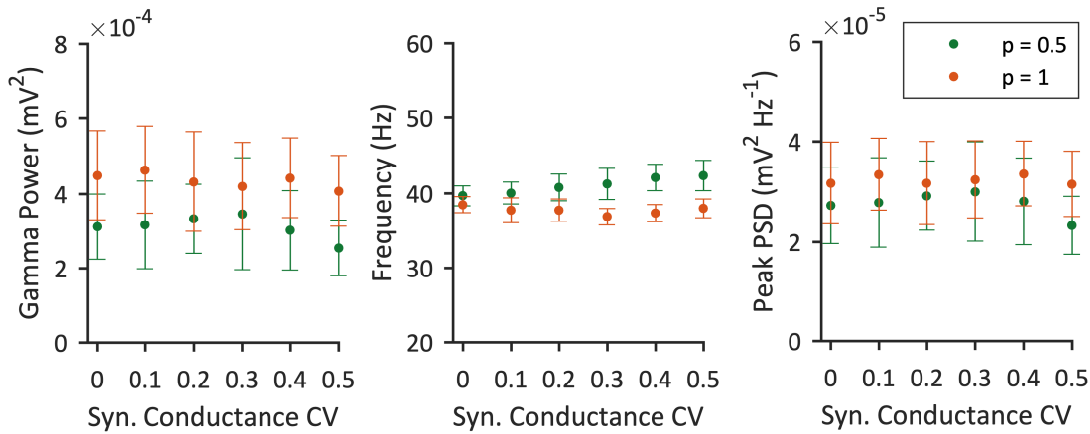


Figure 7.8 | The effect of altering the synaptic strength distribution on network behaviour. Summary properties of the oscillations generated in the all-to-all ($p = 1$) and sparsely-connected ($p = 0.5$) EI networks with synaptic conductances drawn from gaussian distributions of equal means but with increasing coefficients of variation (CV). Gamma frequency oscillations were maintained as synaptic strength variability was increased. There was little change in the mean gamma power (left), frequency (middle) or PSD at the fundamental frequency (right), apart from a slight increase in the frequency of the oscillations in the sparse network. Means estimated by Monte Carlo simulations ($n = 20$), error bars indicate SD.

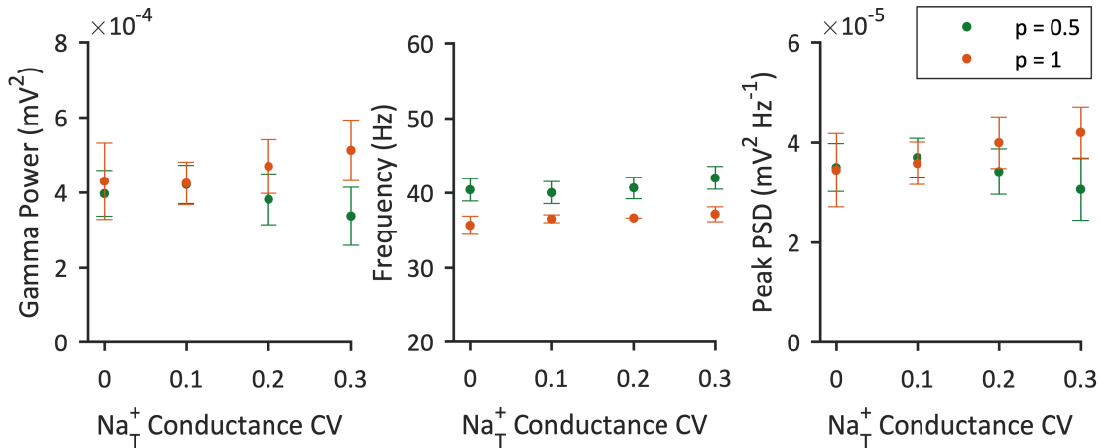


Figure 7.9 | The effect of adding heterogeneity to the E-cell population on network behaviour. Summary properties of the oscillations generated in the all-to-all ($p = 1$) and sparsely-connected ($p = 0.5$) EI networks when the voltage-gated Na_T channel conductance (g_{Na_T}) of each E-cell was drawn from gaussian distributions of equal means but with increasing coefficients of variation (CV). Gamma frequency oscillations were maintained in both networks as g_{Na_T} variability increased. The total gamma power (left) and PSD at the fundamental frequency (right) of the two networks diverged, but the frequency increased (≤ 5 Hz) in both cases (middle). Means estimated by Monte Carlo simulations ($n = 20$), error bars indicate SD.

7.4 Incorporating the Effects of $A\beta$

7.4.1 Altered Intrinsic Excitability

To investigate the impact of the altered PDAPP CA1 pyramidal cell properties on gamma generation, the fitted WT pyramidal neuron model was replaced with the fitted PDAPP CA1 pyramidal neuron model from Chapter 6. In comparison to the WT cells, the PDAPP-fitted cells had a reduced AP width and a faster firing rate during current injections as found experimentally [127]. Monte Carlo simulations were run on the base network (WT) and the PDAPP-type network (PDAPP) to compare the gamma activity generated. In Figure 7.10 the behaviour of the WT and PDAPP networks are compared. The gamma oscillations generated in the PDAPP network were significantly faster than the oscillations generated in the WT network but there was no statistically detectable difference in the total gamma power of the oscillations or the PSD at the fundamental frequency.

The same OAT tests as run on the WT model were run on the PDAPP network to investigate whether the difference in the response of the WT and PDAPP network was robust to changes in those network properties. Overall the increase in the frequency of the oscillations in the PDAPP model was a consistent result across all tests, whereas there was inconsistent evidence of a decrease in the power of the oscillations generated in the PDAPP model. In Figure 7.11 the results from those tests that are most pertinent to the changes in the E-cell parameters are presented. Specifically, the response to changes in the E:I cell ratio (Fig. 7.11a), the response to changes in the stimulation current applied to the E-cells (Fig. 7.11b) and the response when heterogeneity in the E-cell population is incorporated by drawing the Na_T conductances from a gaussian distribution (Fig. 7.11c). Of note is the divergence of the gamma power generated by the two models when heterogeneity was increased within the E-cell population and when the stimulation current was altered. However, as this was not evident in the main simulation or across the other tests, drawing any conclusions from this is not possible without further investigation.

Further simulations were run to compare the behaviour of the two networks when excitatory synaptic connections were removed as this is a characteristic feature of AD that is observed in the PDAPP-mouse model [41]. The response of the networks to a reduction of between 0 and 50% in the excitatory connections is shown in Figure 7.12. Interestingly the frequency of the oscillations generated in the PDAPP network were stable as synapses were removed whereas the frequency in the WT network, although slower throughout, increased as excitatory connections reduced. The peak PSD, measured at the fundamental frequency,

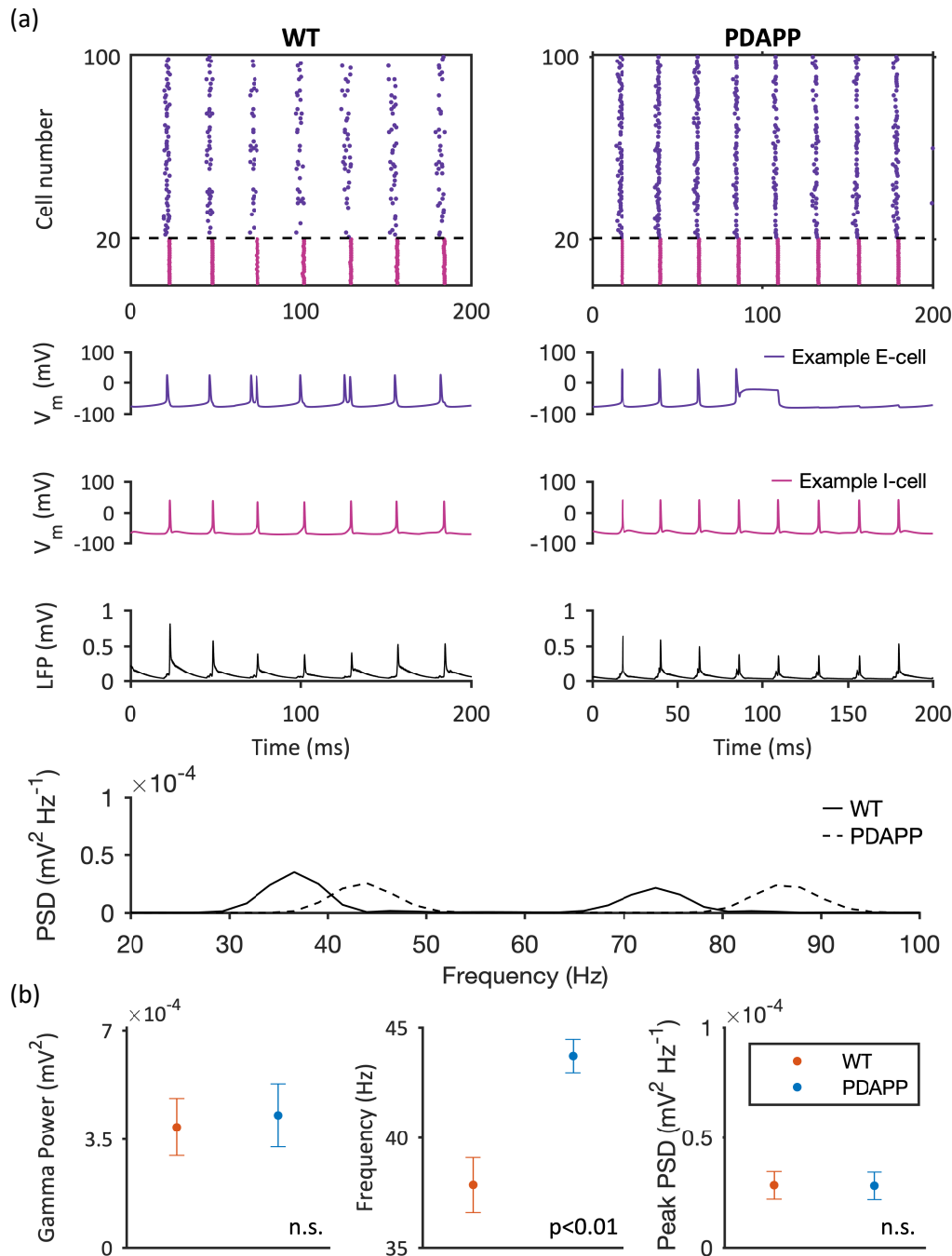


Figure 7.10 | Comparison of the gamma oscillations generated in the WT and PDAPP networks. The same stimulation current was used to drive gamma oscillations in two versions of the EI network, WT and PDAPP, where the E-cells were parameterised with data from CA1 pyramidal neurons in WT mice and PDAPP-transgenic mice respectively. (a) Examples of the activity generated in the WT (Column 1) and PDAPP network (Column 2). Row 1: raster plot (for 80 excitatory and 20 inhibitory cells); row 2: example E-cell activity; row 3: example I-cell activity; row 4: LFP; row 5: PSD. Firing frequency is visibly faster in the raster plot and PSD example from the PDAPP network simulations, as is a slight increase in the amplitude of the E-cell spikes. (b) Summary properties of the oscillations generated in each network. Left: power of the oscillations in the gamma frequency range; middle: fundamental frequency of the oscillations; right: PSD at the

Figure 7.10 (continued) fundamental frequency. There was no significant difference in the gamma power of the oscillations or the PSD at the fundamental frequency but there was a significant increase in the frequency of the oscillations in the PDAPP network ($p < 0.001$, Student's t-test). Means estimated by Monte Carlo simulations ($n = 20$), error bars indicate SD.

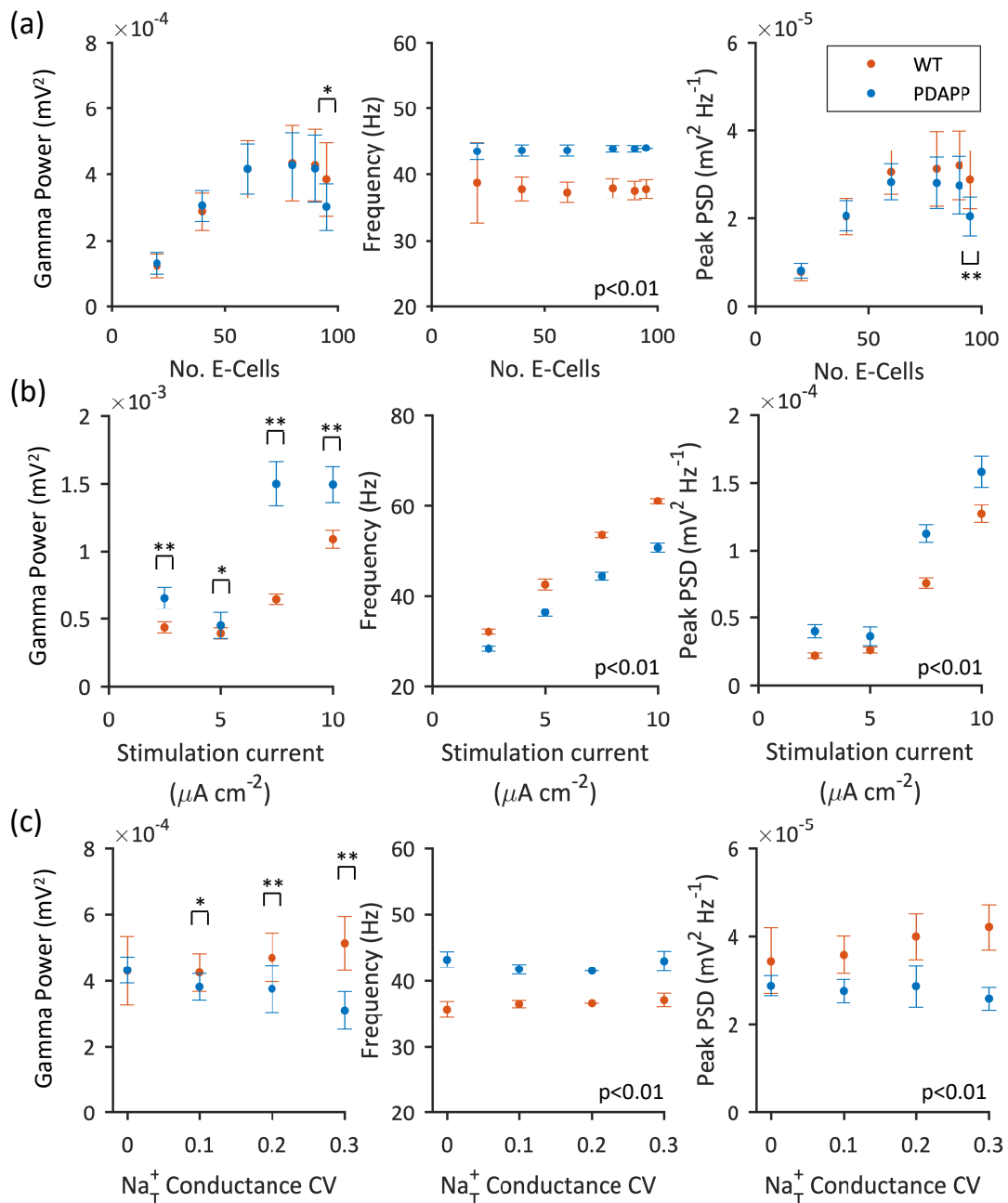


Figure 7.11 | The robustness of the PDAPP vs. WT network response to alterations in the network properties. Summary properties of the oscillations generated in the WT and PDAPP networks when the network construction was varied and heterogeneity was introduced to the models. (a) The ratio of E:I cells was varied from 20:80 to 95:5. (b) The stimulation current applied to the E-cells was varied from 2.5 to 10 $\mu\text{A}/\text{cm}^2$.

Figure 7.11 (continued) (c) The voltage-gated Na_T channel conductance (g_{Na_T}) of each E-cell was drawn from gaussian distributions of equal means but with increasing coefficients of variation (CV). Left: power of the oscillations in the gamma frequency range; middle: fundamental frequency of the oscillations; right: PSD at the fundamental frequency. The frequency of the oscillations were consistently faster in the PDAPP network but the gamma power and peak PSD of the oscillations were inconsistently lower. WT and PDAPP results compared using a Student's T-test (* $p < 0.05$; ** $p < 0.01$). Means estimated by Monte Carlo simulations ($n = 20$), error bars indicate SD.

indicated that the oscillations in the PDAPP network were lower than in the WT network as synapse loss increased. However, the total gamma power of the oscillations was not found to be statistically different in the two models.

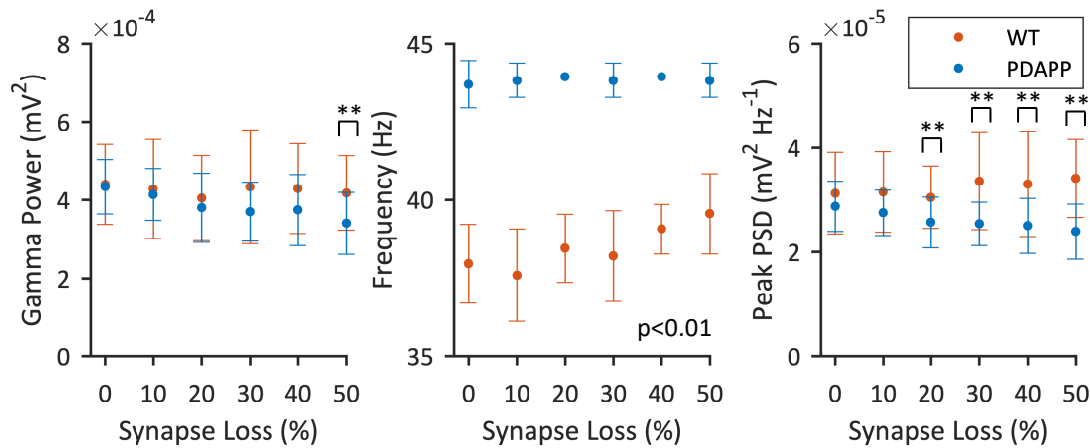


Figure 7.12 | The effect of excitatory synapse loss on the WT and PDAPP network behaviour. Summary properties of the oscillations generated in the WT and PDAPP networks when the number of excitatory synaptic connections were reduced by up to 50%. The total excitatory synaptic conductance across the network was kept constant. Left: power of the oscillations in the gamma frequency range; middle: fundamental frequency of the oscillations; right: PSD at the fundamental frequency. As synapse loss increased the oscillation frequency in the WT-network simulations increased but remained stable in the PDAPP network. The PSD at the fundamental frequency became significantly different in the two networks when synapse loss reached 20%. There was predominantly no change in the total gamma power of the oscillations. WT and PDAPP results compared using a Student's T-test (* $p < 0.05$; ** $p < 0.01$). Means estimated by Monte Carlo simulations ($n = 20$), error bars indicate SD.

7.4.2 Altered Synaptic Strength

In Chapter 5 it was suggested that the enhanced synaptic transmission at CA1 pyramidal neurons following acute A β treatment (results presented in Chapter 4) could be simulated in a simple kinetic model by increasing the synaptic conductance by 50%. The synaptic response, which is believed to be a post-synaptic AMPAR-mediated response [248], was associated with excitatory synapses in pyramidal neurons but it is conjectured here that A β could mediate the same effect at the excitatory AMPAR-mediated synapses of other cell-types. The confirmation or invalidation of this hypothesis requires further experimental investigation.

The impact of altering the excitatory synaptic conductance on the oscillations generated in the WT network, whilst keeping the other parameters fixed, is shown in Figure 7.13. Overall, strengthening the excitatory synaptic input to the I-cells increased the power of the oscillations and the PSD at the fundamental frequency but had little impact on the oscillation frequency at $g_{EI} > 0.6$ (see Figure 7.13a). As the example raster plot shows in Figure 7.13b, at $g_{EI} < 0.4$ the network behaviour was not synchronised, which explains the lower gamma power and high variability in the oscillation frequency at these levels. By $g_{EI} \geq 1$, the excitatory drive to the I-cells begins to evoke rapid spikes which is outside the desired network behaviour, that is that the cell firing is synchronised and occurs at gamma frequency or less, limiting the suitable range of conductances within this network set-up to $0.4 < g_{EI} < 1$.

To investigate how A β -induced enhanced transmission at excitatory post-synaptic synapses might impact on the generation of gamma frequency oscillations in the CA1 region, network simulations were run where the synaptic conductance of the excitatory E to I-cell synapses (g_{EI}) was increased by 50%. Figure 7.14 compares the behaviour of the original WT network with $g_{EI} = 0.5$ mS/cm² with the behaviour when $g_{EI} = 0.75$ mS/cm². With this parameter combination there was a significant increase in the gamma power, frequency and associated PSD of the oscillations. The monotonic increase in power as g_{EI} is strengthened (shown in Figure 7.13) suggests that the increase in the oscillation power was not dependent on the initial conductance parameterisation, although this does not mean that at other network settings this dependence could change. The frequency result is likely due to the fact that the oscillations were less stable at $g_{EI} = 0.5$ indicating this result is more dependent on the initial parameter selection.

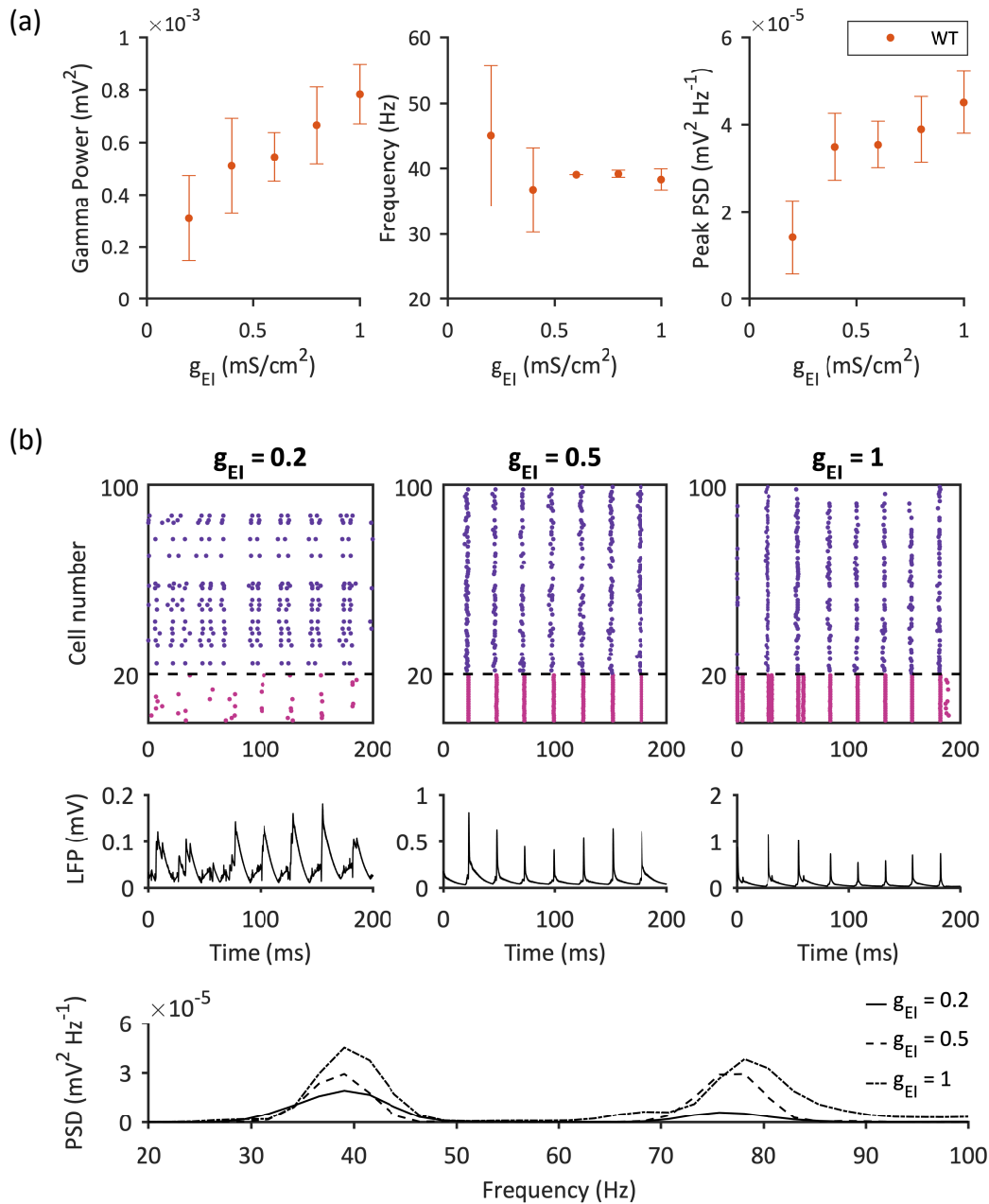


Figure 7.13 | The effect of altering the excitatory synaptic conductance on network behaviour. The excitatory synaptic conductance (g_{EI}) was strengthened from 0.2 to 2 mS/cm² in the WT network. (a) Summary properties of the oscillations generated. Left: power of the oscillations in the gamma frequency range; middle: fundamental frequency of the oscillations; right: PSD at the fundamental frequency. The gamma power and peak PSD increased as g_{EI} increased. The frequency stabilised at $g_{EI} > 0.4$ mS/cm². Results analysed using one-way ANOVA (* $p < 0.05$; ** $p < 0.01$). Means estimated by Monte Carlo simulations ($n = 20$), error bars indicate SD. (b) Columns 1 - 3 show examples of the activity generated at $g_{EI} = 0.2$, 0.5 (the strength used in the main simulations) and 1 mS/cm². Row 1: raster plot (for 80 excitatory and 20 inhibitory cells); row 2: LFP; row 3: PSD. When g_{EI} was too low network activity was not coherent (col. 1). By $g_{EI} = 1$ mS/cm² the I-cells began to produce pairs of rapid spikes (see raster plot).

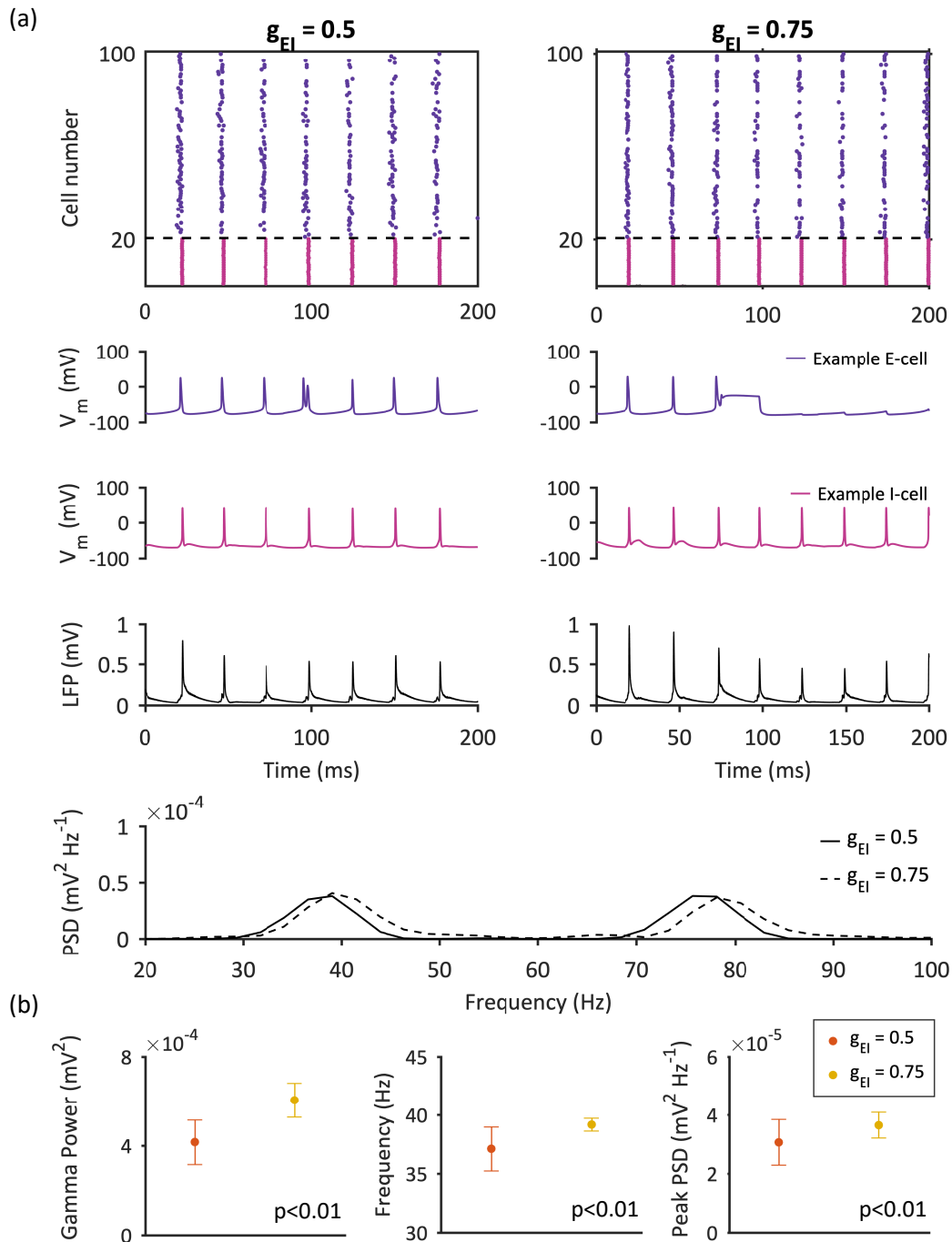


Figure 7.14 | Comparison of the gamma oscillations generated when the excitatory synaptic conductance is increased by 50%. Gamma oscillations were generated in the WT network with the excitatory synaptic conductance (g_{EI}) at 0.5 and 0.75 mS/cm^2 , the original network value and the 50% increase suggested from acute $A\beta$ -treatment data. (a) Examples of the activity generated in the WT network with $g_{EI} = 0.5$ (Column 1) and $g_{EI} = 0.75$ (Column 2). Row 1: raster plot (for 80 excitatory and 20 inhibitory cells); row 2: example E-cell activity; row 3: example I-cell activity; row 4: LFP; row 5: PSD. (b) Summary properties of the oscillations generated in each network version. Left: power of the oscillations in the gamma frequency range; middle: fundamental frequency of the oscillations; right: PSD at the fundamental frequency.

Figure 7.14 (continued) There was a significant increase in all three measures of the simulated gamma oscillations when the excitatory synaptic conductance to the I-cells was increased. Results compared using a Student's T-test. Means estimated by Monte Carlo simulations (n = 20), error bars indicate SD.

The same OAT tests as run on the original WT model were run when g_{EI} was increased by 50% to investigate whether the change in the oscillations were robust to changes in those network properties. Overall the increase in the gamma power at increased g_{EI} was consistent across all tests whereas there was inconsistent evidence of an increase in the oscillation frequency and the associated peak PSD. In Figure 7.15, the results from those tests that are most pertinent to the changes in the synapse parameters are presented. Specifically, the response to changes in the E:I cell ratio (Fig. 7.15a), the response to changes in the probability of a synaptic connection (Fig. 7.15b) and the response when heterogeneity is introduced to the synaptic strengths by drawing the conductances from a gaussian distribution (Fig 7.15c). In these examples the frequency was generally higher when the excitatory conductance was strengthened but as previously stated, this result is dependent on the initial parameter selection even within this network set-up.

So far the network behaviour has been investigated when all of the excitatory synapses have been increased simultaneously. However, given that the enhanced synaptic transmission was measured following acute A β treatment and that it is unlikely that all cells would simultaneously be exposed to pathogenic A β -levels, it is interesting to consider what fraction of the cells have to be affected to produce changes in the oscillations. The result of progressively increasing the fraction of affected cells, which have a 50% increase in the conductance of their excitatory synapses, is shown in Figure 7.16. There was a progressive increase in the gamma power of the oscillations as the fraction of affected synapses was increased. There was also a small statistically significant increase in the oscillation frequency when only 25% of the network was affected but no subsequent change in the frequency as more synapses were affected. There was no significant variation measured in the PSD at the fundamental frequency (as measured with one-way ANOVA and post-hoc unpaired students t-tests).

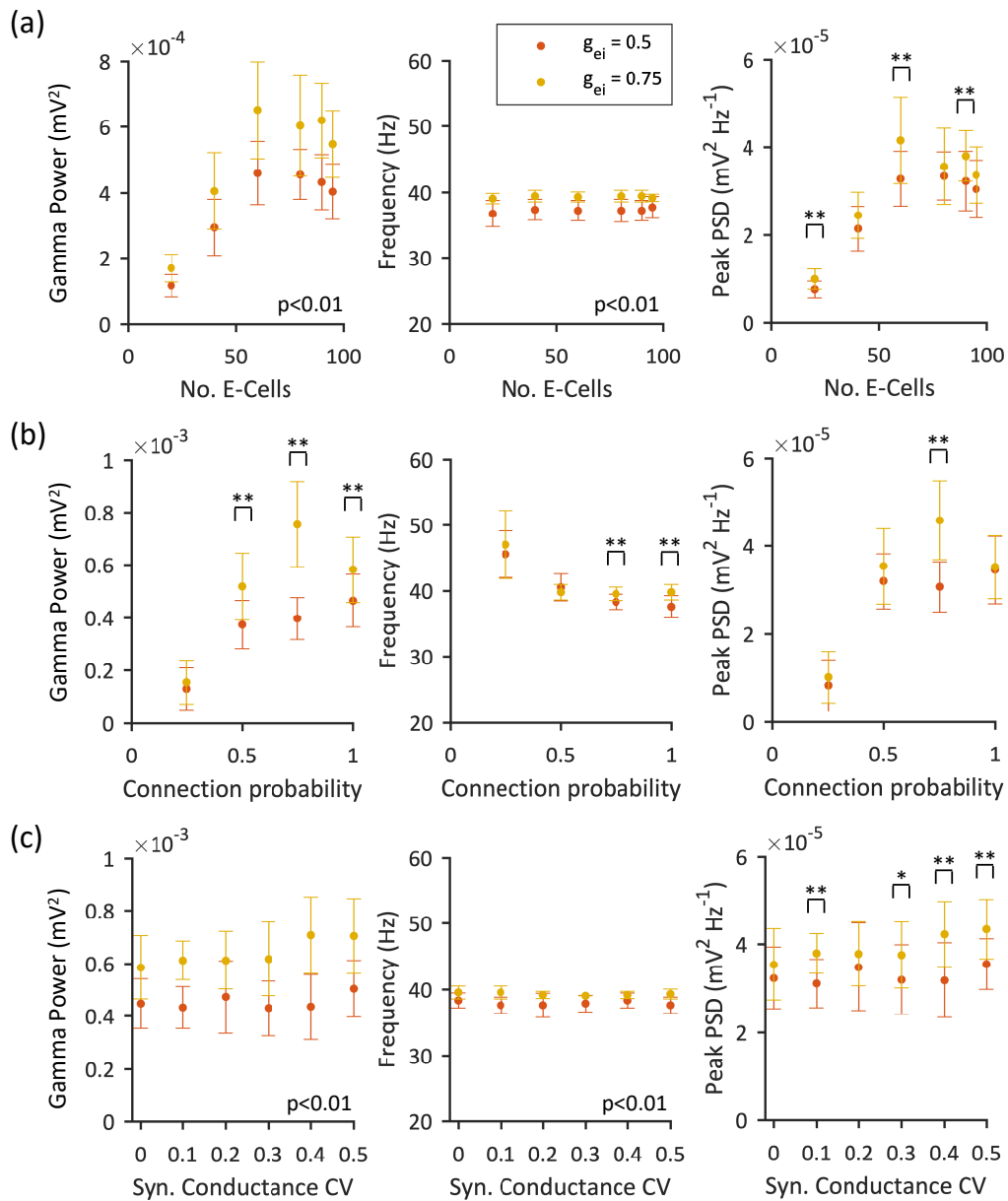


Figure 7.15 | Testing the robustness of the network response to increased excitatory synaptic conductance. Summary properties of the oscillations generated in the WT network with $g_{EI} = 0.5$ and $g_{EI} = 0.75$ mS/cm² when: (a) the ratio of E:I cells was varied from 20:80 to 95:5 (results are plotted against the number of E-cells in the network, which was composed of 100 cells in total); (b) the probability of a connection between two cells was increased from 0.25 to 1 whilst keeping the total synaptic conductance across the network constant; (c) the synaptic conductances were drawn from gaussian distributions of equal means but with increasing coefficients of variation (CV). Left: power of the oscillations in the gamma frequency range; middle: fundamental frequency of the oscillations; right: PSD at the fundamental frequency. The increase in the total power and frequency of the oscillations at $g_{EI} = 0.75$ mS/cm² was insensitive to changes

Figure 7.15 (continued) in cell ratio or synaptic heterogeneity and was maintained at connectivity levels $>50\%$. The effect on peak PSD was inconsistent across all tests. Results compared using a Student's T-test ($*p<0.05$; $**p<0.01$). Means estimated by Monte Carlo simulations ($n = 20$), error bars indicate SD.

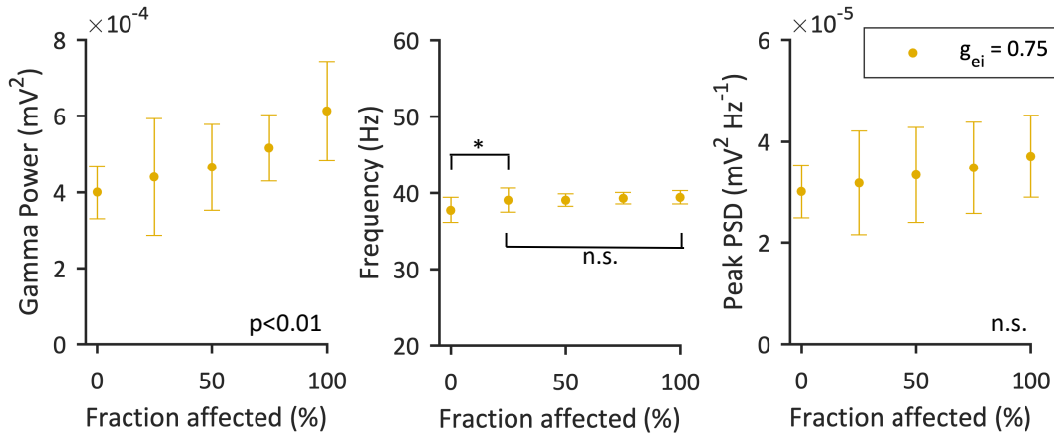


Figure 7.16 | The effect of altering the fraction of strengthened excitatory synapses on network behaviour. Summary properties of the oscillations generated in the WT network when the fraction of excitatory synapses strengthened from $g_{EI} = 0.5$ to $g_{EI} = 0.75 \text{ mS/cm}^2$, is increased from 0 to 100%. Left: power of the oscillations in the gamma frequency range; middle: fundamental frequency of the oscillations; right: PSD at the fundamental frequency. Increasing the fraction of strengthened synapses increased the gamma power and caused a small increase in the oscillation frequency, which then remained stable, when 25% were affected. There was no change in the associated peak PSD. Results analysed using one-way ANOVA ($*p<0.05$; $**p<0.01$). Means estimated by Monte Carlo simulations ($n = 20$), error bars indicate SD.

7.5 Discussion

The well-established EI network model was improved by adding the more detailed data-informed CA1 neuron model and then used to simulate gamma frequency oscillations. It was found that the 50% increase in the fast-excitatory synaptic conductance resulted in a statistically significant increase in the total gamma power of the oscillations across all tests. There was inconsistent evidence of an increase in the frequency of the oscillations.

The incorporation of the fitted PDAPP neuron into the network robustly increased the frequency of the gamma oscillations. Given that gamma oscillations have an important role in memory function it would be interesting to further investigate if this increase in gamma frequency could alter the theta-nested gamma in an E-I-O network (where O-cells are oriens lacunosum-moleculare (O-LM) cells) [135].

DISCUSSION

The use of computational modelling tools alongside experimental work is essential for furthering understanding of the complex processes that underlie Alzheimer's Disease. In this thesis, multiscale biophysical models informed by experimental observations were used to further investigate the functional impact of A β over-expression, one of the key areas of interest in AD research. Enhanced levels of A β have been associated with synaptic dysfunction, altered neuronal intrinsic excitability and altered gamma frequency activity within the CA1 region of the hippocampus, a focal point of AD-related neurodegeneration. By using a combination of synapse, cellular and network level models it was possible to investigate both the cause and functional consequence of experimentally-observed A β -related changes in synaptic and cellular level activity in CA1 pyramidal neurons.

In Chapters 4 and 5 electrophysiology experiments and computational modelling were used to probe the acute effect of amyloid-beta on synaptic transmission. Miniature EPSC recordings in CA1 neurons following acute intracellular A β -treatment showed a rapid increase in the strength of AMPAR-mediated synaptic transmission, corroborating previous results [248]. As mEPSCs reflect quantal transmission they are well-suited to modelling. A kinetic synapse model was then fit to the mEPSCs data to quantify what synaptic changes could account for the increased transmission. It was found that increasing the synaptic conductance of the model by 50% could account for the increase in the mEPSC amplitude distribution. In Chapter 7, by incorporating this synaptic result in a well-established E-I network model that generates gamma frequency activity, it was shown that this increased the

total gamma power of the oscillations with no significant change in the gamma oscillation frequency.

An important avenue of investigation following on from this work is to consider the impact of calcium-permeable AMPAR (CP-AMPA) expression, as it was suggested that they underlie the increase in synaptic transmission. Given the importance of Ca^+ dysregulation in AD pathology, it would be of interest to investigate how an increase in the calcium permeability of the cell membrane could impact the synapse, cell and network level behaviour (discussed in more detail in Section 5.3).

In Chapter 5 a single-compartment pyramidal neuron model was used to suggest what sub-cellular alterations may underlie the altered excitability of CA1 pyramidal neurons from a PDAPP transgenic mouse model which over-express $\text{A}\beta$. The model was parameterised using the data and then extended to include a second transient sodium channel to make the model more biologically realistic. It was found that the altered excitability properties could be achieved by altering the ion channel conductances of the Na_T and K_{DR} channel and the kinetics of the K_{DR} channel, in line with other experimental observations [29, 228]. By incorporating the PDAPP-fitted pyramidal neuron model in an E-I network model in Chapter 7, it was shown that the changes in the intrinsic excitability of the PDAPP neuron caused a robust increase in the gamma oscillation frequency in the PDAPP network.

The next step in this work is to fit similar single-compartment neuronal models to the excitability data recorded in CA1 oriens lacunosum-moleculare (O-LM) cells and fast-spiking interneurons from PDAPP mice (currently unpublished data). The preliminary stages of this work have already begun. The aim is to then incorporate these fitted cell models into an E-I-O network model that is capable of generating theta-nested gamma, which is also functionally important in memory processing in the hippocampus. Using this model it would be possible to investigate how the altered excitability of the different cell types contributes to network-level dysfunction or if the changes occur in order to maintain network level activity homeostasis.

Overall, in this thesis models have been used to investigate cross-scale impacts of $\text{A}\beta$, at a single synapse to the activity across one hundred synaptically connected cells. By using the models, more information was gleaned from the data than was possible experimentally. When addressing a disorder as complex as AD it is important to use all tools available. Mathematical models are ideal for the study of complex systems; their use in a multidisciplinary approach is essential for driving forward understanding of AD pathology.



APPENDIX A

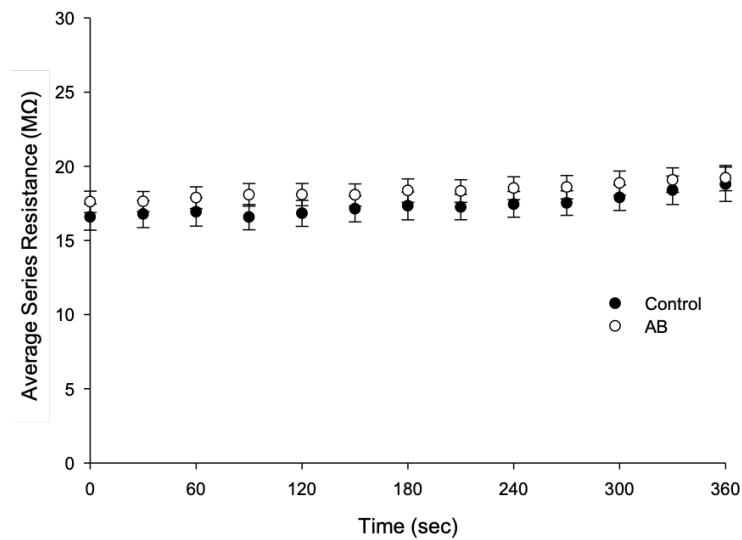


Figure A.1 | The average seal resistance recorded during the mEPSC experiments. Throughout the mEPSC recordings the integrity of the patch was monitored. The plot shows the average seal resistance measured during the control and A β -treated mEPSC recordings. Only experiments with a series resistance (R_s) below 20 M Ω and less than 10% variability in R_s throughout the experiment were used.

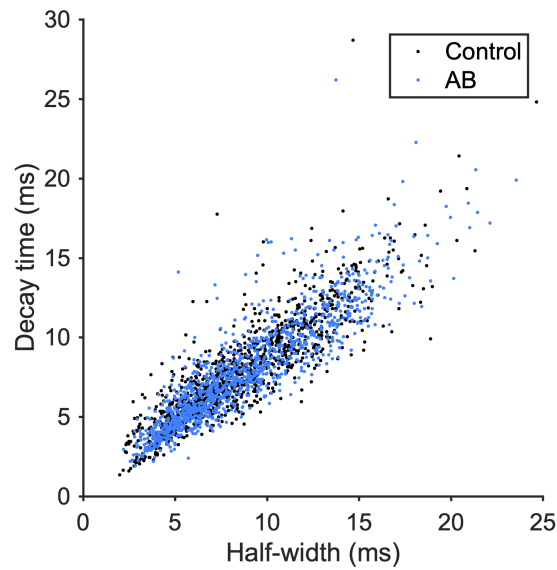


Figure A.2 | mEPSC half-width and decay time correlation. The mEPSC half-width and decay times were highly correlated ($R = 0.9$) with the same correlation in both the control and $A\beta$ -treated cells, therefore when carrying out correlation analysis and in the model we focused on the decay time.

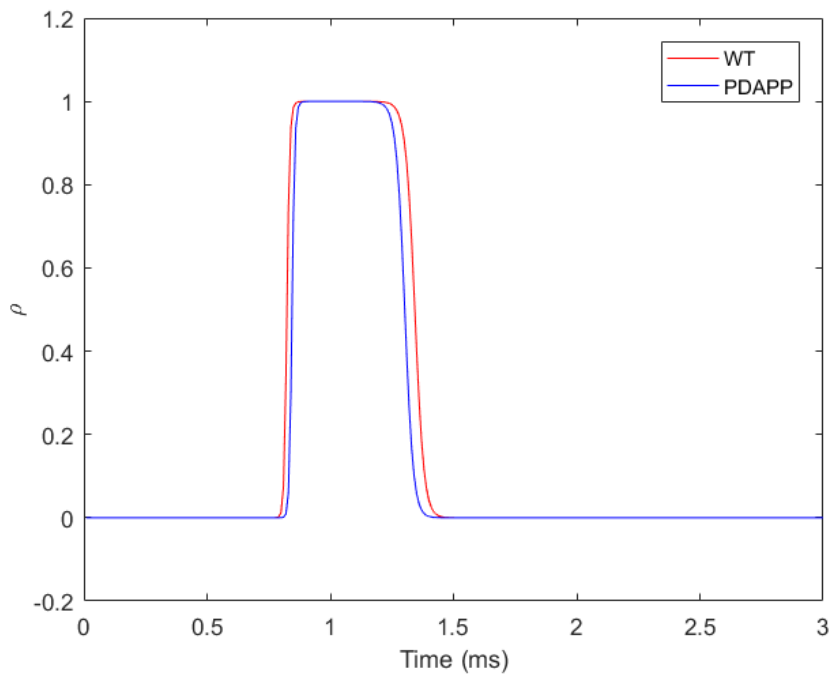


Figure A.3 | Network model neurotransmitter release. The neurotransmitter pulse generated by a pre-synaptic AP in the network model.

APPENDIX B

The Gradient Descent Method

The gradient descent method, also known as the method of steepest descent, is an optimisation algorithm that finds the nearest local minima (x_{\min}) of a given function ($f(x)$) using the gradient of the function ($f'(x)$). Starting from an initial parameter (x_0), the minima is reached by iteratively taking steps ($x_0 \rightarrow x_1$, $x_1 \rightarrow x_2$ etc.) in the negative (downhill) direction of the functions gradient (so $f(x_1) < f(x_0)$, $f(x_2) < f(x_1)$ and so on) until a fixed point (within some tolerance level ϵ) is reached. On each iteration the parameter value is updated using the following form:

$$x_i = x_{i-1} - \alpha f'(x_{i-1}) \quad (\text{B.1})$$

where the size of each step is determined by the learning rate, α , and the gradient of the function.

The example above is of a function with a single variable but the gradient descent method can also be used to find the local minima of a function with multiple variables (e.g. $f(x, y, z)$). In this case the partial derivatives of the function are calculated simultaneously to produce a gradient vector that is used to update the variables in the next iteration. On each iteration the following calculations are used to update the parameter values.

$$x_i = x_{i-1} - \alpha f'_x(x_{i-1}, y_{i-1}, z_{i-1}) \quad (\text{B.2})$$

$$y_i = y_{i-1} - \alpha f'_y(x_{i-1}, y_{i-1}, z_{i-1}) \quad (\text{B.3})$$

$$z_i = z_{i-1} - \alpha f'_z(x_{i-1}, y_{i-1}, z_{i-1}) \quad (\text{B.4})$$

To ensure that the gradient descent algorithm converges within a reasonable time it is important that the learning rate is set to an appropriate value. If the iteration steps are too large they can overshoot the minima and potentially diverge, whereas if they are too small a very large number of steps may be necessary to reach convergence. The performance of the algorithm is also improved when the parameter values are roughly within the same range. A rule of thumb is to scale the parameters $(\theta_1, \theta_2 \dots \theta_n)$ so that $-1 \geq \theta_{1\dots n} \geq 1$.

Model fitting using the gradient descent method

The gradient descent method can be used to optimise the fit of a predefined model to a data set. The aim is to identify the parameter selection that provides the best fit to the data. To achieve this the gradient descent algorithm is used to minimise a cost function J , which is a measure of the goodness of fit of the model to the data. The value of the cost function is dependent on the parameter values used in the model $J(\theta_{1\dots n})$.

In our case we used least squares regression to fit the synapse model to the mEPSC traces. In this approach the aim is to minimise the mean squared error (MSE), therefore the MSE was used as the cost function in the gradient descent algorithm.

$$J(\theta_{1\dots n}) = \frac{1}{m} \sum_{i=1}^m (Y^i - \hat{Y}^i)^2 \quad (\text{B.5})$$

where Y^i is the model output and \hat{Y}^i the expected value from the data.

There are many different optimisation algorithms that can be used for data fitting, with the gradient descent method being one of the more simple approaches. In comparison to the more sophisticated optimisation algorithms (e.g. conjugate gradient descent or BFGS algorithms) the gradient descent method is slower to converge, requiring more iterations. However, for our purposes the computational speed of gradient descent was acceptable, with a single trace fitting taking less than 1 minute. A more pertinent limitation of the gradient descent method is that it only finds the nearest local minima, which is not necessarily the global minimum of the function. However, as we based our initial starting parameters on pre-established biological measurements and the purpose was not to produce accurate measurements of synaptic properties, this was not considered to be a significant problem and consequently the gradient descent method was deemed sufficient for the purpose of this work.

APPENDIX C

Table C.1: Initial AMPAR parameters fitted to CA3 EPSCs from [61]

Property	Variable	Unit	Value
Reversal Potential	E	mV	0
Max. Transmitter Concentration	C_T	mM	1
Transmitter Pulse Duration	t_x	ms	1
Conductance	g	mS/cm ²	1
Binding Rate	α	ms ⁻¹ mM ⁻¹	1.1
Unbinding Rate	β	ms ⁻¹	0.19

Table C.2: EI Network properties. Parameters generally match those in [135] with altered parameters written in bold.

Property	Variable	Unit	Value
Number of E-cells	N_E	-	80
Number of I-cells	N_I	-	20
Connection probability	p	-	1
Total E-I synaptic conductance	g_{EI}	mS/cm ²	2.8
Total I-I synaptic conductance	g_{II}	mS/cm ²	0.5
Total I-E synaptic conductance	g_{IE}	mS/cm ²	0.5
Stimulation Current	I_{det}	μ A/cm ²	5
Stochastic synaptic conductance	g_{stoch}	mS/cm ²	0.02
Stochastic synaptic frequency	f_{stoch}	Hz	20
Stochastic synaptic decay time	$\tau_{stoch,E}$	ms ⁻¹	3

BIBLIOGRAPHY

- [1] E. ABRAMOV, I. DOLEV, H. FOGEL, G. D. CICCOTOSTO, E. RUFF, AND I. SLUTSKY, *Amyloid- β as a positive endogenous regulator of release probability at hippocampal synapses.*, *Nature Neuroscience*, 12 (2009), pp. 1567–1576.
- [2] T. AKAM, I. OREN, L. MANTOAN, E. FERENCZI, AND D. M. KULLMANN, *Oscillatory dynamics in the hippocampus support dentate gyrus-CA3 coupling*, *Nature Neuroscience*, 15 (2012), pp. 763–768.
- [3] ALZHEIMER’S ASSOCIATION, *2017 Alzheimer’s Disease Facts and Figures*, *Alzheimer’s Dementia*, 13 (2017), pp. 325–373.
- [4] P. ANDERSEN, *Organization of Hippocampal Neurons and Their Interconnections*, in *The Hippocampus*, R. Isaacson and K. Pribram, eds., Springer, 1975, pp. 155–175.
- [5] B. K. ANDRÁSFALVY, J. K. MAKARA, D. JOHNSTON, AND J. C. MAGEE, *Altered synaptic and non-synaptic properties of CA1 pyramidal neurons in Kv4.2 knockout mice.*, *The Journal of Physiology*, 586 (2008), pp. 3881–3892.
- [6] P. ANDREWS, H. BOKIL, S. KAUR, C. LOADER, H. MANIAR, S. MEHTA, P. MITRA, H. NALATORE, R. YADAV, AND R. SHUKLA, *Chronux Toolbox*, 2008.
- [7] M. ARBEL-ORNATH, E. HUDRY, J. R. BOIVIN, T. HASHIMOTO, S. TAKEDA, K. V. KUCHIBHOTLA, S. HOU, C. R. LATTARULO, A. M. BELCHER, N. SHAKERDGE, P. B. TRUJILLO, A. MUZIKANSKY, R. A. BETENSKY, B. T. HYMAN, AND B. J. BACSKAI, *Soluble oligomeric amyloid- β induces calcium dyshomeostasis that precedes synapse loss in the living mouse brain*, *Molecular Neurodegeneration*, 12 (2017), pp. 1–14.
- [8] P. V. ARRIAGADA, J. H. GROWDON, E. T. HEDLEY-WHYTE, AND B. T. HYMAN, *Neurofibrillary tangles but not senile plaques parallel duration and severity of Alzheimer’s disease*, *Neurology*, 42 (1992), p. 631.

BIBLIOGRAPHY

- [9] M. C. ASHBY, M. I. DAW, AND J. T. ISAAC, *AMPA Receptors*, in *The Glutamate Receptors*, R. Gereau and G. Swanson, eds., Humana Press, Totowa, NJ, 2008, pp. 1–44.
- [10] D. ATASOY, M. ERTUNC, K. L. MOULDER, J. BLACKWELL, C. CHUNG, J. SU, AND E. T. KAVALALI, *Spontaneous and evoked glutamate release activates two populations of NMDA receptors with limited overlap*, *Journal of Neuroscience*, 28 (2008), pp. 10151–10166.
- [11] L. A. ATHERTON, D. DUPRET, AND J. R. MELLOR, *Memory trace replay: The shaping of memory consolidation by neuromodulation*, *Trends in Neurosciences*, 38 (2015), pp. 560–570.
- [12] D. E. BARNES AND K. YAFFE, *The projected effect of risk factor reduction on Alzheimer's disease prevalence*, *The Lancet Neurology*, 10 (2011), pp. 819–828.
- [13] R. J. BATEMAN, P. S. AISEN, B. DE STROOPER, N. C. FOX, C. A. LEMERE, J. M. RINGMAN, S. SALLOWAY, R. A. SPERLING, M. WINDISCH, AND C. XIONG, *Autosomal-dominant Alzheimer's disease: A review and proposal for the prevention of Alzheimer's disease*, *Alzheimer's Research and Therapy*, 1 (2011).
- [14] T. A. BAYER AND O. WIRTHS, *Intracellular accumulation of amyloid-beta - A predictor for synaptic dysfunction and neuron loss in Alzheimer's disease*, *Frontiers in Aging Neuroscience*, 2 (2010), pp. 1–10.
- [15] C. BÉDARD, S. RODRIGUES, N. ROY, D. CONTRERAS, AND A. DESTEXHE, *Evidence for frequency-dependent extracellular impedance from the transfer function between extracellular and intracellular potentials*, *Journal of Computational Neuroscience*, 29 (2010), pp. 389–403.
- [16] R. T. BETTERTON, L. M. BROAD, K. TSANEVA-ATANASOVA, AND J. R. MELLOR, *Acetylcholine modulates gamma frequency oscillations in the hippocampus by activation of muscarinic M1 receptors*, *European Journal of Neuroscience*, 45 (2017), pp. 1570–1585.
- [17] T. BILOUSOVA, C. A. MILLER, W. W. POON, H. V. VINTERS, M. CORRADA, C. KAWAS, E. Y. HAYDEN, D. B. TEPLow, C. GLABE, R. ALBAY, G. M. COLE, E. TENG, AND K. H. GYLYS, *Synaptic Amyloid- β Oligomers Precede p-Tau and Differentiate High Pathology Control Cases*, *American Journal of Pathology*, 186 (2016), pp. 185–198.
- [18] T. D. BIRD, *Alzheimer Disease Overview*, *Gene Reviews*, (2018), pp. 1–12.

-
- [19] G. S. BLOOM, *Amyloid- β and tau: The trigger and bullet in Alzheimer disease pathogenesis*, JAMA Neurology, 71 (2014), pp. 505–508.
- [20] H. BOKIL, P. ANDREWS, J. E. KULKARNI, S. MEHTA, AND P. P. MITRA, *Chronux: A platform for analyzing neural signals*, Journal of Neuroscience Methods, 192 (2010), pp. 146–151.
- [21] C. BOOTH, J. WITTON, J. NOWACKI, K. TSANEVA-ATANASOVA, M. W. JONES, A. D. RANDALL, AND J. T. BROWN, *Alterations to intrinsic pyramidal neuron properties and temporoammonic synaptic plasticity underlie deficits in hippocampal network function in a mouse model of tauopathy*, Journal of Neuroscience, 36 (2016), pp. 350–363.
- [22] D. R. BORCHELT AND G. THINAKARAN, *Familial Alzheimer's Disease-Linked Presenilin 1 Variants Elevate A β 1-42/1-40 Ratio In Vitro and In Vivo*, Neuron, 17 (1996), pp. 1005–1013.
- [23] C. BÖRGERS, *The PING Model of Gamma Rhythms*, 2017.
- [24] C. BÖRGERS AND N. J. KOPELL, *Synchronization in Networks of Excitatory and Inhibitory Neurons with Sparse, Random Connectivity*, Neural Computation, 15 (2003), pp. 509–538.
- [25] C. BÖRGERS AND N. J. KOPELL, *Effects of noisy drive on rhythms in networks of excitatory and inhibitory neurons*, Neural Computation, 17 (2005), pp. 557–608.
- [26] H. BRAAK AND E. BRAAK, *Neuropathological staging of Alzheimer-related changes*, Acta Neuropathologica, 82 (1991), pp. 239–259.
- [27] A. BRAGIN, G. JANDO, Z. NADASDY, J. HETKE, K. WISE, AND G. BUZSAKI, *Gamma (40–100 Hz) oscillation in the hippocampus of the behaving rat*, Journal of Neuroscience, 15 (1995), pp. 47–60.
- [28] R. BROOKMEYER, E. JOHNSON, K. ZIEGLER-GRAHAM, AND H. M. ARRIGHI, *Forecasting the global burden of Alzheimer's disease*, Alzheimer's & Dementia: The Journal of the Alzheimer's Association, 3 (2007), pp. 186–191.
- [29] J. T. BROWN, J. CHIN, S. C. LEISER, M. N. PANGALOS, AND A. D. RANDALL, *Altered intrinsic neuronal excitability and reduced Na⁺ currents in a mouse model of Alzheimer's disease*, Neurobiology of Aging, 32 (2011), pp. 2109.e1–2109.e14.

BIBLIOGRAPHY

- [30] K. A. BRUGGINK, W. JONGBLOED, E. A. BIEMANS, R. VEERHUIS, J. A. CLAASSEN, H. B. KUIPERIJ, AND M. M. VERBEEK, *Amyloid- β oligomer detection by ELISA in cerebrospinal fluid and brain tissue*, *Analytical Biochemistry*, 433 (2013), pp. 112–120.
- [31] A. BRUN AND L. GUSTAFSON, *Distribution of cerebral degeneration in Alzheimer's disease - A clinico-pathological study*, *Archives of Psychiatry and Neurological Sciences*, 223 (1976), pp. 15–33.
- [32] D. BURDICK, B. SOREGHAN, M. KWON, J. KOSMOSKI, M. KNAUER, A. HENSCHEN, J. YATES, C. COTMAN, AND C. GLABE, *Assembly and aggregation properties of synthetic Alzheimer's A4/ β amyloid peptide analogs*, *Journal of Biological Chemistry*, 267 (1992), pp. 546–554.
- [33] E. C. BURGARD AND J. J. HABLITZ, *Developmental changes in NMDA and non-NMDA receptor-mediated synaptic potentials in rat neocortex*, *Journal of Neurophysiology*, 69 (1993), pp. 230–240.
- [34] P. C. BURGER AND F. S. VOGEL, *The development of the pathologic changes of Alzheimer's disease and senile dementia in patients with Down's syndrome*, *American Journal of Pathology*, 73 (1973), pp. 457–476.
- [35] J. L. BUTLER, Y. A. HAY, AND O. PAULSEN, *Comparison of three gamma oscillations in the mouse entorhinal-hippocampal system*, *European Journal of Neuroscience*, 48 (2018), pp. 2795–2806.
- [36] G. BUZÁKI, *Theta oscillations in the hippocampus*, *Neuron*, 33 (2002), pp. 325–340.
- [37] ———, *Hippocampal sharp wave-ripple: A cognitive biomarker for episodic memory and planning*, *Hippocampus*, 25 (2015), pp. 1073–1188.
- [38] G. BUZÁKI, C. A. ANASTASSIOU, AND C. KOCH, *The origin of extracellular fields and currents—EEG, ECoG, LFP and spikes.*, *Nature Reviews Neuroscience*, 13 (2012), pp. 407–420.
- [39] G. BUZÁKI AND A. DRAGUHN, *Neuronal oscillations in cortical networks*, *Science*, 304 (2004), pp. 1926–1929.
- [40] C. CHEN, *β -amyloid increases dendritic Ca^{2+} influx by inhibiting the A-type K^+ current in hippocampal CA1 pyramidal neurons*, *Biochemical and Biophysical Research Communications*, 338 (2005), pp. 1913–1919.

-
- [41] J. CHIN, *Selecting a Mouse Model of Alzheimer's Disease*, in *Alzheimer's Disease and Frontotemporal Dementia*, vol. 670, 2011, pp. 169–189.
- [42] C. H. CHUNG, B. BARYLKO, J. LEITZ, X. LIU, AND E. T. KAVALALI, *Acute dynamin inhibition dissects synaptic vesicle recycling pathways that drive spontaneous and evoked neurotransmission*, *Journal of Neuroscience*, 30 (2010), p. 13631376.
- [43] P. M. CLIFFORD, S. ZARRABI, G. SIU, K. J. KINSLER, M. C. KOSCIUK, V. VENKATARAMAN, M. R. D'ANDREA, S. DINSMORE, AND R. G. NAGELE, *A β peptides can enter the brain through a defective blood-brain barrier and bind selectively to neurons*, *Brain Research*, 1142 (2007), pp. 223–236.
- [44] L. L. COLGIN, *Mechanisms and Functions of Theta Rhythms*, *Annual Review of Neuroscience*, 36 (2013), pp. 295–312.
- [45] L. L. COLGIN, *Rhythms of the hippocampal network*, *Nature Reviews Neuroscience*, 17 (2016), pp. 239–249.
- [46] L. L. COLGIN, T. DENNINGER, M. FYHN, T. HAFTING, T. BONNEVIE, O. JENSEN, M. B. MOSER, AND E. I. MOSER, *Frequency of gamma oscillations routes flow of information in the hippocampus*, *Nature*, 462 (2009), pp. 353–357.
- [47] L. L. COLGIN AND E. I. MOSER, *Gamma oscillations in the hippocampus*, *Physiology*, 25 (2010), pp. 319–329.
- [48] K. D. COON, A. J. MYERS, D. W. CRAIG, J. A. WEBSTER, J. V. PEARSON, D. H. LINCE, V. L. ZISMANN, T. G. BEACH, D. LEUNG, L. BRYDEN, R. F. HALPERIN, L. MARLOWE, M. KALEEM, D. G. WALKER, R. RAVID, C. B. HEWARD, J. ROGERS, A. PAPPASOTIROPOULOS, E. M. REIMAN, J. HARDY, AND D. A. STEPHAN, *A high-density whole-genome association study reveals that APOE is the major susceptibility gene for sporadic late-onset Alzheimer's disease*, *Journal of Clinical Psychiatry*, 68 (2007), pp. 613–618.
- [49] D. C. CRAWFORD, D. M. RAMIREZ, B. TRAUTERMAN, L. M. MONTEGGIA, AND E. T. KAVALALI, *Selective molecular impairment of spontaneous neurotransmission modulates synaptic efficacy*, *Nature Communications*, 8 (2017).
- [50] J. L. CRIMINS, A. POOLER, M. POLYDORO, J. I. LUEBKE, AND T. L. SPIRES-JONES, *The intersection of amyloid beta and tau in glutamatergic synaptic dysfunction and collapse in Alzheimer's disease*, *Ageing Research Reviews*, 12 (2013), pp. 757–763.

- [51] J. CSICSVARI, B. JAMIESON, K. D. WISE, AND G. BUZSÁKI, *Mechanisms of gamma oscillations in the hippocampus of the behaving rat*, *Neuron*, 37 (2003), pp. 311–322.
- [52] W. K. CULLEN, Y. H. SUH, R. ANWYL, AND M. J. ROWAN, *Block of LTP in rat hippocampus in vivo by β -amyloid precursor protein fragments*, *NeuroReport*, (1997).
- [53] V. CULMONE AND M. MIGLIORE, *Progressive effect of beta amyloid peptides accumulation on CA1 pyramidal neurons: a model study suggesting possible treatments*, *Frontiers in Computational Neuroscience*, 6 (2012), p. 52.
- [54] C. A. DAVIES, D. M. MANN, P. Q. SUMPTER, AND P. O. YATES, *A quantitative morphometric analysis of the neuronal and synaptic content of the frontal and temporal cortex in patients with Alzheimer's disease*, *Journal of the Neurological Sciences*, 78 (1987), pp. 151–164.
- [55] M. L. DAVIGLUS, B. L. PLASSMAN, A. PIRZADA, C. C. BELL, P. E. BOWEN, J. R. BURKE, E. S. CONNOLLY, J. M. DUNBAR-JACOB, E. C. GRANIERI, K. MCGARRY, D. PATEL, M. TREVISAN, AND J. W. WILLIAMS, *Risk factors and preventive interventions for alzheimer disease: State of the science*, *Archives of Neurology*, 68 (2011), pp. 1185–1190.
- [56] S. T. DEKOSKY AND S. W. SCHEFF, *Synapse Loss in Frontal Cortex Biopsies in Alzheimer's Disease: Correlation with Cognitive Severity*, *Annals of Neurology*, 27 (1990), pp. 457–464.
- [57] S. T. DEKOSKY, S. W. SCHEFF, AND S. D. STYREN, *Structural correlates of cognition in dementia: Quantification and assessment of synapse change*, *Neurodegeneration*, 5 (1996), pp. 417–421.
- [58] J. DEL CASTILLO AND B. KATZ, *Quantal components of the end-plate potential*, *The Journal of Physiology*, 124 (1954), pp. 560–573.
- [59] A. DESTEXHE AND J. R. HUGUENARD, *5. Which formalism to use for modeling voltage-dependent conductances?*, *Computational Neuroscience: Realistic Modeling for Experimentalists*, (2000), pp. 129–157.
- [60] A. DESTEXHE, Z. F. MAINEN, AND T. J. SEJNOWSKI, *Synthesis of models for excitable membranes, synaptic transmission and neuromodulation using a common kinetic formalism*, *Journal of Computational Neuroscience*, 1 (1994), pp. 195–230.

-
- [61] A. DESTEXHE, Z. F. MAINEN, AND T. J. SEJNOWSKI, *Kinetic Models of Synaptic Transmission*, in *Methods in Neuronal Modelling*, C. Koch and I. Segev, eds., MIT Press, Cambridge, 2nd ed., 1998, ch. 1, pp. 1–25.
- [62] A. DESTEXHE, Z. F. MAINEN, AND T. J. T. SEJNOWSKI, *An efficient method for computing synaptic conductances based on a kinetic model of receptor binding*, *Neural Computation*, 6 (1994), pp. 14–18.
- [63] S. D. DONEVAN AND M. A. ROGAWSKI, *Intracellular polyamines mediate inward rectification of Ca^{2+} -permeable α -amino-3-hydroxy-5-methyl-4-isoxazolepropionic acid receptors*, *Proceedings of the National Academy of Sciences of the United States of America*, 92 (1995), pp. 9298–9302.
- [64] G. DRAGOI AND G. BUZSÁKI, *Temporal Encoding of Place Sequences by Hippocampal Cell Assemblies*, *Neuron*, 50 (2006), pp. 145–157.
- [65] B. DUBOIS, H. H. FELDMAN, C. JACOVA, J. L. CUMMINGS, S. T. DEKOSKY, P. BARBERGER-GATEAU, A. DELACOURTE, G. FRISONI, N. C. FOX, D. GALASKO, S. GAUTHIER, H. HAMPEL, G. A. JICHA, K. MEGURO, J. O'BRIEN, F. PASQUIER, P. ROBERT, M. ROSSOR, S. SALLOWAY, M. SARAZIN, L. C. DE SOUZA, Y. STERN, P. J. VISSER, AND P. SCHELTENS, *Revising the definition of Alzheimer's disease: A new lexicon*, *The Lancet Neurology*, 9 (2010), pp. 1118–1127.
- [66] G. B. ERMENTROUT AND N. J. KOPELL, *Fine structure of neural spiking and synchronization in the presence of conduction delays.*, *Proceedings of the National Academy of Sciences of the United States of America*, 95 (1998), pp. 1259–1264.
- [67] G. ETTER, S. VAN DER VELDT, F. MANSEAU, I. ZARRINKOUB, E. TRILLAUD-DOPPIA, AND S. WILLIAMS, *Optogenetic gamma stimulation rescues memory impairments in an Alzheimer's disease mouse model*, *Nature Communications*, 10 (2019), pp. 1–11.
- [68] L. A. FARRER, L. A. CUPPLES, J. L. HAINES, B. HYMAN, W. A. KUKULL, R. MAYEUX, R. H. MYERS, M. A. PERICAK-VANCE, N. RISCH, AND C. M. VAN DUIJN, *Effects of age, sex, and ethnicity on the association between apolipoprotein E genotype and Alzheimer disease: A meta-analysis*, *Journal of the American Medical Association*, 278 (1997), pp. 1349–1356.
- [69] P. FATT AND B. KATZ, *Spontaneous Subthreshold Activity at Motor*, *Journal of Physiology*, 117 (1952), pp. 109–128.

BIBLIOGRAPHY

- [70] J. FELL, P. KLAVER, K. LEHNERTZ, T. GRUNWALD, C. SCHALLER, C. E. ELGER, AND G. FERNÁNDEZ, *Human memory formation is accompanied by rhinal-hippocampal coupling and decoupling*, *Nature Neuroscience*, 4 (2001), pp. 1259–1264.
- [71] D. FRECHE, U. PANNASCH, N. ROUACH, AND D. HOLCMAN, *Synapse geometry and receptor dynamics modulate synaptic strength*, *PLoS ONE*, 6 (2011).
- [72] N. B. FREDJ AND J. BURRONE, *A resting pool of vesicles is responsible for spontaneous vesicle fusion at the synapse.*, *Nature Neuroscience*, 12 (2009), pp. 751–758.
- [73] M. FRERKING, S. BORGES, AND M. WILSON, *Are Some Minis Multiquantal?*, *Journal of Neurophysiology*, 78 (1997), pp. 1293–1304.
- [74] T. F. FREUND AND M. ANTAL, *GABA-containing neurons in the septum control inhibitory interneurons in the hippocampus*, *Nature*, (1988).
- [75] E. C. FUCHS, A. R. ZIVKOVIC, M. O. CUNNINGHAM, S. MIDDLETON, F. E. LEBEAU, D. M. BANNERMAN, A. ROZOV, M. A. WHITTINGTON, R. D. TRAUB, J. N. P. RAWLINS, AND H. MONYER, *Recruitment of Parvalbumin-Positive Interneurons Determines Hippocampal Function and Associated Behavior*, *Neuron*, 53 (2007), pp. 591–604.
- [76] S. C. FURTAK, S.-M. WEI, K. L. AGSTER, AND R. D. BURWELL, *Functional Neuroanatomy of the Parahippocampal Region in the Rat: The Perirhinal and Postrhinal Cortices*, *Hippocampus*, 17 (2007), pp. 709–722.
- [77] D. GAMES, D. ADAMS, R. ALESSANDRINI, R. BARBOUR, P. BORTHELETTE, C. BLACKWELL, T. CARR, J. CLEMENS, T. DONALDSON, F. GILLESPIE, T. GUIDO, S. HAGOPIAN, K. JOHNSON-WOOD, K. KHAN, M. LEE, P. LEIBOWITZ, I. LIEBERBURG, S. LITTLE, E. MASLIAH, L. MC CONLOGUE, M. MONTOYA-ZAVALA, L. MUCKE, L. PAGANINI, E. PENNIMAN, M. POWER, D. SCHENK, P. SEUBERT, B. SNYDER, F. SORIANO, H. TAN, J. VITALE, S. WADSWORTH, B. WOLOZIN, AND J. ZHAO, *Alzheimer-type neuropathology in transgenic mice overexpressing V717F β -amyloid precursor protein*, *Nature*, 373 (1995), pp. 523–527.
- [78] H. GEERTS, P. A. DACKS, V. DEVANARAYAN, M. HAAS, Z. KHATCHATURIAN, M. F. GORDON, S. MAUDSLEY, K. ROMERO, AND D. STEPHENSON, *From big data to smart data in Alzheimer's disease: The brain health modeling initiative to foster actionable knowledge*, *Alzheimer's & Dementia: The Journal of the Alzheimer's Association*, 12 (2016), pp. 1014–1021.

- [79] H. GEERTS, A. SPIROS, P. ROBERTS, AND R. CARR, *Towards the virtual human patient. Quantitative Systems Pharmacology in Alzheimer's disease*, European Journal of Pharmacology, 817 (2017), pp. 38–45.
- [80] M. GEPPERT, Y. GODA, R. E. HAMMER, C. LI, T. W. ROSAHL, C. F. STEVENS, AND T. C. SÜDHOF, *Synaptotagmin I: A major Ca^{2+} sensor for transmitter release at a central synapse*, Cell, 79 (1994), pp. 717–727.
- [81] J. GILBERT, S. SHU, X. YANG, Y. LU, L.-Q. ZHU, AND H.-Y. MAN, *β -Amyloid triggers aberrant over-scaling of homeostatic synaptic plasticity*, Acta Neuropathologica Communications, 4 (2016), p. 131.
- [82] C. G. GLABE, *Structural classification of toxic amyloid oligomers*, Journal of Biological Chemistry, 283 (2008), pp. 29639–29643.
- [83] S. D. GLASGOW, R. MCPHEDRAIN, J. F. MADRANGES, T. E. KENNEDY, AND E. S. RUTHAZER, *Approaches and limitations in the investigation of synaptic transmission and plasticity*, Frontiers in Synaptic Neuroscience, 11 (2019), pp. 1–16.
- [84] G. G. GLENNER AND C. W. WONG, *Alzheimer's disease and Down's syndrome: Sharing of a unique cerebrovascular amyloid fibril protein*, Biochemical and Biophysical Research Communications, 122 (1984), pp. 1131–1135.
- [85] ———, *Alzheimer's disease: Initial report of the purification and characterization of a novel cerebrovascular amyloid protein*, Biochemical and Biophysical Research Communications, 120 (1984), pp. 885–890.
- [86] A. GOATE, *Segregation of a missense mutation in the amyloid precursor gene with familial Alzheimer's disease*, Nature, 349 (1991), pp. 704–706.
- [87] J. GOLOWASCH AND F. NADIM, *Encyclopedia of Computational Neuroscience*, in Encyclopedia of Computational Neuroscience, D. Jaeger and R. Jung, eds., Springer, 2014, pp. 1–5.
- [88] T. GÓMEZ-ISLA, J. L. PRICE, D. W. MCKEEL, J. C. MORRIS, J. H. GROWDON, AND B. T. HYMAN, *Profound loss of layer II entorhinal cortex neurons occurs in very mild Alzheimer's disease.*, The Journal of Neuroscience, 16 (1996), pp. 4491–500.
- [89] C. GONZALEZ-ISLAS, P. BÜLOW, AND P. WENNER, *Regulation of synaptic scaling by action potential, independent miniature neurotransmission*, 2018.

- [90] T. A. GOOD AND R. M. MURPHY, *Effect of β -amyloid block of the fast-inactivating K^+ channel on intracellular Ca^{2+} and excitability in a modeled neuron.*, Proceedings of the National Academy of Sciences of the United States of America, 93 (1996), pp. 15130–15135.
- [91] M. S. GOODMAN, S. KUMAR, R. ZOMORRODI, Z. GHAZALA, A. S. CHEAM, M. S. BARR, Z. J. DASKALAKIS, D. M. BLUMBERGER, C. FISCHER, A. FLINT, L. MAH, N. HERMANN, C. R. BOWIE, B. H. MULSANT, T. K. RAJJI, B. G. POLLOCK, L. LOURENCO, M. BUTTERS, D. GALLAGHER, A. GOLAS, A. GRAFF, J. L. KENNEDY, S. OVAYSIKIA, M. RAPOPORT, K. THORPE, N. P. VERHOEFF, AND A. N. VOINESKOS, *Theta-Gamma coupling and working memory in Alzheimer's dementia and mild cognitive impairment*, Frontiers in Aging Neuroscience, 10 (2018), pp. 1–10.
- [92] I. GRUNDKE-IQBAL, K. IQBAL, AND Y. C. TUNG, *Abnormal phosphorylation of the microtubule-associated protein τ (tau) in Alzheimer cytoskeletal pathology*, Proceedings of the National Academy of Sciences of the United States of America, 83 (1986), pp. 44913–44917.
- [93] Q. GUO, W. FU, B. L. SOPHER, M. W. MILLER, C. B. WARE, G. M. MARTIN, AND M. P. MATTSON, *Increased vulnerability of hippocampal neurons to excitotoxic necrosis in presenilin-1 mutant knock-in mice*, Nature Medicine, 5 (1999), pp. 101–106.
- [94] O. P. HAMILL, A. MARTY, E. NEHER, B. SAKMANN, AND F. J. SIGWORTH, *Improved Patch-Clamp Techniques for High-Resolution Current Recording from Cells and Cell-Free Membrane Patches*, Pflügers Archiv, 391 (1981), pp. 85–100.
- [95] J. E. HAMOS, L. J. DEGENNARO, AND D. A. DRACHMAN, *Synaptic loss in Alzheimer's disease and other dementias.*, Neurology, 39 (1989), pp. 355–61.
- [96] H. HAMPEL, M. M. MESULAM, A. C. CUELLO, M. R. FARLOW, E. GIACOBINI, G. T. GROSSBERG, A. S. KHACHATURIAN, A. VERGALLO, E. CAVEDO, P. J. SNYDER, AND Z. S. KHACHATURIAN, *The cholinergic system in the pathophysiology and treatment of Alzheimer's disease*, Brain, 141 (2018), pp. 1917–1933.
- [97] F. T. HANE, M. ROBINSON, B. Y. LEE, O. BAI, Z. LEONENKO, AND M. S. ALBERT, *Recent Progress in Alzheimer's Disease Research, Part 3: Diagnosis and Treatment*, Journal of Alzheimer's Disease, 57 (2017), pp. 645–665.
- [98] J. HARDY AND D. ALLSOP, *Amyloid deposition as the central event in the aetiology of Alzheimer's disease*, Trends in Pharmacological Sciences, 12 (1991), pp. 383–388.

-
- [99] J. A. HARDY, G. A. HIGGINS, J. A. HARDY, AND G. A. HIGGINS, *Alzheimer's Disease: The Amyloid Cascade Hypothesis*, *Science*, 256 (1992), pp. 184–185.
- [100] J. D. HARPER, S. S. WONG, C. M. LIEBER, AND P. T. LANSBURY, *Observation of metastable A β amyloid protofibrils by atomic force microscopy*, *Chemistry and Biology*, 4 (1997), pp. 119–125.
- [101] M. HASHIMOTO, N. BOGDANOVIC, I. VOLKMANN, M. AOKI, B. WINBLAD, AND L. O. TJERNBERG, *Analysis of microdissected human neurons by a sensitive ELISA reveals a correlation between elevated intracellular concentrations of A β 42 and Alzheimer's disease neuropathology*, *Acta Neuropathologica*, (2010).
- [102] J. M. HENLEY AND K. A. WILKINSON, *Synaptic AMPA receptor composition in development, plasticity and disease*, *Nature Reviews Neuroscience*, 17 (2016), pp. 337–350.
- [103] K. HERRUP, *The case for rejecting the amyloid cascade hypothesis*, *Nature Neuroscience*, 18 (2015), pp. 794–799.
- [104] B. HILLE, *Ion channels of excitable membranes. Edition 3*, Sinauer Associates, Inc., 2001.
- [105] A. L. HODGKIN AND A. F. HUXLEY, *Propagation of Electrical Signals Along Giant Nerve Fibres*, *Proceedings of the Royal Society of London. Series B - Biological Sciences*, 140 (1952), pp. 177–183.
- [106] S. HONG, B. L. OSTASZEWSKI, T. YANG, T. T. O'MALLEY, M. JIN, K. YANAGISAWA, S. LI, T. BARTELS, AND D. J. SELKOE, *Soluble A β Oligomers Are Rapidly Sequestered from Brain ISF In Vivo and Bind GM1 Ganglioside on Cellular Membranes.*, *Neuron*, 82 (2014), pp. 308–19.
- [107] M. W. HOWARD, D. S. RIZZUTO, J. B. CAPLAN, J. R. MADSEN, J. LISMAN, R. ASCHENBRENNER-SCHEIBE, A. SCHULZE-BONHAGE, AND M. J. KAHANA, *Gamma Oscillations Correlate with Working Memory Load in Humans*, *Cerebral Cortex*, 13 (2003), pp. 1369–1374.
- [108] H. HSIEH, J. BOEHM, C. SATO, T. IWATSUBO, T. TOMITA, S. SISODIA, AND R. MALINOW, *AMPA removal underlies A β -induced synaptic depression and dendritic spine loss*, *Neuron*, 52 (2006), pp. 831–43.

BIBLIOGRAPHY

- [109] W. HU, C. TIAN, T. LI, M. YANG, H. HOU, AND Y. SHU, *Distinct contributions of $Na_v1.6$ and $Na_v1.2$ in action potential initiation and backpropagation.*, *Nature Neuroscience*, 12 (2009), pp. 996–1002.
- [110] X. HU, S. L. CRICK, G. BU, C. FRIEDEN, R. V. PAPPU, AND J.-M. LEE, *Amyloid seeds formed by cellular uptake, concentration, and aggregation of the amyloid-beta peptide*, *Proceedings of the National Academy of Sciences of the United States of America*, 106 (2009), pp. 20324–20329.
- [111] X. HUA, A. D. LEOW, N. PARIKSHAK, S. LEE, M. C. CHIANG, A. W. TOGA, C. R. JACK, M. W. WEINER, AND P. M. THOMPSON, *Tensor-based morphometry as a neuroimaging biomarker for Alzheimer's disease: An MRI study of 676 AD, MCI, and normal subjects*, *NeuroImage*, 43 (2008), pp. 458–469.
- [112] Y. HUANG AND L. MUCKE, *Alzheimer mechanisms and therapeutic strategies*, *Cell*, 148 (2012), pp. 1204–1222.
- [113] R. L. HUGANIR AND R. A. NICOLL, *AMPA receptors and synaptic plasticity: The last 25 years*, *Neuron*, 80 (2013), pp. 704–717.
- [114] B. HYMAN, G. VAN HOESEN, A. DAMASIO, AND C. BARNES, *Alzheimer's disease: cell-specific pathology isolates the hippocampal formation*, *Science*, 225 (1984), pp. 1168–1170.
- [115] T. ISHIKAWA, Y. SAHARA, AND T. TAKAHASHI, *A single packet of transmitter does not saturate postsynaptic glutamate receptors*, *Neuron*, 34 (2002), pp. 613–621.
- [116] E. IZHIKEVICH, *Dynamical systems in neuroscience: The Geometry of Excitability and Bursting*, MIT Press, 2007.
- [117] S. K. JAKAWICH, H. B. NASSER, M. J. STRONG, A. J. MCCARTNEY, A. S. PEREZ, N. RAKESH, C. J. CARRUTHERS, AND M. A. SUTTON, *Local Presynaptic Activity Gates Homeostatic Changes in Presynaptic Function Driven by Dendritic BDNF Synthesis*, *Neuron*, 68 (2010), pp. 1143–1158.
- [118] S. JANG, D. OH, Y. LEE, E. HOSY, H. SHIN, C. VAN RIESEN, D. WHITCOMB, J. M. WARBURTON, J. JO, D. KIM, S. G. KIM, S. M. UM, S.-K. KWON, M.-H. KIM, J. D. ROH, J. WOO, H. JUN, D. LEE, W. MAH, H. KIM, B.-K. KAANG, K. CHO, J.-S. RHEE, D. CHOQUET, AND E. KIM, *Synaptic adhesion molecule IgSF11 regulates synaptic transmission and plasticity*, *Nature Neuroscience*, (2015).

- [119] J. JO, D. J. WHITCOMB, K. M. OLSEN, T. L. KERRIGAN, S.-C. LO, G. BRU-MERCIER, B. DICKINSON, S. SCULLION, M. SHENG, G. COLLINGRIDGE, AND K. CHO, *A β ₁₋₄₂ inhibition of LTP is mediated by a signaling pathway involving caspase-3, Akt1 and GSK-3 β .*, Nature Neuroscience, 14 (2011), pp. 545–547.
- [120] M. J. JUTRAS, P. FRIES, AND E. A. BUFFALO, *Gamma-band synchronization in the macaque hippocampus and memory formation*, Journal of Neuroscience, 29 (2009), pp. 12521–12531.
- [121] J. KANG, H. G. LEMAIRE, A. UNTERBECK, J. M. SALBAUM, C. L. MASTERS, K. H. GRZESCHIK, G. MULTHAUP, K. BEYREUTHER, AND B. MÜLLER-HILL, *The precursor of Alzheimer's disease amyloid A4 protein resembles a cell-surface receptor*, Nature, 325 (1987), pp. 733–736.
- [122] E. KARRAN, M. MERCKEN, AND B. D. STROOPER, *The amyloid cascade hypothesis for Alzheimer's disease: An appraisal for the development of therapeutics*, Nature Reviews Drug Discovery, 10 (2011), pp. 698–712.
- [123] H. KARST AND M. JOËLS, *Corticosterone slowly enhances miniature excitatory postsynaptic current amplitude in mice CA1 hippocampal cells.*, Journal of Neurophysiology, 94 (2005), pp. 3479–3486.
- [124] B. KATZ AND R. MILEDI, *Tetrodotoxin and neuromuscular transmission.*, Proceedings of the Royal Society of London. Series B. Biological sciences, 167 (1967), pp. 8–22.
- [125] E. T. KAVALALI, *The mechanisms and functions of spontaneous neurotransmitter release.*, Nature Reviews Neuroscience, 16 (2015), pp. 5–16.
- [126] R. KAYED, E. HEAD, J. L. THOMPSON, T. M. MCINTIRE, S. C. MILTON, C. W. COTMAN, AND C. G. GLABE, *Common Structure of Soluble Amyloid Oligomers Implies Common Mechanism of Pathogenesis*, Science, 300 (2003), pp. 486–489.
- [127] T. L. KERRIGAN, J. T. BROWN, AND A. D. RANDALL, *Characterization of altered intrinsic excitability in hippocampal CA1 pyramidal cells of the A β -overproducing PDAPP mouse*, Neuropharmacology, 79 (2014), pp. 515–524.
- [128] P. KHANNA AND J. M. CARMENA, *Beta band oscillations in motor cortex reflect neural population signals that delay movement onset*, eLife, 6 (2017), pp. 1–31.

BIBLIOGRAPHY

- [129] R. J. KILLIANY, B. T. HYMAN, T. GOMEZ-ISLA, M. B. MOSS, R. KIKINIS, F. JOLESZ, R. TANZI, K. JONES, AND M. S. ALBERT, *MRI measures of entorhinal cortex vs hippocampus in preclinical AD*, *Neurology*, 58 (2002), pp. 1188–1196.
- [130] D. Y. KIM, B. W. CAREY, H. WANG, L. A. INGANO, A. M. BINSHTOK, M. H. WERTZ, W. H. PETTINGELL, P. HE, V. M. LEE, C. J. WOOLF, AND D. M. KOVACS, *BACE1 regulates voltage-gated sodium channels and neuronal activity*, *Nature Cell Biology*, 9 (2007), pp. 755–764.
- [131] M. J. KIM, K. FUTAI, J. JO, Y. HAYASHI, K. CHO, AND M. SHENG, *Synaptic Accumulation of PSD-95 and Synaptic Function Regulated by Phosphorylation of Serine-295 of PSD-95*, *Neuron*, 56 (2007), pp. 488–502.
- [132] A. M. KLEIN, N. W. KOWALL, AND R. J. FERRANTE, *Neurotoxicity and oxidative damage of beta amyloid 1-42 versus beta amyloid 1-40 in the mouse cerebral cortex*, *Annals of the New York Academy of Sciences*, 893 (1999), pp. 314–320.
- [133] T. KOENIG, L. PRICHER, T. DIERKS, D. HUBL, L. O. WAHLUND, E. R. JOHN, AND V. JELIC, *Decreased EEG synchronization in Alzheimer's disease and mild cognitive impairment*, *Neurobiology of Aging*, 26 (2005), pp. 165–171.
- [134] R. M. KOFFIE, T. HASHIMOTO, H. C. TAI, K. R. KAY, A. SERRANO-POZO, D. JOYNER, S. HOU, K. J. KOPEIKINA, M. P. FROSCHE, V. M. LEE, D. M. HOLTZMAN, B. T. HYMAN, AND T. L. SPIRES-JONES, *Apolipoprotein E4 effects in Alzheimer's disease are mediated by synaptotoxic oligomeric amyloid- β* , *Brain*, 135 (2012), pp. 2155–2168.
- [135] N. J. KOPELL, C. BORRERS, D. PERVOUCHINE, P. MALERBA, AND A. TORT, *Gamma and Theta Rhythms in Biophysical Models of Hippocampal Circuits*, in *Hippocampal Microcircuits*, Springer-Verlag New York, 2010, pp. 423–457.
- [136] A. KUMAR, A. SINGH, AND EKAVALI, *A review on Alzheimer's disease pathophysiology and its management: An update*, *Pharmacological Reports*, 67 (2015), pp. 195–203.
- [137] S. KWAK AND J. H. WEISS, *Calcium-permeable AMPA channels in neurodegenerative disease and ischemia*, *Current Opinion in Neurobiology*, 16 (2006), pp. 281–287.
- [138] P. N. LACOR, M. C. BUNIEL, P. W. FURLOW, A. S. CLEMENTE, P. T. VELASCO, M. WOOD, K. L. VIOLA, AND W. L. KLEIN, *A β oligomer-induced aberrations in synapse com-*

- position, shape, and density provide a molecular basis for loss of connectivity in Alzheimer's disease*, *Journal of Neuroscience*, 27 (2007), pp. 796–807.
- [139] F. M. LAFERLA, *Calcium dyshomeostasis and intracellular signalling in Alzheimer's disease*, *Nature Reviews Neuroscience*, 3 (2002), pp. 862–872.
- [140] F. M. LAFERLA, K. N. GREEN, AND S. ODDO, *Intracellular amyloid-beta in Alzheimer's disease.*, *Nature Reviews Neuroscience*, 8 (2007), pp. 499–509.
- [141] M. P. LAMBERT, A. K. BARLOW, B. A. CHROMY, C. EDWARDS, R. FREED, M. LIOSATOS, T. E. MORGAN, I. ROZOVSKY, B. TROMMER, K. L. VIOLA, P. WALS, C. ZHANG, C. E. FINCH, G. A. KRAFFT, AND W. L. KLEIN, *Diffusible, nonfibrillar ligands derived from A β _{1–42} are potent central nervous system neurotoxins.*, *Proceedings of the National Academy of Sciences of the United States of America*, 95 (1998), pp. 6448–53.
- [142] C. LAZZARI, M. J. KIPANYULA, M. AGOSTINI, T. POZZAN, AND C. FASOLATO, *A β ₄₂ oligomers selectively disrupt neuronal calcium release*, *Neurobiology of Aging*, 36 (2015), pp. 877–885.
- [143] B. LEGA, J. BURKE, J. JACOBS, AND M. J. KAHANA, *Slow-Theta-to-Gamma Phase-Amplitude Coupling in Human Hippocampus Supports the Formation of New Episodic Memories*, *Cerebral Cortex*, 26 (2016), pp. 268–278.
- [144] M. A. LEISSRING, Y. AKBARI, C. M. FANGER, M. D. CAHALAN, M. P. MATTSON, AND F. M. LAFERLA, *Capacitative calcium entry deficits and elevated luminal calcium content in mutant presenilin-1 knockin mice*, *Journal of Cell Biology*, 149 (2000), pp. 793–797.
- [145] C. LEVER, T. WILLS, F. CACUCCI, N. BURGESS, AND J. O'KEEFE, *Long-term plasticity in hippocampal place-cell representation of environmental geometry*, *Nature*, 416 (2002), pp. 90–94.
- [146] E. LEVY, M. D. CARMAN, I. J. FERNANDEZ-MADRID, M. D. POWER, I. LIEBERBURG, S. G. VAN DUINEN, G. T. A. BOTS, W. LUYENDIJK, AND B. FRANGIONE, *Mutation of the Alzheimer's disease amyloid gene in hereditary cerebral hemorrhage, Dutch type*, *Science*, 248 (1990), pp. 1124–1126.
- [147] H. LINDÉN, T. TETZLAFF, T. C. POTJANS, K. H. PETTERSEN, S. GRÜN, M. DIEMANN, AND G. T. EINEVOLL, *Modeling the spatial reach of the LFP*, *Neuron*, 72 (2011), pp. 859–872.

- [148] J. E. LISMAN AND O. JENSEN, *The Theta-Gamma Neural Code*, *Neuron*, 77 (2013), pp. 1002–1016.
- [149] J. E. LISMAN, S. RAGHAVACHARI, AND R. W. TSIEN, *The sequence of events that underlie quantal transmission at central glutamatergic synapses.*, *Nature Reviews Neuroscience*, 8 (2007), pp. 597–609.
- [150] C. C. LIU, T. KANEKIYO, H. XU, AND G. BU, *Apolipoprotein E and Alzheimer disease: risk, mechanisms and therapy*, *Nature Reviews Neurology*, 9 (2013), pp. 106–118.
- [151] G. LIU, S. CHOI, AND R. W. TSIEN, *Variability of neurotransmitter concentration and nonsaturation of postsynaptic AMPA receptors at synapses in hippocampal cultures and slices*, *Neuron*, 22 (1999), pp. 395–409.
- [152] W. LU, Y. SHI, A. C. JACKSON, K. BJORGAN, M. J. DURING, R. SPRENGEL, P. H. SEEBURG, AND R. A. NICOLL, *Subunit Composition of Synaptic AMPA Receptors Revealed by a Single-Cell Genetic Approach*, *Neuron*, 62 (2009), pp. 254–268.
- [153] L. F. LUE, Y. M. KUO, A. E. ROHER, L. BRACHOVA, Y. SHEN, L. SUE, T. BEACH, J. H. KURTH, R. E. RYDEL, AND J. ROGERS, *Soluble amyloid β peptide concentration as a predictor of synaptic change in Alzheimer's disease*, *American Journal of Pathology*, 155 (1999), pp. 853–862.
- [154] S. MAKIN, *The amyloid hypothesis on trial*, *Nature*, 559 (2018), pp. S4–S7.
- [155] T. MANABE, *Analysis of Synaptic Plasticity with the Slice Patch-Clamp Recording Technique*, in *Patch Clamp Techniques*, Y. Okada, ed., Springer, 2012, ch. 9, pp. 147–158.
- [156] T. MANABE, P. RENNER, AND R. A. NICOLL, *Postsynaptic contribution to long-term potentiation revealed by the analysis of miniature synaptic currents.*, *Nature*, 355 (1992), pp. 50–55.
- [157] E. MARCELLO, R. EPIS, C. SARACENO, F. GARDONI, B. BORRONI, F. CATTABENI, A. PADOVANI, AND M. DI LUCA, *SAP97-mediated local trafficking is altered in Alzheimer disease patients' hippocampus*, *Neurobiology of Aging*, 33 (2012), pp. 422.e1–422.e10.
- [158] C. MARTIN AND N. RAVEL, *Beta and gamma oscillatory activities associated with olfactory memory tasks: Different rhythms for different functional networks?*, *Frontiers in Behavioral Neuroscience*, 8 (2014), pp. 1–13.

- [159] E. MASLIAH, M. MALLORY, M. ALFORD, R. DETERESA, L. A. HANSEN, D. W. MCKEEL, AND J. C. MORRIS, *Altered expression of synaptic proteins occurs early during progression of Alzheimer's disease*, *Neurology*, 56 (2001), pp. 127–129.
- [160] C. L. MASTERS, G. SIMMS, N. A. WEINMAN, G. MULTHAUP, B. L. McDONALD, AND K. BEYREUTHER, *Amyloid plaque core protein in Alzheimer disease and Down syndrome.*, *Proceedings of the National Academy of Sciences of the United States of America*, 82 (1985), pp. 4245–9.
- [161] C. J. MCBAIN AND R. DINGLEDINE, *Dual-component miniature excitatory synaptic currents in rat hippocampal CA3 pyramidal neurons*, *Journal of Neurophysiology*, 68 (1992), pp. 16–27.
- [162] G. M. MCKHANN, D. S. KNOPMAN, H. CHERTKOW, B. T. HYMAN, C. R. JACK, C. H. KAWAS, W. E. KLUNK, W. J. KOROSHETZ, J. J. MANLY, R. MAYEUX, R. C. MOHS, J. C. MORRIS, M. N. ROSSOR, P. SCHELTENS, M. C. CARRILLO, B. THIES, S. WEINTRAUB, AND C. H. PHELPS, *The diagnosis of dementia due to Alzheimer's disease: Recommendations from the National Institute on Aging-Alzheimer's Association workgroups on diagnostic guidelines for Alzheimer's disease*, *Alzheimer's and Dementia*, 7 (2011), pp. 263–269.
- [163] C. A. MCLEAN, R. A. CHERNY, F. W. FRASER, S. J. FULLER, M. J. SMITH, K. BEYREUTHER, A. I. BUSH, AND C. L. MASTERS, *Soluble pool of A β amyloid as a determinant of severity of neurodegeneration in Alzheimer's disease*, *Annals of Neurology*, 46 (1999), pp. 860–866.
- [164] A. MEGILL, T. TRAN, K. ELDRED, N. J. LEE, P. C. WONG, H. S. HOE, A. KIRKWOOD, AND H. K. LEE, *Defective age-dependent metaplasticity in a mouse model of Alzheimer's disease*, *Journal of Neuroscience*, 35 (2015), pp. 11346–11357.
- [165] MOLECULAR DEVICES, *The Patch-Clamp Rig*, www.moleculardevices.com/sites/default/files/en/assets/infographics/dd/cns/patch-clamp-rig.pdf, 2019.
- [166] S. M. MONTGOMERY AND G. BUZSÁKI, *Gamma oscillations dynamically couple hippocampal CA3 and CA1 regions during memory task performance.*, *Proceedings of the National Academy of Sciences of the United States of America*, 104 (2007), pp. 14495–14500.

- [167] J. C. MORRIS, *Early-stage and preclinical Alzheimer disease*, *Alzheimer Disease and Associated Disorders*, 19 (2005), pp. 163–5.
- [168] T. M. MORSE, N. T. CARNEVALE, P. G. MUTALIK, M. MIGLIORE, AND G. M. SHEPHERD, *Abnormal excitability of oblique dendrites implicated in early Alzheimer's: a computational study*, *Frontiers in Neural Circuits*, 4 (2010), pp. 1–11.
- [169] M. MOSCOVITCH, R. CABEZA, G. WINOCUR, AND L. NADEL, *Episodic Memory and Beyond: The Hippocampus and Neocortex in Transformation*, *Annual Review of Psychology*, 67 (2016), pp. 105–134.
- [170] M. P. MURPHY AND H. LEVINE, *Alzheimer's disease and the amyloid- β peptide*, *Journal of Alzheimer's Disease*, 19 (2010), pp. 311–323.
- [171] M. E. MURRAY, N. R. GRAFF-RADFORD, O. A. ROSS, R. C. PETERSEN, R. DUARA, AND D. W. DICKSON, *Neuropathologically defined subtypes of Alzheimer's disease with distinct clinical characteristics: A retrospective study*, *The Lancet Neurology*, 10 (2011), pp. 785–796.
- [172] E. S. MUSIEK AND D. M. HOLTZMAN, *Three dimensions of the amyloid hypothesis: time, space and 'wingmen'*, *Nature Neuroscience*, 18 (2015), pp. 800–806.
- [173] R. G. NAGELE, M. R. D'ANDREA, W. J. ANDERSON, AND H. Y. WANG, *Intracellular accumulation of β -amyloid1-42 in neurons is facilitated by the $\alpha 7$ nicotinic acetylcholine receptor in Alzheimer's disease*, *Neuroscience*, 110 (2002), pp. 199–211.
- [174] T. NARAHASHI, J. W. MOORE, AND W. R. SCOTT, *Tetrodotoxin Blockage of Sodium Conductance Increase in Lobster Giant Axons*, *The Journal of General Physiology*, 47 (1964), pp. 965–974.
- [175] J. NÄSLUND, V. HAROUTUNIAN, R. MOHS, K. L. DAVIS, P. DAVIES, P. GREENGARD, AND J. D. BUXBAUM, *Correlation between elevated levels of amyloid β -peptide in the brain and cognitive decline*, *Journal of the American Medical Association*, 283 (2000), pp. 1571–1577.
- [176] J. NOEL, G. S. RALPH, L. PICKARD, J. WILLIAMS, E. MOLNAR, J. B. UNEY, G. L. COLLINGRIDGE, AND J. M. HENLEY, *Surface expression of AMPA receptors in hippocampal neurons is regulated by an NSF-dependent mechanism*, *Neuron*, 23 (1999), pp. 365–376.

- [177] E. NOSYREVA, K. SZABLA, A. E. AUTRY, A. G. RYAZANOV, L. M. MONTEGGIA, AND E. T. KAVALALI, *Acute suppression of spontaneous neurotransmission drives synaptic potentiation*, *Journal of Neuroscience*, 33 (2013), pp. 6990–7002.
- [178] J. NOWACKI, H. M. OSINGA, J. T. BROWN, A. D. RANDALL, AND K. TSANEVA-ATANASOVA, *A unified model of CA1/3 pyramidal cells: an investigation into excitability*, *Progress in Biophysics and Molecular Biology*, 105 (2011), pp. 34–48.
- [179] S. ODDO, A. CACCAMO, L. TRAN, M. P. LAMBERT, C. G. GLABE, W. L. KLEIN, AND F. M. LA FERLA, *Temporal profile of amyloid- β ($A\beta$) oligomerization in an in vivo model of Alzheimer disease: A link between $A\beta$ and tau pathology*, *Journal of Biological Chemistry*, 281 (2006), pp. 1599–1604.
- [180] J. O'KEEFE AND L. NADEL, *The Hippocampus as a Cognitive Map*, Oxford University Press, 1978.
- [181] J. J. PALOP AND L. MUCKE, *Amyloid- β -induced neuronal dysfunction in Alzheimer's disease: from synapses toward neural networks*, *Nature Neuroscience*, 13 (2010), pp. 812–818.
- [182] F. PANZA, M. LOZUPONE, G. LOGROSCINO, AND B. P. IMBIMBO, *A critical appraisal of amyloid- β -targeting therapies for Alzheimer disease*, *Nature Reviews Neurology*, 15 (2019), pp. 73–88.
- [183] R. C. PEARSON, M. M. ESIRI, R. W. HIORNS, G. K. WILCOCK, AND T. P. POWELL, *Anatomical correlates of the distribution of the pathological changes in the neo-cortex in Alzheimer disease*, *Proceedings of the National Academy of Sciences*, 82 (1985), pp. 4531–4534.
- [184] E. S. PELED, Z. L. NEWMAN, AND E. Y. ISACOFF, *Evoked and spontaneous transmission favored by distinct sets of synapses*, *Current Biology*, 24 (2014), pp. 484–493.
- [185] K. A. PELKEY, R. CHITTAJALLU, M. T. CRAIG, L. TRICOIRE, J. C. WESTER, AND C. J. MCBAIN, *Hippocampal gabaergic inhibitory interneurons*, *Physiological Reviews*, 97 (2017), pp. 1619–1747.
- [186] N. PIERROT, S. FERRAO SANTOS, C. FEYT, M. MOREL, J. P. BRION, AND J. N. OCTAVE, *Calcium-mediated transient phosphorylation of tau and amyloid precursor protein followed by intraneuronal amyloid- β accumulation*, *Journal of Biological Chemistry*, 281 (2006), pp. 39907–39914.

- [187] E. POPUGAEVA, E. PCHITSKAYA, AND I. BEZPROZVANNY, *Dysregulation of neuronal calcium homeostasis in Alzheimer's disease. À A therapeutic opportunity?*, Biochemical and Biophysical Research Communications, 483 (2017), pp. 998–1004.
- [188] M. POSTLETHWAITE, M. H. HENNIG, J. R. STEINERT, B. P. GRAHAM, AND I. D. FORSYTHE, *Acceleration of AMPA receptor kinetics underlies temperature-dependent changes in synaptic strength at the rat calyx of Held*, Journal of Physiology, 579 (2007), pp. 69–84.
- [189] M. PRINCE, A. WIMO, M. GUERCHET, A. GEMMA-CLAIRE, Y.-T. WU, AND M. PRINA, *World Alzheimer Report 2015: The Global Impact of Dementia - An analysis of prevalence, incidence, cost and trends*, Alzheimer's Disease International, (2015), p. 84.
- [190] W. QIANG, W. M. YAU, J. X. LU, J. COLLINGE, AND R. TYCKO, *Structural variation in amyloid- β fibrils from Alzheimer's disease clinical subtypes*, Nature, 541 (2017), pp. 217–221.
- [191] D. M. RAMIREZ, D. C. CRAWFORD, N. L. CHANADAY, B. TRAUTERMAN, L. M. MONTEGGIA, AND E. T. KAVALALI, *Loss of doc2-dependent spontaneous neurotransmission augments glutamatergic synaptic strength*, Journal of Neuroscience, 37 (2017), pp. 6224–6230.
- [192] D. M. RAMIREZ AND E. T. KAVALALI, *Differential regulation of spontaneous and evoked neurotransmitter release at central synapses*, Current Opinion in Neurobiology, 21 (2011), pp. 275–282.
- [193] J. B. RANCK, *Analysis of specific impedance of rabbit cerebral cortex*, Experimental Neurology, 7 (1963), pp. 153–174.
- [194] G. RIEDEL, J. MICHEAU, A. G. LAM, E. V. ROLOFF, S. J. MARTIN, H. BRIDGE, L. DE HOZ, B. POESCHEL, J. MCCULLOCH, AND R. G. MORRIS, *Reversible neural inactivation reveals hippocampal participation in several memory processes*, Nature Neuroscience, 2 (1999), pp. 898–905.
- [195] J. L. ROBINSON, L. MOLINA-PORCEL, M. M. CORRADA, K. RAIBLE, E. B. LEE, V. M. LEE, C. H. KAWAS, AND J. Q. TROJANOWSKI, *Perforant path synaptic loss correlates with cognitive impairment and Alzheimer's disease in the oldest-old*, Brain, 137 (2014), pp. 2578–2587.

- [196] J. ROGERS, . AND, AND J. H. MORRISON, *Quantitative Morphology and Regional and Laminar Distributions of Senile Plaques in Alzheimer's Disease*, *The Journal of Neuroscience*, 5 (1985), pp. 2801–2808.
- [197] J. L. ROLLO, N. BANIHASHEMI, F. VAFAEE, J. W. CRAWFORD, Z. KUNCIC, AND R. D. HOLSINGER, *Unraveling the mechanistic complexity of Alzheimer's disease through systems biology*, *Alzheimer's & Dementia: The Journal of the Alzheimer's Association*, (2015), pp. 1–11.
- [198] A. ROMANI, C. MARCHETTI, D. BIANCHI, X. LEINEKUGEL, P. POIRAZI, M. MIGLIORE, AND H. MARIE, *Computational modeling of the effects of amyloid-beta on release probability at hippocampal synapses.*, *Frontiers in Computational Neuroscience*, 7 (2013), p. 1.
- [199] F. ROSELLI, M. TIRARD, J. LU, P. HUTZLER, P. LAMBERTI, P. LIVREA, M. MORABITO, AND O. F. ALMEIDA, *Soluble β -amyloid_{1–40} induces NMDA-Dependent Degradation of Postsynaptic Density-95 at Glutamatergic Synapses*, *Journal of Neuroscience*, 25 (2005), pp. 11061–11070.
- [200] M. ROYECK, M.-T. HORSTMANN, S. REMY, M. REITZE, Y. YAARI, AND H. BECK, *Role of Axonal Na V 1 . 6 Sodium Channels in Action Potential Initiation of CA1 Pyramidal Neurons*, *Journal of Neurophysiology*, (2008), pp. 2361–2380.
- [201] S. SAHARA, Y. YANAGAWA, D. D. O'LEARY, AND C. F. STEVENS, *The fraction of cortical GABAergic neurons is constant from near the start of cortical neurogenesis to adulthood*, *Journal of Neuroscience*, 32 (2012), pp. 4755–4761.
- [202] A. N. SANTOS, M. EWERS, L. MINTHON, A. SIMM, R. E. SILBER, K. BLENNOW, D. PRVULOVIC, O. HANSSON, AND H. HAMPEL, *Amyloid- β oligomers in cerebrospinal fluid are associated with cognitive decline in patients with Alzheimer's disease*, *Journal of Alzheimer's Disease*, 29 (2012).
- [203] Y. SARA, M. BAL, M. ADACHI, L. M. MONTEGGIA, AND E. T. KAVALALI, *Use-dependent AMPA receptor block reveals segregation of spontaneous and evoked glutamatergic neurotransmission*, *Journal of Neuroscience*, 31 (2011), pp. 5378–5382.
- [204] S. W. SCHEFF, D. A. PRICE, F. A. SCHMITT, S. T. DEKOSKY, AND E. J. MUFSON, *Synaptic alterations in CA1 in mild Alzheimer disease and mild cognitive impairment*, *Neurology*, 68 (2007), pp. 1501–1508.

- [205] S. W. SCHEFF, D. A. PRICE, F. A. SCHMITT, AND E. J. MUFSON, *Hippocampal synaptic loss in early Alzheimer's disease and mild cognitive impairment*, *Neurobiology of Aging*, 27 (2006), pp. 1372–1384.
- [206] H. H. SCHIFFER, G. T. SWANSON, AND S. F. HEINEMANN, *Rat GluR7 and a carboxy-terminal splice variant, GluR7b, are functional kainate receptor subunits with a low sensitivity to glutamate*, *Neuron*, 19 (1997), pp. 1141–1146.
- [207] E. W. SCHOMBURG, A. FERNÁNDEZ-RUIZ, K. MIZUSEKI, A. BERÉNYI, C. A. ANASTASSIOU, C. KOCH, AND G. BUZSÁKI, *Theta Phase Segregation of Input-Specific Gamma Patterns in Entorhinal-Hippocampal Networks*, *Neuron*, 84 (2014), pp. 470–485.
- [208] A. SCIMEMI AND M. BEATO, *Determining the neurotransmitter concentration profile at active synapses*, *Molecular Neurobiology*, 40 (2009), pp. 289–306.
- [209] P. B. SEDERBERG, A. SCHULZE-BONHAGE, J. R. MADSEN, E. B. BROMFIELD, B. LITT, A. BRANDT, AND M. J. KAHANA, *Gamma oscillations distinguish true from false memories: Research report*, *Psychological Science*, 18 (2007), pp. 927–932.
- [210] D. J. SELKOE, *The molecular pathology of Alzheimer's disease*, *Neuron*, 6 (1991), pp. 487–498.
- [211] D. J. SELKOE, *Alzheimer's disease is a synaptic failure.*, *Science*, 298 (2002), pp. 789–791.
- [212] D. J. SELKOE, *Resolving controversies on the path to Alzheimer's therapeutics*, *Nature Medicine*, 17 (2011), pp. 1060–1065.
- [213] D. J. SELKOE AND J. HARDY, *The amyloid hypothesis of Alzheimer's disease at 25 years*, *EMBO Molecular Medicine*, 8 (2016), pp. 595–608.
- [214] A. SERRANO-POZO, M. P. FROSCHE, E. MASLIAH, AND B. T. HYMAN, *Neuropathological alterations in Alzheimer disease.*, *Cold Spring Harbor Perspectives in Medicine*, 1 (2011), pp. 1–24.
- [215] G. M. SHANKAR, B. L. BLOODGOOD, M. TOWNSEND, D. M. WALSH, D. J. SELKOE, AND B. L. SABATINI, *Natural oligomers of the Alzheimer amyloid- β protein induce reversible synapse loss by modulating an NMDA-type glutamate receptor-dependent signaling pathway*, *Journal of Neuroscience*, 27 (2007), pp. 2866–2875.
- [216] G. M. SHANKAR, S. LI, T. H. MEHTA, A. GARCIA-MUNOZ, N. E. SHEPARDSON, I. SMITH, F. M. BRETT, M. A. FARRELL, M. J. ROWAN, C. A. LEMERE, C. M. REGAN, D. M.

- WALSH, B. L. SABATINI, AND D. J. SELKOE, *Amyloid- β protein dimers isolated directly from Alzheimer's brains impair synaptic plasticity and memory.*, *Nature Medicine*, 14 (2008), pp. 837–842.
- [217] P. R. SHIRVALKAR, P. R. RAPP, AND M. L. SHAPIRO, *Bidirectional changes to hippocampal theta-gamma comodulation predict memory for recent spatial episodes*, *Proceedings of the National Academy of Sciences of the United States of America*, 107 (2010), pp. 7054–7059.
- [218] K. K. SKREDE AND R. H. WESTGAARD, *The transverse hippocampal slice: a well-defined cortical structure maintained in vitro*, *Brain Research*, 35 (1971), pp. 589–593.
- [219] D. H. SMALL, S. S. MOK, AND J. C. BORNSTEIN, *Alzheimer's disease and A β toxicity: from top to bottom.*, *Nature Reviews Neuroscience*, 2 (2001), pp. 595–598.
- [220] V. S. SOHAL, F. ZHANG, O. YIZHAR, AND K. DEISSEROTH, *Parvalbumin neurons and gamma rhythms enhance cortical circuit performance*, *Nature*, 459 (2009), pp. 698–702.
- [221] T. L. SPIRES-JONES AND B. HYMAN, *The Intersection of Amyloid Beta and Tau at Synapses in Alzheimer's Disease*, *Neuron*, 82 (2014), pp. 756–771.
- [222] M. SPITZER, J. WILDENHAIN, J. RAPPILBER, AND M. TYERS, *BoxPlotR: A web tool for generation of box plots*, *Nature Methods*, 11 (2014), pp. 121–122.
- [223] L. R. SQUIRE, *Memory and the hippocampus: a synthesis from findings with rats, monkeys, and humans*, *Psychological Review*, 99 (1992), pp. 195–231.
- [224] R. A. R. STELZMANN, H. N. SCHNITZLEIN, AND F. R. F. MURTAGH, *An English translation of Alzheimer's 1907 paper, "Über eine eigenartige Erkrankung der Hirnrinde"*, *Clinical Anatomy*, 8 (1995), pp. 429–431.
- [225] M. A. SUTTON, H. T. ITO, P. CRESSY, C. KEMPE, J. C. WOO, AND E. M. SCHUMAN, *Miniature Neurotransmission Stabilizes Synaptic Function via Tonic Suppression of Local Dendritic Protein Synthesis*, *Cell*, 125 (2006), pp. 785–799.
- [226] SYNAPTOSOFT INC., *MiniAnalysis 6.0.3 (trial version)*, www.synaptosoft.com/MiniAnalysis/, 2003.
- [227] R. H. TAKAHASHI, C. G. ALMEIDA, P. F. KEARNEY, F. YU, M. T. LIN, T. A. MILNER, AND G. K. GOURAS, *Oligomerization of Alzheimer's β -Amyloid within Processes*

- and Synapses of Cultured Neurons and Brain*, Journal of Neuroscience, 24 (2004), pp. 3592–3599.
- [228] F. TAMAGNINI, J. NOVELIA, T. L. KERRIGAN, J. T. BROWN, K. TSANEVA-ATANASOVA, AND A. D. RANDALL, *Altered intrinsic excitability of hippocampal CA1 pyramidal neurons in aged PDAPP mice*, Frontiers in Cellular Neuroscience, 9 (2015).
- [229] F. TAMAGNINI, S. SCULLION, J. T. BROWN, AND A. D. RANDALL, *Intrinsic excitability changes induced by acute treatment of hippocampal CA1 pyramidal neurons with exogenous amyloid β peptide*, Hippocampus, 25 (2015), pp. 786–797.
- [230] H. B. TAYLOR, R. TONG, A. F. JEANS, AND N. J. EMPTAGE, *A Novel Optical Quantal Analysis of Miniature Events Reveals Enhanced Frequency Following Amyloid β Exposure*, Frontiers in Cellular Neuroscience, 14 (2020), pp. 1–11.
- [231] R. D. TERRY, E. MASLIAH, D. P. SALMON, N. BUTTERS, R. DETERESA, R. HILL, L. A. HANSEN, AND R. KATZMAN, *Physical Basis of Cognitive Alterations in Alzheimer's Disease: Synapse loss Is the Major Correlate of Cognitive Impairment*, Annals of Neurology, 30 (1991), pp. 572–580.
- [232] R. D. TERRY, A. PECK, R. DETERESA, R. SCHECHTER, AND D. S. HOROUPIAN, *Some Morphometric Aspects of the Brain in Sede Dementia of the Ahheimer Type*, Annals of Neurology, 10 (1981), pp. 184–192.
- [233] A. B. L. TORT, M. A. KRAMER, C. THORN, D. J. GIBSON, Y. KUBOTA, A. M. GRAYBIEL, AND N. J. KOPELL, *Dynamic cross-frequency couplings of local field potential oscillations in rat striatum and hippocampus during performance of a T-maze task.*, Proceedings of the National Academy of Sciences of the United States of America, 105 (2008), pp. 20517–22.
- [234] S. F. TRAYNELIS, L. P. WOLLMUTH, C. J. MCBAIN, F. S. MENNITI, K. M. VANCE, K. K. OGDEN, K. B. HANSEN, H. YUAN, S. J. MYERS, AND R. DINGLEDINE, *Glutamate Receptor Ion Channels: Structure, Regulation, and Function*, Pharmacological Reveiws, 62 (2010), pp. 405–496.
- [235] M. TSODYKS, K. PAWELZIK, AND H. MARKRAM, *Neural networks with dynamic synapses*, Neural Computation, 10 (1998), pp. 821–835.

- [236] M. UMEMIYA, M. SENDA, AND T. H. MURPHY, *Behaviour of NMDA and AMPA receptor-mediated miniature EPSCs at rat cortical neuron synapses identified by calcium imaging*, *Journal of Physiology*, 521 (1999), pp. 113–122.
- [237] T. VAN GROEN AND J. M. WYSS, *Extrinsic projections from area CA1 of the rat hippocampus: Olfactory, cortical, subcortical, and bilateral hippocampal formation projections*, *Journal of Comparative Neurology*, 302 (1990), pp. 515–528.
- [238] G. W. VAN HOESEN, B. T. HYMAN, AND A. R. DAMASIO, *Entorhinal cortex pathology in Alzheimer's disease*, *Hippocampus*, 1 (1991), pp. 1–8.
- [239] M. K. VAN VUGT, A. SCHULZE-BONHAGE, B. LITT, A. BRANDT, AND M. J. KAHANA, *Hippocampal gamma oscillations increase with memory load*, *Journal of Neuroscience*, 30 (2010), pp. 2694–2699.
- [240] K. L. VIOLA AND W. L. KLEIN, *Amyloid β oligomers in Alzheimer's disease pathogenesis, treatment, and diagnosis*, *Acta Neuropathologica*, 129 (2015), pp. 183–206.
- [241] D. M. WALSH, I. KLYUBIN, J. V. FADEEVA, W. K. CULLEN, R. ANWYL, M. S. WOLFE, M. J. ROWAN, AND D. J. SELKOE, *Naturally secreted oligomers of amyloid β protein potently inhibit hippocampal long-term potentiation in vivo.*, *Nature*, 416 (2002), pp. 535–539.
- [242] D. M. WALSH, B. P. TSENG, R. E. RYDEL, M. B. PODLISNY, AND D. J. SELKOE, *The oligomerization of amyloid β -protein begins intracellularly in cells derived from human brain*, *Biochemistry*, 39 (2000), pp. 10831–10839.
- [243] X.-J. WANG, *Neurophysiological and Computational Principles of Cortical Rhythms in Cognition*, *Physiological Reviews*, 90 (2010), pp. 1195–1268.
- [244] X. J. WANG AND G. BUZSÁKI, *Gamma oscillation by synaptic inhibition in a hippocampal interneuronal network model.*, *The Journal of Neuroscience*, 16 (1996), pp. 6402–6413.
- [245] L. M. WARD, *Synchronous neural oscillations and cognitive processes*, *Trends in Cognitive Sciences*, 7 (2003), pp. 553–559.
- [246] M. WEST, C. H. KAWAS, L. J. MARTIN, AND J. C. TRONCOSO, *The CA1 Region of the Human Hippocampus Is a Hot Spot in Alzheimer's Disease*, *Annals of the New York Academy of Sciences*, 908 (2000), pp. 255–259.

- [247] M. J. WEST, P. D. COLEMAN, D. G. FLOOD, AND J. C. TRONCOSO, *Differences in the Pattern of Hippocampal Neuronal Loss in Normal Aging and Alzheimers-Disease*, *Lancet*, 344 (1994), pp. 769–772.
- [248] D. J. WHITCOMB, E. L. HOGG, P. REGAN, T. PIERS, P. NARAYAN, G. WHITEHEAD, B. L. WINTERS, D.-H. KIM, E. KIM, P. ST GEORGE-HYSLOP, D. KLENERMAN, G. L. COLLINGRIDGE, J. JO, AND K. CHO, *Intracellular oligomeric amyloid-beta rapidly regulates GluA1 subunit of AMPA receptor in the hippocampus*, *Scientific Reports*, 5 (2015), pp. 1–12.
- [249] G. WHITEHEAD, P. REGAN, D. J. WHITCOMB, AND K. CHO, *Ca²⁺-permeable AMPA receptor: A new perspective on amyloid-beta mediated pathophysiology of Alzheimer's disease*, *Neuropharmacology*, 112 (2017), pp. 221–227.
- [250] N. P. WILSON, B. GATES, AND M. CASTELLANOS, *Modeling the short time-scale dynamics of β -amyloid-neuron interactions*, *Journal of Theoretical Biology*, 331 (2013), pp. 28–37.
- [251] J. WINNUBST, J. E. CHEYNE, D. NICULESCU, AND C. LOHMANN, *Spontaneous Activity Drives Local Synaptic Plasticity In Vivo*, *Neuron*, 87 (2015), pp. 399–410.
- [252] B. WINTERS, *Investigating the Interplay between Muscarinic and NMDA Receptors at Hippocampal Synapses: Implications for Alzheimer's Disease*, PhD thesis, University of Bristol, 2012.
- [253] WORLD HEALTH ORGANISATION AND ALZHEIMER'S DISEASE INTERNATIONAL, *Dementia: a public health priority*, tech. rep., World Health Organization, 2012.
- [254] X.-S. WU, L. XUE, R. MOHAN, K. PARADISO, K. D. GILLIS, AND L.-G. WU, *The origin of quantal size variation: vesicular glutamate concentration plays a significant role.*, *The Journal of Neuroscience*, 27 (2007), pp. 3046–3056.
- [255] R. WYKES, A. KALMBACH, M. ELIAVA, AND J. WATERS, *Changes in the physiology of CA1 hippocampal pyramidal neurons in preplaque CRND8 mice*, *Neurobiology of Aging*, 33 (2012), pp. 1609–1623.
- [256] J. YAMAMOTO, J. SUH, D. TAKEUCHI, AND S. TONEGAWA, *Successful execution of working memory linked to synchronized high-frequency gamma oscillations*, *Cell*, 157 (2014), pp. 845–857.

- [257] M. A. YASSA AND Z. M. REAGH, *Competitive trace theory: A role for the hippocampus in contextual interference during retrieval*, *Frontiers in Behavioral Neuroscience*, 7 (2013), pp. 1–13.
- [258] M. YE, J. YANG, C. TIAN, Q. ZHU, L. YIN, S. JIANG, M. YANG, AND Y. SHU, *Differential roles of Na V 1.2 and Na V 1.6 in regulating neuronal excitability at febrile temperature and distinct contributions to febrile seizures*, *Scientific Reports*, 8 (2018), pp. 1–15.
- [259] O. ZANETTI, S. SOLERTE, AND F. CANTONI, *Life Expectancy in Alzheimer's Disease (AD)*, *Archives of gerontology and geriatrics*, 49 (2009), pp. 237–243.

